ABSTRACT

Title of dissertation: Numerical and Experimental Studies on Dynamic
Interactions of Robot Appendages with
Granular Media

Preethi Ravula, 2021

Dissertation directed by: Professor Balakumar Balachandran
Department of Mechanical Engineering

Terramechanics plays an important role in the design and control of robots moving on granular surfaces. Traction capabilities, slippage, and sinkage of a robot are governed by the interaction of a robot's appendage (such as wheel, track or leg) with the operating terrain and how the terrain motion happens with respect to the appendage during such an interaction. In this dissertation work, dynamics of robot appendages interaction with granular media is explored through numerical and experimental studies. A two dimensional (2D) numerical model, constructed using the Discrete Element Method (DEM), is adapted to simulate lugged wheel interaction with granular media. Parametric studies on wheel performance are conducted for two different control schemes, namely, a slip-based control scheme and an angular velocity-based wheel control scheme. Furthermore, the soil flow pattern under the wheel is studied by examining the force distribution and evolution of force networks during the course of wheel travel.

An experimental setup is designed to study the particle motion and force networks inside the media during dynamic forcing. Two different designs of robot appendages, a lugged and a single actuator pendulum are investigated. High speed imaging of photo-elastic particles under polarized light is used to visualize the force distributions inside the media. Qualitative behavior of force chains/networks evolution during interaction with the lugged wheel and pendulum is presented. In addition, quantitative measures of the interaction between appendage and granular media, such as, the driving torque values, appendage velocity, and particle motion are inferred from the experimental findings.

Based on this work, insights can be gained into the design influences of robot appendages on performance and further understanding can be obtained on the behavior of granular media across different length scales. Furthermore, the numerical and experimental techniques developed and outcomes of this dissertation can serve as an important foundation for optimal design and control of different robot appendages interacting with deformable surfaces.

Numerical and Experimental Studies on Dynamic Interactions of Robot Appendages with Granular Media

by

Preethi Ravula

Dissertation submitted to the Faculty of the Graduate School of the
University of Maryland, College Park in partial fulfillment
of the requirements for the degree of
Doctor of Philosophy
2021

Advisory Committee:
Professor Balakumar Balachandran, Chair and Advisor
Professor Abhijit Dasgupta, Department of Mechanical Engineering
Professor Teng Li, Department of Mechanical Engineering
Professor Peter W. Chung, Department of Mechanical Engineering
Professor Derek Richardson, Department of Astronomy (Dean's Representative)

To my family.

Acknowledgments

I would like to thank my advisor, Professor Balakumar Balachandran, for his invaluable support and guidance throughout my research. His passion for science and great depth of knowledge in any given topic has always left me inspired and motivated to broaden my horizon. I truly value his encouragement and feedback which not only pushed me to sharpen my thinking but also made me a better researcher and communicator. It has been a great learning experience being able to setup the laboratory experiment and I thank him for the opportunity. It was without a doubt a pleasant and enriching experience to work with him.

I would also like to thank the past and present members of the Dynamics and Vibrations group. The diverse backgrounds of the group have made for some intellectually stimulating discussions, be it about research, stock market, or life in general. The collaborative, fun, and supportive atmosphere within our group has made my journey at UMD, truly memorable. I am fortunate to have a wonderful support system in my family and friends who helped me navigate through some rather challenging and demanding times. I am deeply thankful to my friends for always being around to listen to me and encourage me. It was a pleasure sharing my travels, meals, struggles, and many conversations with them.

I will forever be indebted to my parents, Ravula Ramalinga Reddy and Vanaja, for their endless patience, unconditional love, and for encouraging me to pursue my passions without any reservation. I am grateful to my sister, Sruthi, brother, Pranav, niece, Humsiha, and brother-in-law, Tejswaroop, for being a force of positivity and strength to me. Without my family, I would not be the person I am today, and this dissertation would likely not have been a reality.

I am grateful to my committee members, Professor Abhijit Dasgupta, Professor Teng Li, Professor Peter Chung, and Professor Derek Richardson for agreeing to serve on my dissertation committee and for their valuable feedback and insightful comments on my research work. It was a pleasure to learn and interact with each of them. I would like to acknowledge the High-Performance Computing Center (HPCC) at the University of Maryland, for providing me with the resources required to run the simulations for this research.

The financial support for this research received through the National Science Foundation Grant No. CMMI-150761 and the Minta Martin Foundation are gratefully acknowledged.

Table of Contents

List of Tables

List of Figures

Chapter 1: Introduction

In this chapter, the author covers the problem of interest for the present study, providing background information on its relevance and the state of the art of the numerical and experimental methods for granular mechanics. Here, the goal and the general approach followed to achieve the specific objectives are introduced.

1.1 Problem of Interest

Granular materials are complex and not as well understood as solids, fluids, or gases with several remaining open problems. The problems of interest for this work are problems where robots are designed for travel on deformable and loose surfaces. Most natural surfaces are comprised of granular materials, such as sand, soil, snow, mud, gravel, debris and these surfaces can deform or flow during solid intrusions. Compared to a rigid (or nearly rigid) ground, robots required to traverse deformable surfaces can experience locomotion challenges such as sinking, slipping, and loss of traction. The locomotion challenges have been mainly attributed to the granular materials transitioning between various physical states ranging from fluid to solid or even gaseous states [Daerr and Douady, 1999]. For example, a dense and/or cohesion-less material can flow, thereby exhibiting a fluid-like behavior. On the other hand, under certain conditions, the surfaces compact due to internal friction and can act as a solid and support shear loads. This behavior is distinctive from that of the individual behavior of Newtonian fluids or elastic materials, which can be described by using existing constitutive equations of motion (for example, the use of Navier Stokes equations to describe flow of incompressible fluids). However, to describe the collective behavior of granular media, no universal equation exists and so, there is still a lack of comprehensive physical understanding of granular media.

While traversing granular surfaces, the locomotion performance of robots is critically dependant on the transmission of forces between the appendage (such as wheel, track or leg) of the robot and the terrain. Understanding the behavior of granular media and the interaction of this media with the robot/robot appendages can lead to better design and control of robots. An aim of this dissertation work is to advance such an understanding. As a part of the effort, a combination of numerical and experimental studies are undertaken to investigate the physics of interactions between deformable surfaces and solid intruders such as robot appendages. Here, the focus is on locomotion performance of the chosen robot appendage on dry granular media and developing an understanding of the parameters influencing the performance of robot and the granular media.

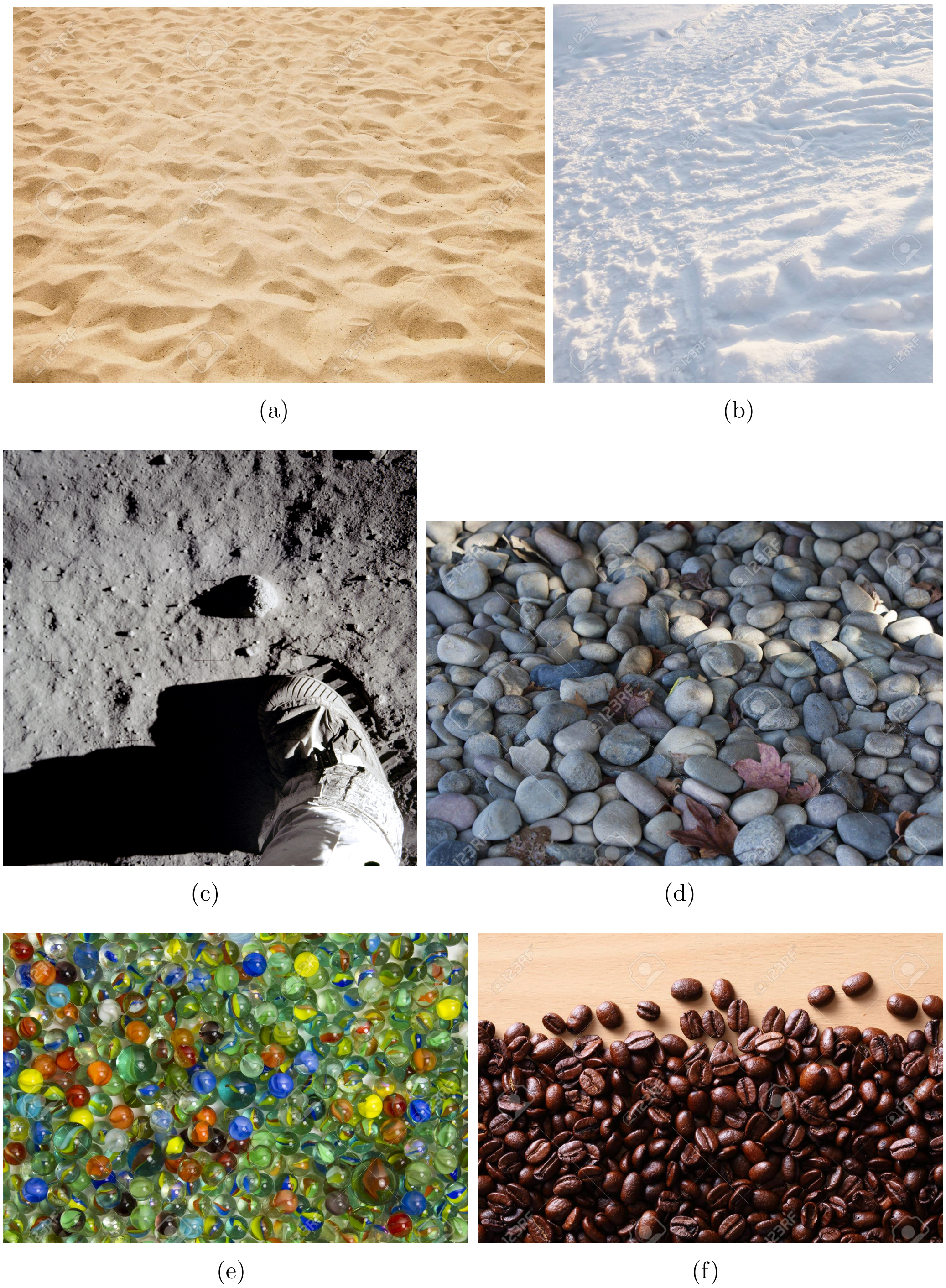

(a) (b) (c) (d) (e) (f)

Figure 1.1: Granular materials have a wide range of shapes, sizes and micromechanical properties. Examples include a) Yellow sand on a beach b) Snow surface c) A close-up view of Apollo 11 commander Neil Armstrong's boot and boot print in the lunar soil, showing the makeup of regolith on the moon d) Rocks e) Marbles f) Coffee Beans. Images Courtesy of a) b), d), e) and f) 123RF.com, and c) NASA.gov

1.2 Literature Review

Granular materials commonly occur in nature, as well as industrial applications (Figure 1.1). Owing to the significance of granular materials, a large number of experimental and numerical studies have been devoted to understanding granular media behavior. In the past few decades, granular materials have been studied in the literature in the context of powder-based additive manufacturing [Haeri et al., 2017, Fayazfar et al., 2018], pharmaceutical processes [Shah et al., 2008, Osorio et al., 2014], asteroid dynamics DeMartini et al. [2019], earthquake engineering [Johnson and Jia, 2005, Dorostkar et al., 2018] and terramechanics [Li et al., 2009, Juarez et al., 2010, Li et al., 2013].

In particular, terramechanics has received considerable attention in the past few years due to a wide range of applications of terrain robots. Known applications of small-scale robots and terrain vehicles are in space exploration, search and rescue operations, construction, mining, agriculture and so on (Figure 1.2). Researchers have explored many locomotion mechanisms designed to traverse granular surfaces including multi-legged robots, such as the RHex robot discussed by Saranli et al. [2001], the Sandbot robot in the work of Li et al. [2009], or the Basiliskbot robot discussed by Bagheri et al. [2017], wheel-leg hybrids considered by Besseron et al. [2005] and Heverly [2008], and side-winding robots, such as the snake robots explored by Marvi et al. [2014]. Planetary rovers built with lugged wheels are used for exploration on Martian surface and lunar surface, see Ding et al. [2011], Jiang et al. [2018], Hopkins et al. [2008], Nakashima et al. [2007], Nakashima et al. [2010], and Johnson et al. [2015]. In the past, planetary rovers, namely Curiosity, Opportunity, and Spirit rovers have been successfully launched on Mars and they have provided and been providing valuable information about the Martian surface. Recently, NASA has successfully launched Perseverance rover on Mars, the rover carries several instruments that can provide advanced imaging, chemical composition analysis and mineralogy of the Martian surface. Moreover, several new missions for exploring the planetary surfaces are still underway. Based on the type of application, the robots are often required to carry heavy loads and/or travel for long distances on complex and unfamiliar terrains. Developing an understanding of the performance of a robot under different driving conditions before deployment has become essential to keep the mission costs and risks at minimum. For further advancements in the design and control of robots suitable for traversing deformable surfaces, research in terramechanics is underway. Prior research in this field has been based on numerical and experimental approaches.

(a) (b)

(c)

(d) (e)

Figure 1.2: Different types of terrain robots: a) Mars exploration rover Spirit became stuck in a sand trap in 2009, b) Field trials on SherpaTT rover, an agile walking/driving robot, c) artist's illustration of Perseverance rover is successfully launched on Mars in 2021, d) Sandflea robot designed for reconnaissance can jump across the terrain, and e) beach cleaning robot. (Image credit: a) 'I&' b) NASA.gov, c) dfki.de, d) bostondynamics.com, and e) yellRobot.com)

1.2.1 Legged Locomotion: Numerical Methods

Within the research and engineering communities, a variety of numerical methods have been proposed to study the robot locomotion of granular media.

1.2.1.1 Empirical methods

Earlier terramechanics models developed for studying robot-terrain interactions include Bekker's classical terramechanics wheel model [Bekker, 1962, Smith et al., 2014]. Bekker's model, which is based on the pressure-sinkage relationship, is used by many researchers to study locomotion of off-road vehicles. While Bekker's theory is effective in modelling conventional vehicles, small-scale robots such as, planetary rovers present new challenges because of their traction loads, smaller size, terrain deformation caused by the wheels, and various other factors. Li et al. [2013] studied the dependence of forces applied by the granular media on the depth and orientation of the robot legs, and showed that hydrostatic interactions play an important role in the soil reaction forces. In addition, Slonaker et al. [2017] derived scaling relations for locomotion parameters (e.g., leg size) for robots moving on granular surfaces. Furthermore, Qian et al. [2015] studied leg penetration for various appendage designs through experiments on fluidized granular beds and numerical simulations with a resistive force based approach. However, the main disadvantage of such empirical/semi-empirical models is the inability to accurately model different types and configurations of granular materials.

Computational models that can describe the dynamics of granular material in more detail have been developed following two main approaches:

- Continuum-based approach: This approach relies on the continuum and free-flow nature of granular media and is used to develop a macroscopic view of the granular media behavior. Continuum models are derived based on the fundamental equations of physics including conservation of mass, momentum and energy, and material constitutive equations. One of the relevant advantages of the continuum based models is the ability to deal with multi-physics problems. However, in a continuum approach, it is assumed that the granular material is continuously distributed over its volume and so the contacts between individual particles are not modelled explicitly.
- Discrete approach: On the other hand, in the discrete approach, the granular material is modelled at a grain scale wherein the particles of the granular material are represented as a set of discrete rigid elements. The methods based on the discrete approach that can be used to accurately capture different physical states as well as the transitions between the states of the granular matter.

1.2.1.2 Continuum-based approach

In one of the earlier applications of continuum based simulation methods, the Finite Element method (FEM) was used to simulate the flow of the granular material. FEM is based on mesh-based representation of granular media. As such only the averaged behavior of the granular media can be determined which renders FEM not suitable to capture the detailed geometry or grain level interactions. Moreover, due to the mesh-based Lagrangian representation, when large deformations in the granular media occur resulting in severe grid distortions, the method suffers from numerical difficulties. While in some cases, FEM has been effective to simulate granular flows and deal with multi-physics, for example, granular media with fluid flow, there are many limitations and drawbacks [Crosta et al., 2009, Butterworth-Heineman, 2005]. Some of the existing FEM models are limited to 2D scenarios and not directly applicable to complex 3D systems. Furthermore, assumptions made regarding the dynamics of the granular media flow such as incompressibility, compaction, domain size, and so on limit the application of existing FEM models to different types of granular materials. To overcome some of these drawbacks, in the last decade, different mesh-less methods have been developed. Among them, the most commonly used approaches for modeling granular materials include the multi-particle method (MPM) and Smoothed Particle Hydrodynamics (SPH).

SPH is a fully mesh-less numerical method, particularly suitable for modeling free surface flows of fluids. Earlier models based on the SPH method has been developed by Lucy [1977] and Gingold and Monaghan [1977] for applications in Astronomy. In the use of SPH, the granular media is treated as an equivalent fluid moving with the flow field governed by different constitutive equations. The simulation volume of the fluid is divided into a discrete set of fuzzy particles. These particles effect or interact with the neighbouring particles through a kernel function. The main idea behind the SPH method is that the dynamics/properties of the particles are determined based on the properties of the particles in the range of the kernel function. Specifically, a set of particle evolution equations are used to represent the fluid dynamics. The kernel function has a corresponding weighing function and a smoothing length, and the physical field of the flow is determined by using the weighing function, smoothing length and the volume of each fluid particle. The governing equations of motion for in-compressible viscous flows include the Navier–Stokes (N–S) equation, the continuity equation, and the advection equation as shown below:

$$\frac{du}{dt} = -\frac{1}{\rho}\delta p + \frac{1}{\rho}(\delta\mu.\delta)u + g \tag{1.1}$$

$$\frac{d\rho}{dt} = -\rho\delta u \tag{1.2}$$

$$\frac{dr}{dt} = u \tag{1.3}$$

Here, ρ is used for density, u for velocity, t for time, p for pressure, μ for dynamic viscosity and g for acceleration due to gravity, and r for position of the fluid element.

Based on the type of flow, different types of approximations are used to express the governing equations in the SPH formalism. Kernel approximation is used to express the field functions into the integral functions, which are then approximated by using particles. Along with the conservation of mass, momentum, and energy equations, a constitutive model is implemented to relate stress and strain. One of the popular model is a Drucker-Prager constitutive model in which one follows the μ(I) rheology and relies upon a pressure-dependent yield criterion. Over the years, various constitutive models for use with SPH have been developed including, visco-plastic model, elasto-plastic model, improvements and simplifications to the Drucker-Prager model and so on [Bui et al., 2008, Ulrich et al., 2013, Ikari and Gotoh, 2016]. Wang et al. [2019] developed the SPH model for simulating interactions of wet granular media and presented studies on granular column collapse. Despite many improvements, there are still a number of drawbacks and limitations with the use of SPH method notably, treatment of boundary conditions, tensile instability, inconsistency in interpolation approximations, zero-energy models, and assumption of homogeneous and smooth particle distribution.

While SPH can be used in applications with larger deformations without suffering numerical difficulties that are inherent to mesh-based methods, the cost of computation is significantly greater compared to the grid-based counter part. This brings a compelling argument for hybrid models with a background mesh. Material Point Method (MPM) is one such method developed by Sulsky et al. [1994]. Unlike SPH, wherein no direct connectivity between particles exist, in MPM the particles are connected. In this approach, the motion of granular media is determined using a hybrid Lagrangian-Eulerian description. There have been some studies where MPM has been successfully used to simulate granular column collapse, computer graphics, impact problems, wave propagation, silo discharge, and manufacturing problems [Dunatunga and Kamrin, 2015, Wieckowski and Kowalska-Kubsik, 1999, Mast et al., 2014]. However, there are some drawbacks to the method, with one notable disadvantage being due to the consideration of assigning a fixed mass for each particle.

1.2.1.3 Discrete Approach

In contrast to continuum based approaches wherein the granular matter is represented as a continuum, in discrete approaches, the interaction between the particles is resolved at a particle length scale. Discrete element method (DEM) is one of the most established discrete approach. Cundall and Strack [1979] first introduced the Discrete Element Method (DEM), a computational technique based on particle-particle interactions for simulating granular media behavior. Ever since then, DEM has been extensively used for granular media related studies and to study robot-soil interactions, see Knuth et al. [2012], Johnson et al. [2017], Smith and Peng [2013], Nakashima and T.Kobayashi [2014], Hopkins et al. [2008], Nakashima et al. [2007], Nakashima et al. [2010], Johnson et al. [2015], Ding et al. [2009], Wong [2012], and Zhou et al. [2014].

In the use of DEM, the granular material is comprised of discrete particles that are allowed to displace independently from one another and interact only at contact points. It is assumed the deformations of individual particles are small in comparison with the deformation of the granular assembly as a whole. In other words, the deformation of granular assembly is described as primarily due to movements of individual granular as rigid bodies. As such, it can said that a good approximation of the mechanical behavior of granular assembly can still be possible in spite of the lesser precision in modeling particle deformations. Taking advantage of this argument, several simplifications are made when it comes to particle shapes, resolution, interaction models to achieve accuracy and computational efficiency based on the type of application. Nakashima et al. [2007] employed a two-dimensional (2D) DEM model to simulate the lugged wheel interactions with soft soil. In this prior work, the numerical model with a reasonable precision was validated by comparing with experimental results. DEM results on parametric influence of lugged wheel performance for a slip-based wheel control were presented. Knuth et al. [2012] and Johnson et al. [2015] employed three-dimensional (3D) discrete element method (DEM) for simulations of Mars exploration rover (MER) wheel using poly-ellipsoid and polyhedral particles, respectively. In this dissertation work, a 2D DEM model is used to simulate the interactions of granular media with different types of robot appendages. The performance of the robot appendages is critically dependent on the force transmission between the granular media and the robot appendage. As such, it has been essential to investigate the granular media at a particle scale. As detailed in Chapters 3 and 4, DEM and experimental methods have been employed to study and compare the force distributions for different configurations of robot appendages and the granular media performance.

1.2.2 Experimental Methods

In addition to numerical studies, experiments [Brzinski III et al., 2013, Birch et al., 2014, Li et al., 2018, Guerrero et al., 2018, Liu et al., 2018] have been employed in the previous studies to augment an understanding of the behavior of granular materials. Experimental studies have utilized various types of granular materials with different particle sizes [Umbanhowar et al., 1996, Losert et al., 2000, Jia et al., 1999], and material properties, including photoelasticity [Gallagher Jr et al., 1974, Van Hecke, 2005]. Photoelastic property of translucent materials have been used to understand the stress distribution in granular media, for example, Geng et al. [2003]; Wood and Leśniewska [2011]; and Lesniewska and Wood [2011]. In photoelastic materials, local changes in refractive index due to deformation make it possible to observe stress distribution and force chains inside the media in the form of bright and dark fringes (Silva and Rajchenbach [2000]). Since the number of bright and dark fringes increase with the applied force, Howell et al. [1999] developed an approach for which one counts the number of fringes in order to extract the force networks from images of photoelastic disks. In addition, Yoneyama et al. [2012] used an FEM-photoelasticity hybrid to study stress separation. Furthermore, Lim and Ravi-Chandar [2009] studied the evolution of stress distribution in dynamically loaded specimens by analyzing temporal light intensity changes.

Studies with photoelastic media include those for wave propagation [Shukla and Damania, 1987], stress fluctuations [Howell et al., 1999], and stress induced anisotropy in granular materials [Majmudar and Behringer, 2005]. Experiments with photoelastic granular media have been used in a variety of efforts, ranging from geotechnical studies [Dijkstra and Broere, 2010, Daniels and Hayman, 2008] to investigations on plant root growth in granular substrates [Wendell et al., 2012] and contact stresses in a ball bearing [Mose et al., 2018]. Furthermore, in the literature on the performance of planetary rovers, experimental studies can be found in which single wheel test beds have been used, see Ding et al. [2011], Jiang et al. [2018], and Sutoh et al. [2012]. Conditions similar to those expected to be encountered by planetary rovers have been developed and the rovers have been equipped with various sensors for measuring wheel performance.

Although, experiments are needed to obtain accurate results, it is difficult to emulate certain complex and unfamiliar terrains in an experimental setup. Moreover, it is easier to adjust system parameters in numerical simulations, and to simulate conditions such as, the effects of a planet's gravity. In the current effort, the author uses a combination of numerical and experimental studies to investigate dynamics of a robot appendage (lugged wheel/leg) interaction with soft soil. Numerical model employing DEM is used to evaluate wheel performance for different wheel configurations. As a part of the current study, the author has presented soil performance analysis and force chain visualization to demonstrate quasi-static and dynamic behavior of the granular media. To evaluate the relationship between the soil flow pattern and the wheel performance, the author has conducted DEM studies and experiments on force distribution and evolution of force chains during the course of the wheel travel.

1.3 Objectives

The overall goal of this work is to investigate the physics of interaction between granular media and robot appendages. To realize this goal, as a part of this dissertation work, the following specific objectives are pursued:

1. Study the locomotion performance of a robot with appendages like an actuated leg, a lugged wheel among others, and examine how the parameters such as,

size, control mode, load, speed, and design of an appendage influence the performance of the robot

2. Investigate the micro-scale and meso-scale behavior of granular media under dynamic loading using a visualization of inter-particle force distributions and force networks constructed by using DEM simulations; compare evolution of force chains within the granular media during interactions with different robot appendages

3. Conduct experiments with use of a laboratory scale test-bed setup and high-speed imaging to capture qualitative and quantitative behavior of force distribution in the granular media during interaction with different types of robot appendages

4. Experimentally complement the numerical findings on particle motion and force chains and reveal a quantifiable relation between the force networks in granular media and robot performance

1.4 Organization of Dissertation

The rest of the dissertation is organized as follows. Journal articles and conference presentations have followed during the course of this dissertation work.

In Chapter 2, an overview of the DEM model used for this dissertation work is presented. Computation algorithm along with performance details of the DEM model are also discussed. In addition to this, the author present a comparison of

DEM and experimental results to validate the DEM model.

In Chapter 3, the details of the DEM simulations undertaken along with the wheel performance metrics is described. Subsequently, the results obtained with angular velocity-based wheel control are presented and discussed. The effect of the control mode (i.e., angular velocity-based control and slip-based control) is examined and conclusions are presented [Ravula et al., 2021].

In Chapter 4, the details of the experimental procedure and image processing techniques used to analyze the data obtained are discussed. Subsequently, a discussion of the results including particle displacements and force chains is presented and concluding remarks are collected together and presented at the end. The experimental work is discussed along with the results obtained, and comparisons are made with observations made in numerical simulations [Acar et al., 2021, Ravula and Balachandran, 2021].

In Chapter 5, the dissertation contributions are highlighted and future directions are discussed. Appendices related to the simulations and experiments are also included.

Chapter 2: Discrete Element Method

In this dissertation work, a two-dimensional DEM model is used to simulate granular media interactions. DEM, which is a computational technique based on particle-particle interactions, was first introduced by Cundall and Strack [1979]. For many applications, DEM is known to be suitable for simulating dynamics of an assembly of particles. Some of the material presented in this chapter has been published by the author Ravula et al. [2021].

In this chapter, the author reports on the following:

- Different computational modeling aspects of the DEM including contact models, algorithm stability, integration schemes, and parallel processing.
- Validation of the model with experimental results from literature. For a spherical projectile, simulation results from DEM on particle interactions are compared with experimental results.

In the use of DEM, the granular media is represented as a finite number of particles/discrete elements that are subject to Newton's laws of motion. The particles have a defined shape, size, and position. Furthermore, each of the particles have a translational velocity and a rotational velocity and can move independently relative to each other. The computational modelling framework, as shown in Figure

Table 2.1: Nomenclature

K_n	Normal Stiffness
K_t	Tangential Stiffness
K_r	Rolling Stiffness
C_n	Normal damping constant
C_t	Tangential damping constant
C_r	Rolling damping constant
μ	Friction coefficient for particle-particle interaction
μ_r	Rolling Friction coefficient
δ_n	Overlap in normal direction
δ_t	Overlap in tangential direction
δ_{theta_r}	Relative rolling rotational angle
E	Young's modulus
G	Shear modulus
ν	Poisson's ratio
e	Coefficient of restitution
ω	Angular velocity
g	Acceleration due to gravity
Δt	Time step
R_i	Radius of particle 'i'
r_i	Position vector of particle 'i'
x_i	Displacement of particle 'i' in X direction
y_i	Displacement of particle 'y' in X direction
m_i	mass of particle 'i'
F_{ij}	Force on particle 'i' due to contact with particle 'j'
M_{ij}^r	Rolling resistance moment on particle 'i' due to particle 'j'

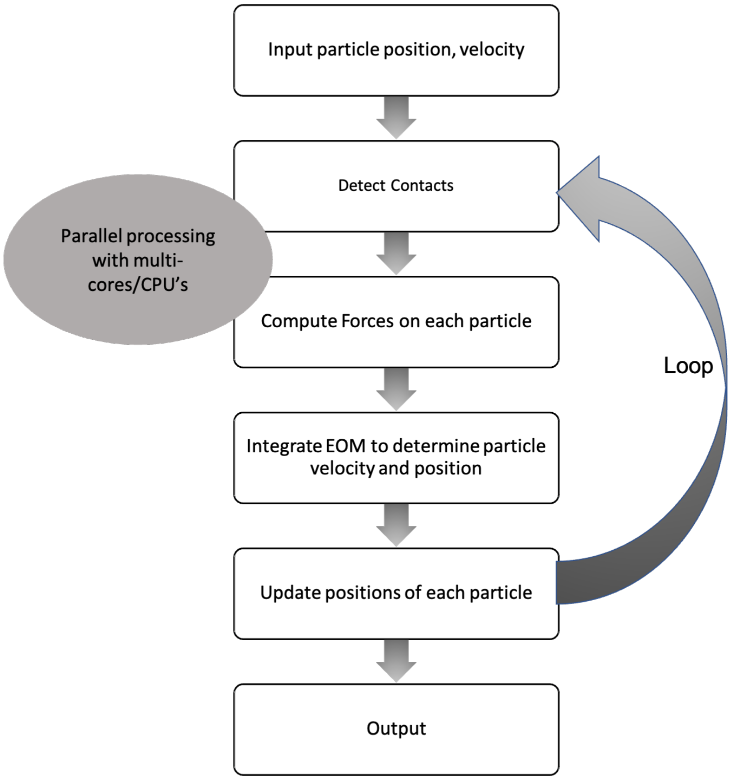

Figure 2.1: Computational framework for DEM modeling of granular media.

2.1 of the DEM follows an iterative process to update the velocity and position of each of the particles in time, which will be discussed in detail later in the chapter. To start with, a system geometry including shape, positions, velocities of the particles, and boundary conditions are specified. There have been research studies, wherein the particles have been modelled with complex shapes such as circular, polygonal, ellipsoid, poly-ellipsoid, or clustering of multiple particles [Latham et al., 2008]. Some of the methods of representations of particle geometry is shown in Figure 2.2.

For the studies herein after, the particle shape is considered as being circular to reduce the complexity and cost of computations. The particle dynamics is governed by inter-particle forces arising from collision with neighbouring particles or external bodies. The inter-particle forces exist only if there is contact between the

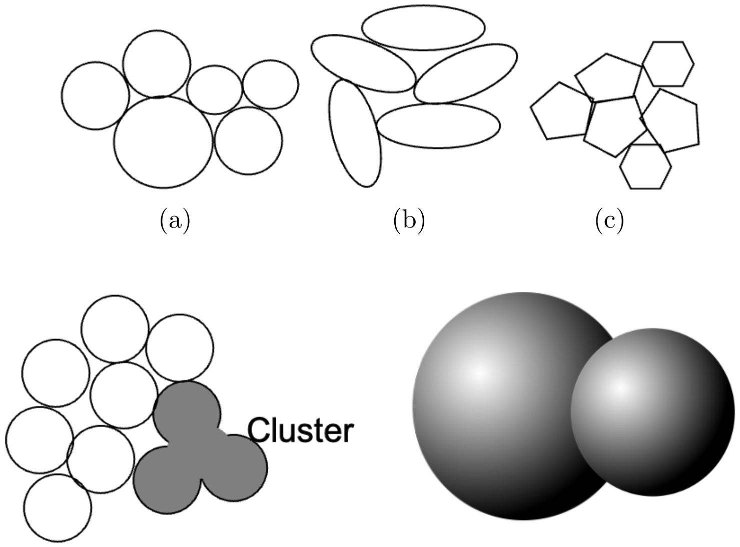

(a) (b) (c)

(d) (e)

Figure 2.2: Different methods of representation of particles for DEM modeling.

particles. The contact forces can be resolved into a normal force component and a tangential force component. The contact forces are calculated based on the contact model chosen for the granular media; this will be explained in detail later in the chapter. Apart from the contact forces, the particles have external forces such as a gravitational force. Two representative particles in contact are shown in Figure 2.3. The translation and rotation of the particle i are governed by the following equations of motion:

$$m_i \frac{d^2 x_i}{dt^2} = \sum_j (\vec{F}^n_{ij}.\hat{x}_i + \vec{F}^t_{ij}.\hat{x}_i) + F_{x,ext} \tag{2.1}$$

$$m_i \frac{d^2 y_i}{dt^2} = \sum_j (\vec{F}^n_{ij}.\hat{y}_i + \vec{F}^t_{ij}.\hat{y}_i) + F_{y,ext} \tag{2.2}$$

$$I_i \frac{d\omega_i}{dt} = \sum_j M_{ij} + T_{ext} \tag{2.3}$$

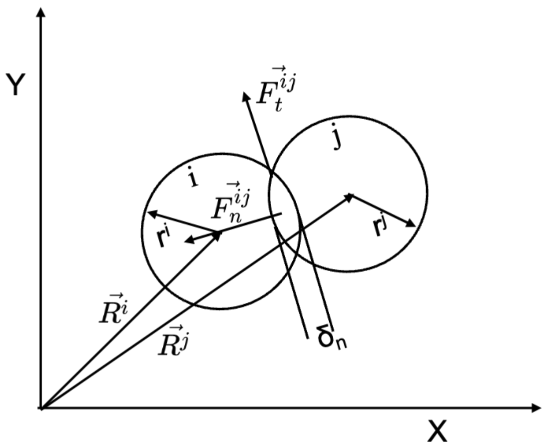

Figure 2.3: Schematic diagram of two circular particles in contact.

where m_i is the mass of particle i, x_i, y_i are,respectively, the X and Y co-ordinates of particle i, ω_i is the angular velocity of particle i, t is the time variable, $F_{x,ext}$ and $F_{y,ext}$ are respectively, the external forces on particle i in X and Y directions, M_{ij} is the torque exerted by particle j on particle i, and T_{ext} is the external torque on particle i.

At each computational time step, the particles in contact are determined. The overlap between particles i and j can be determined based on the following equation:

$$\delta_n = r_i + r_j - |\vec{R}_i - \vec{R}_j| \tag{2.4}$$

The particles i and j are said to be in contact if the corresponding overlap δ_n is greater than zero. Accordingly, for the particles in contact, inter-particle forces can be determined based on the contact model.

2.1 Contact Model

As mentioned before, the inter-particle forces arise from collision with neighbouring particles or external bodies. If the collision between the particles is instantaneous, the particles are modelled as hard particles, wherein the coefficient of restitution is used to determine the particle dynamics. Here, a soft particle method is used, in which the collision time is non-zero allowing for an overlap between the particles. In soft particle DEM, the deformation of a particle is small compared to the size of the particle. The surface of the particle undergoes deformation due to these inter-particle contacts. Consideration of asymmetrical shape for particles may result in more than one contact between particles that may be accurate for some real-world granular particles. In this dissertation work, as earlier mentioned, to reduce the complexity and computational cost, all the particles are considered to have a circular shape. The particles are packed in a hexagonal close packing (HCP) structure to resemble dense granular media. Dynamics of robot locomotion on heterogeneous media; that is, different particle size distributions (PSD) and/or different particle shapes will be the subject of future studies.

2.1.1 Linear Contact Model

Based on the type of granular media, different types of contacts such as, linear or non-linear elastic, visco-elastic or plastic contacts are possible. In a linear elastic model, the normal contact force on the particles is directly proportional to the overlap. In a visco-elastic model, viscous effects along with the elastic forces

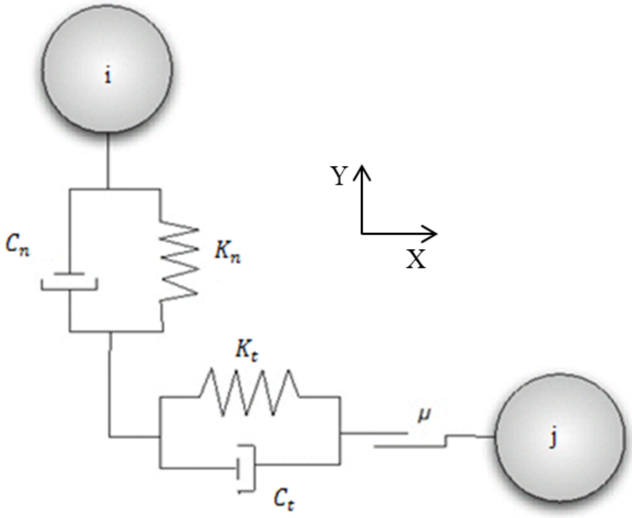

Figure 2.4: DEM contact model.

are included for the contact between the particles. In this work, a visco-elastic model with a linear force-displacement relationship is considered for the granular media. For the visco-elastic model, the contact is represented by fictitious springs and dampers between the particles. In Figure 2.4, the author has shown the contact model used for determining contact forces. The particles i and j are connected by a spring, damper in a normal direction and; a spring, a damper, and a slider in the tangential direction. In the Cartesian coordinate system, for particle i with co-ordinates x_i and y_i, the force F_{ij} due to contact with particle j is determined by using equations (2.1)-(2.3). The contact force F_{ij} is non-zero only if there is a non-zero overlap δ_n, between the corresponding particles. The force F_{ij} on particle i due to contact with the particle j is resolved into normal and tangential components with respect to the plane of contact. The normal force component consists of the elastic and viscous forces. The tangential component includes an additional force due to friction modeled based on Coulomb's law.

For δ_n,

$$\vec{F}_{ij} = \vec{F}_{ij}^n + \vec{F}_{ij}^t \tag{2.5}$$

$$F_{ij}^n = -(K_n \delta_n + C_n \dot{\delta_n}) \tag{2.6}$$

$$F_{ij}^t = min((K_t \delta_t + C_t \dot{\delta_t}), \mu |\vec{F}_{ij}^n|) \tag{2.7}$$

Here, F_{ij} is the contact force on particle i due to contact with particle j, and F_{ij}^n, F_{ij}^t are the normal and tangential components of the force F_{ij}, respectively. The overlap in tangential direction δ_t can be calculated as follows:

$$\delta_t(t) = \int_{t_0}^{t} v_t^{rel}(t')\, dt' = v_t^{rel} \Delta t \tag{2.8}$$

The DEM parameters K_n, C_n, K_t, C_t, and μ used for determining the forces F_{ij}^n, F_{ij}^t are dependent on material properties of both the particles i and j. Moreover, the stiffness coefficients K_n and K_t can be related to the damping coefficients C_n and C_t respectively as follows:

$$C_n = 2\xi \sqrt{m_{eff} K_n}; \tag{2.9}$$

$$m_{eff} = \frac{m_i m_j}{m_i + m_j} \tag{2.10}$$

$$\xi = \frac{lne}{\sqrt{lne + \pi^2}} \tag{2.11}$$

Here, the coefficient of restitution e, the average mass of both the particles i and j m_{eff}, the damping factor ξ are used to relate the DEM parameters K_n and C_n.

For realistic particles with non-circular shape, the line of action of the normal contact force may not pass through the center of mass of the particles. As such, the normal force would generate a rotational moment on the particles. To account for these shape effects, rolling resistance is incorporated into the contact model. Many researchers have addressed the importance of introducing rolling resistance into the contact model, see Belheine et al. [2009], Iwashita and Oda [1998], and Li et al. [2005]. The elastic rolling moment is proportional to the relative rolling angular displacement. Including the damping effect, the visco-elastic rolling resistance moment can be defined as:

$$M_r^{ve} = -(K_r \delta_{\theta_r} + C_r \dot{\delta_{\theta_r}}) \tag{2.12}$$

Here, K_r is the rolling stiffness, δ_{θ_r} is the relative rotational angle, and C_r is the rolling viscous damping coefficient. Applying Coulomb's law of friction, the maximum rolling resistance moment can be determined by:

$$M_{ij}^r \leq \mu_r R_{eff} |\vec{F}_{ij}^n|) \tag{2.13}$$

Here, μ_r is the static rolling friction coefficient and R_{eff} is the average radius of particle. Apart from the moment, rolling resistance can also be incorporated in the tangential force components [Li et al., 2005].

2.1.2 Hertz Mindlin Contact Model

In a Hertz contact model, force and displacement are related non-linearly through the stiffness coefficient. The stiffness coefficient is a function of geometry of the particles and the properties of contact components. For an elastic Hertzian contact, the equations for the normal and tangential forces are determined as shown next:

For $\delta_n > 0$,

$$F_n^{sh} = -(K_n^h {\delta_n}^{3/2}); \; = -\frac{4}{3}\sqrt{R_{eff}} E_{eff} (\delta_n)^3/2; \tag{2.14}$$

$$F_t^{sh} = -(K_t^h \delta_t); \tag{2.15}$$

$$K_n^h = \frac{dF_n^s}{d\delta_n} = 2E_{eff}\sqrt{R_{eff}\delta_n}; \tag{2.16}$$

$$K_t^h = 8G_{eff}\sqrt{R_{eff}\delta_n} \tag{2.17}$$

$$R_{eff} = \frac{R_i R_j}{R_i + R_j} \tag{2.18}$$

$$\frac{1}{E_{eff}} = \frac{1 - {\nu_i}^2}{E_i} + \frac{1 - {\nu_j}^2}{E_j} \tag{2.19}$$

Here, F_n^{sh} and F_t^{sh} are the normal and tangential spring forces for the Hertz contact model, respectively. Average quantities of both the particles i and j such as, the Young's modulus E_{eff}, shear modulus G_{eff}, radius R_{eff}, and the Poisson's ratio ν are used to determine the DEM parameters K_n^h and K_t^h.

2.2 Integration schemes

Based on the contact model chosen for the granular material, the inter-particle/contact forces are calculated and summed up for each of the particles. Along with the contact forces, external forces such as gravity are also added to determine the total force on each of the particles of the granular assembly. At each time step of the simulation, velocities and positions are determined and updated for each particle by numerically integrating the equations of motion. Based on the computational cost and algorithm stability and truncation errors acceptable for the model, various integration schemes are possible. In general, integration schemes can be divided into the one-step method, multi-step method, and predictor-corrector methods. One of the simplest one-step method is the Euler scheme which is an explicit method used for numerically integrating ordinary differential equations. At each time step, to determine velocities and positions from accelerations, the Forward Euler method follows the equations:

$$\dot{x}_{t+\Delta t} = \dot{x}_t + \ddot{x}_i \Delta t \tag{2.20}$$

$$x_{t+\Delta t} = x_t + \dot{x}_i \Delta t \tag{2.21}$$

First, the equations of motion (2.1-2.3) are used to calculate the translational and rotational accelerations of particles. At time step t, velocity of the particles is determined from the acceleration by using the equation (2.20). Next, displacements and rotations of particles for the next time step are determined from the velocity by using the equation (2.21). Similar to the displacement and velocity calculations in the X direction as shown here, the displacement and velocity in the Y direction and; angular velocity and orientation for the time step can be calculated. The new position and orientation of particles are then established based on the calculated displacements and rotations. In the next time step, the particles in contact are calculated, contact forces are calculated and the calculations for new positions and orientations are repeated.

Another popular one-step algorithm used for integrating equations of motion in DEM is a central difference or Verlet algorithm. In contrast to the Euler scheme, with the Verlet algorithm, the velocities and positions of the particles are calculated for time steps that are t/2 apart. The Verlet algorithm can be written as:

$$\dot{x}_{t+\Delta t/2} = \dot{x}_{t-\Delta t/2} + \ddot{x}_i \Delta t \tag{2.22}$$

$$x_{t+\Delta t} = x_t + \dot{x}_{t+\Delta t/2} \Delta t \tag{2.23}$$

In multi-step algorithms, the results from previous time steps are stored and used to calculate values of future velocities and positions. In this work, Gear's fourth order Predictor-corrector method, which is based on a multi-step process is explored for DEM. Typically, the predictor-corrector method proceeds in two steps, a prediction step in which a rough approximation of the target value is calculated and in the corrector step, the predicted value is refined by using another method. Typically, the two steps of the predictor-corrector algorithm can be expressed in the form:

$$\tilde{x_{t+1}} = x_t + f x_t, t\Delta t \tag{2.24}$$

$$x_{t+1} = x_t + \frac{1}{2} x_t, t\Delta t + f x_t, t\Delta t \tag{2.25}$$

Specifically, the predictions for the Gear's fourth order predictor-corrector algorithm follows the following equations:

$$\dot{x}_{t+\Delta t/2} = \dot{x}_{t-\Delta t/2} + \ddot{x}_i \Delta t \tag{2.26}$$

$$x^p_{t+\Delta t} = x_t + \dot{x}_t \Delta t + \frac{1}{2}\ddot{x}_i \Delta t^2 + \frac{1}{6}C^1_t \Delta t^3 + \frac{1}{24}C^2_t \Delta t^4 \tag{2.27}$$

$$\dot{x^p}_{t+\Delta t} = \dot{x}_t + \ddot{x}_t \Delta t + \frac{1}{2}C^1_t \Delta t^2 + \frac{1}{6}C^2_t \Delta t^3 \tag{2.28}$$

$$\ddot{x^p}_{t+\Delta t} = \ddot{x}_t + C^1_t \Delta t + \frac{1}{2}C^2_t \Delta t^2 \tag{2.29}$$

$$C^{1p}_{t+\Delta t} = C^1_t + C^2_t \Delta t \tag{2.30}$$

$$C^{2p}_{t+\Delta t} = C^2_t \tag{2.31}$$

Here, C^1 can be calculated as the time derivative of acceleration $\ddot{x}_i$ and C^2 can be calculated as the time derivative of C^1. The predicted results calculated by using the above equations are used to further calculate the final positions, and velocities at the next time step by using the following equations:

$$x_{t+\Delta t} = x^p_{t+\Delta t} + \frac{19}{240}(\ddot{x^p}_{t+\Delta t} - \ddot{x}_{t+\Delta t})\Delta t^2 \tag{2.32}$$

$$\dot{x}_{t+\Delta t} = \dot{x^p}_{t+\Delta t} + \frac{3}{8}(\ddot{x^p}_{t+\Delta t} - \ddot{x}_{t+\Delta t})\Delta t \tag{2.33}$$

$$\ddot{x}_{t+\Delta t} = \ddot{x^p}_{t+\Delta t} + (\ddot{x^p}_{t+\Delta t} - \ddot{x}_{t+\Delta t}) \tag{2.34}$$

$$C^1_{t+\Delta t} = C^{1p}_{t+\Delta t} + \frac{3}{2}\frac{(\ddot{x^p}_{t+\Delta t} - \ddot{x}_{t+\Delta t})}{t} \tag{2.35}$$

$$C^2_{t+\Delta t} = C^{2p}_{t+\Delta t} + \frac{(\ddot{x^p}_{t+\Delta t} - \ddot{x}_{t+\Delta t})}{t^2} \tag{2.36}$$

The use of higher order integration schemes results in an increase of the computational costs of the simulation but can improve the accuracy of calculations. For each of the integration methods, the integration time step plays a critical role in determining the numerical stability of the algorithm, global errors, and truncation errors. While, small time steps improve the accuracy of the simulations, it also renders the simulations computationally expensive. So, there is always a trade off between the cost and accuracy of calculations and the integration schemes are chosen based on the type of applications. In DEM applications, there is an additional constraint to follow when choosing the time step of integration. The integration time step depends critically on the duration of contact between the particles. which in turn is affected by particle mass, stiffness, and damping constants.

$$\Delta t_{cr} = min(\sqrt{m_i/k_n}) \tag{2.37}$$

In this dissertation work, the radius of the granular material considered for DEM studies are of the order of 10^{-3} to 10^{-4}, which warrants the use of very small sizes of time steps for the integration scheme. As such, for the chosen time steps for DEM simulations, no significant difference was observed in the accuracy with the use of either a one-step or a Predictor-Corrector integration scheme. par

2.3 Computational Cost

In addition to the size time step, integration scheme, the number of particles also effect the computational cost of the DEM simulations. Contact detection

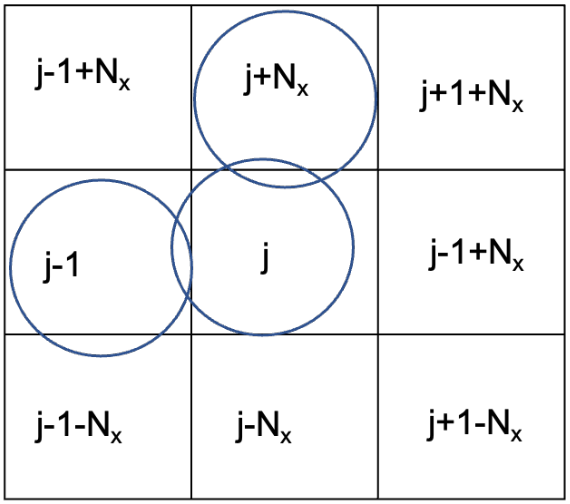

Figure 2.5: Each of the particles is assigned to a bin with unique bin numbers. To detect contacts for particle j, only the neighboring 8 bins are searched for contacts, here, N_x is total number of columns in the computational grid.

between the particles and numerical integration are some of the computationally expensive processes in DEM. To search for contacts between particles, a basic approach is to search the entire domain of particles for contacts, which results in complexity of $O(N^2)$. A linear sorting algorithm with a computational complexity of $O(N)$ is employed to detect the contacts between the particles. In this algorithm, the simulation area/test bed is uniformly discretized into rectilinear bins/boxes. Each box has a length approximately equal to the diameter of the particles and each of the particles has a unique box number. The box number for each of the particles is determined based on their position in the grid. As shown in Figure 2.5, each box is surrounded by 8 boxes and only the neighboring cells need to be searched for detecting contact for the particle in the box j. The improvement in the computational speed with the use of a linear sorting algorithm as opposed to searching entire domain of particles for contact is shown in Figure 2.6.

The algorithm can also be extended to the three dimensional DEM model

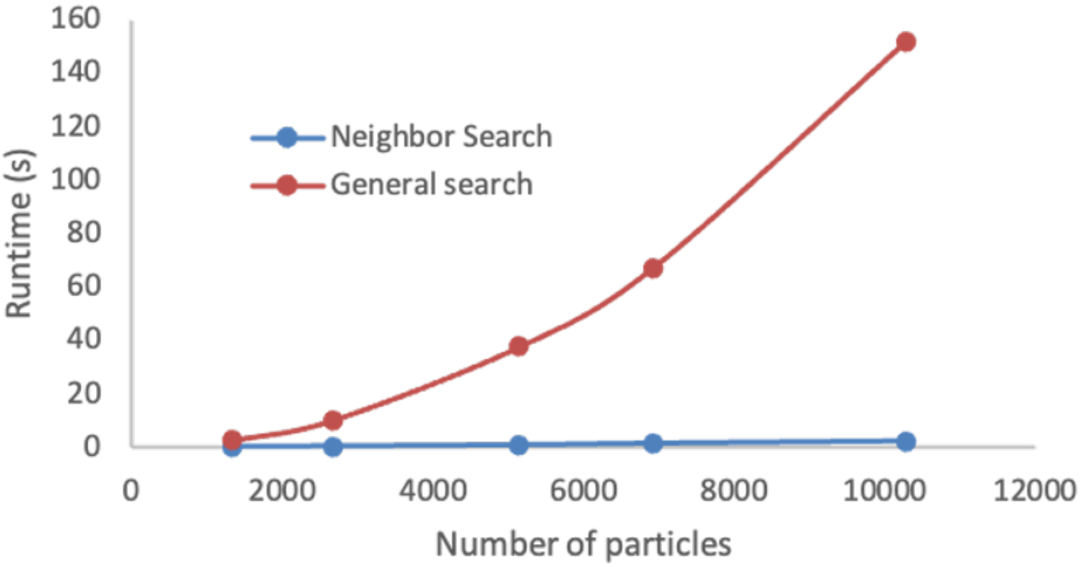

Figure 2.6: Performance of an exhaustive search and neighbor search algorithm used for contact detection and resolution are plotted.

wherein only neighboring 12 cells need to be searched for contacts thus improving the complexity. Taking advantage of the availability of large number of GPUs and multi-core CPUs, computational efficiency of the DEM simulations can be further improved. In the DEM framework, the task of determining contacts as well as forces for all the particles can be distributed among multiple processors to further improve the computational efficiency. A parallel computing framework that enables the author to run the simulations on high performance computing (HPC) clusters is employed. In Figure 2.7, architecture for the parallel processing is shown. As shown, the tasks for all the particles can be distributed among the workers. The workers can be different cores in a CPU or different CPUs in the cluster. Similar to the CPU parallel processing, the framework can be implemented on GPUs as well. Due to the availability of the larger number of GPU nodes compared to CPU cores, the efficiency with GPU implementation is higher than that with CPU implementation.

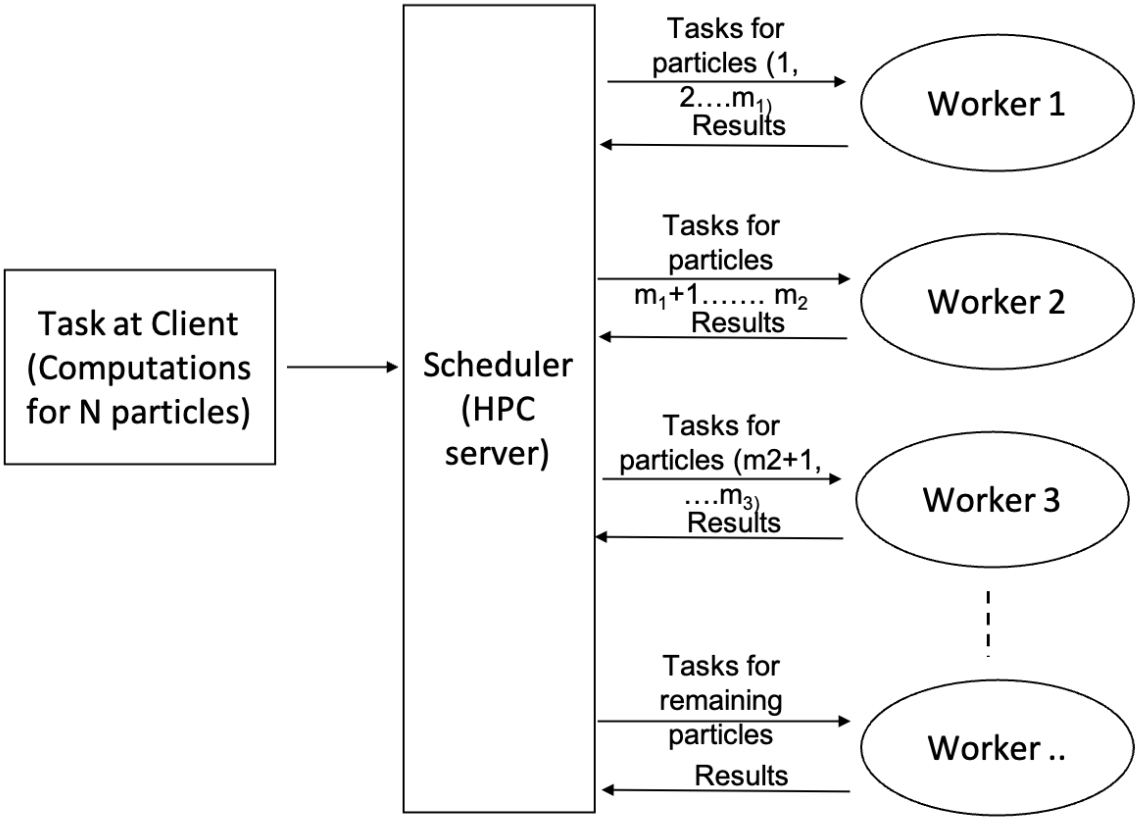

Figure 2.7: Parallel Processing framework used for DEM. Each worker is used to compute the tasks for a fraction of the total number of particles.

In Figure 2.8, the performance improvement with the number of workers used is shown.

2.4 Validation

2.4.1 Spherical Projectile

The DEM model used herein for this dissertation work follows the scientific principles where ever applicable. Further, the DEM model has also been validated by comparisons with experimental results as shown in this section. To validate the granular media interactions modelled by using DEM, the author shows the compar-

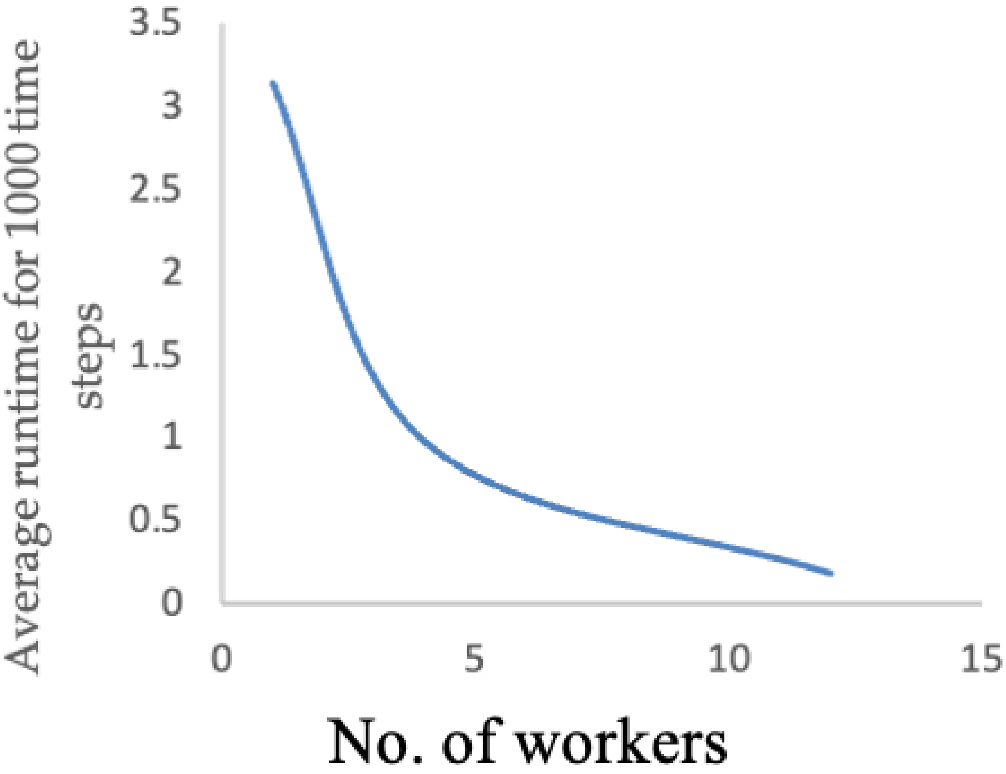

Figure 2.8: Performance of the parallel processing framework versus the number of workers used to implement the framework.

ison with experimental results reported by Tanaka et al. [2002]. The experiment is conducted with 329 nylon spheres in closely packed rectangular arrangement and a steel projectile. The top surface of the granular matter is impacted with the spherical steel projectile by using a small pneumatic gun. The motion of particles and the projectile is recorded with a high-speed video camera.

The DEM model employed for the studies presented in this paper is used to model the interaction between the granular matter and the spherical projectile. Similar initial conditions are provided for the simulations to make a direct comparison with the experimental results. The particles are allowed to reach an equilibrium and then impacted with the projectile with the same velocity as that of the experiments.

Comparison of motions of the particles and the projectile captured at regular intervals of 10ms from DEM simulations and the corresponding experimental results are shown in Figure 2.9. It can be seen that the motion of the projectile and the particles is captured well by using the DEM simulations.

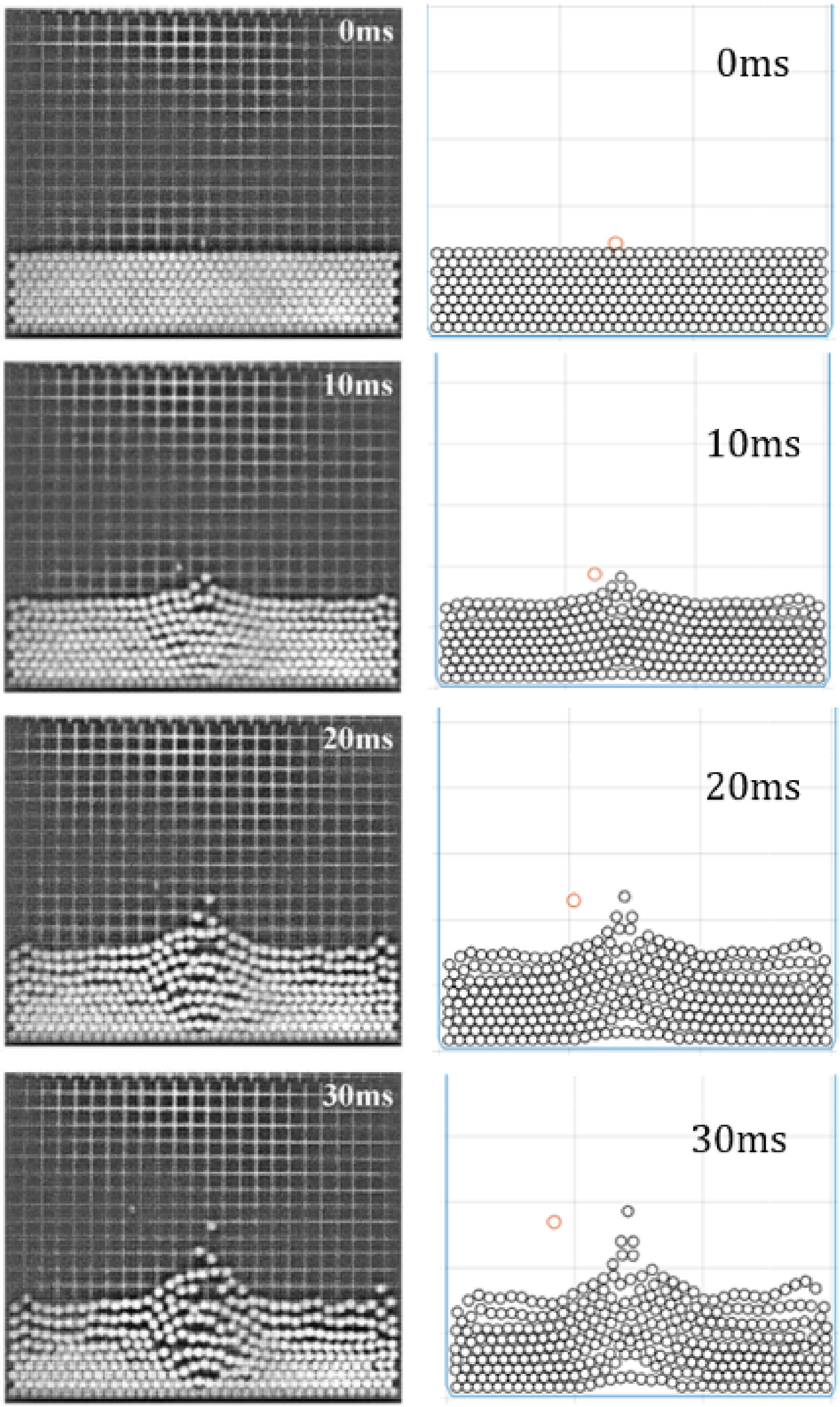

Figure 2.9: Comparison of experimental results (left side) and DEM results (right side) for motion of particle due to an impact with the projectile captured at 0 ms, 10 ms, 20 ms, and 30 ms.

Chapter 3: Dynamic interactions of lugged wheel with granular media

In this chapter, investigations on the influence of configuration and control mode used for the wheel on the locomotion performance of the wheel is presented based on the work, which is reported in the reference Ravula et al. [2021]. Wheel performance has been evaluated for different wheel configurations and the results obtained include sinkage, gross traction, tractive efficiency, and power consumption for angular velocity-based wheel control. Then, a wheel-performance comparison is carried out between the case of angular velocity-based wheel control and the case of slip-based wheel control. As a part of the current study, the author has presented soil performance analysis and force chain visualization to demonstrate quasi-static and dynamic behavior of the granular media. During wheel-soil interactions, energy transferred from the wheel propagates inside the soil through force networks and eventually gets dissipated. Since the soil cannot support a stress higher than its maximum shear stress, the soil starts to flow under a wheel loading leading to such a stress state. Further, if the wheel operates at a traction higher than this maximum shear stress, the wheel also starts to sink. To evaluate the relationship between the force distributions inside the soil and the wheel performance, the author has conducted DEM studies on force distribution and evolution of force chains during the course of the wheel travel. The objective is to locate the regions inside the granular media with high concentrations of force chains that can lead to soil failure. This work provides a glimpse into the performance of the robot appendage and the soil.

The rest of the chapter is organized as follows. In Section 3.1, the author describes the DEM modeling details for the test bed and the lugged wheel and in the next Section 3.2, metrics that are used to evaluate the performance of the lugged wheel are presented. Subsequently, in Section 3.3, the results obtained with angular velocity based wheel control are presented and discussed. The effect of the control mode (i.e., angular velocity-based control and slip-based control) is examined in Section 3.4. Finally, conclusions are drawn together and presented in Section 3.5.

Table 3.1: Nomenclature describing the quantities for lugged wheel and granular media

r	Radius of soil particle
μ_p	Friction coefficient for particle-particle interaction
μ_b	Friction coefficient for particle-wall interaction
μ_w	Friction coefficient for particle-wheel interaction
R	Nominal wheel radius
L_h	Length of lug
L_w	Width of lug
L_n	Number of lugs
M_w	Mass of wheel
I_p	Inertia of granular media particle
I_w	Inertia of wheel
W	Fraction of the robot weight carried by wheel
T_c	Traction control on wheel
T_l	Traction load on wheel
Db	Drawbar pull
τ_{input}	Driving torque of wheel
ω	Angular velocity of wheel
$F_{R,x}$	Reaction force on wheel exerted by soil in x-direction
$F_{R,y}$	Reaction force on wheel exerted by soil y-direction
τ_R	Reaction torque on wheel exerted by soil
S	Slip ratio
Tr_g	Gross traction of wheel
η	Traction efficiency of wheel

3.1 Lugged Wheel Interactions with Granular Media

Here, as aforementioned, the author has investigated dynamics of a lugged wheel's interaction with soft soil by using numerical studies. Sinkage, slip, traction, and power consumption of the wheel are studied as wheel performance metrics. The wheel performance is influenced by many factors such as terrain properties, wheel configuration, and wheel control mode among others. An optimal combination of the parameters that helps maximize the traction and minimize the power consumption, sinkage, and slip ratio is desired. To study this, numerical simulations are conducted for two different control modes namely, an angular velocity-based wheel mode and a slip-based wheel control mode. A two-dimensional (2D) DEM model similar to the one employed by Nakashima et al. [2007] is used to simulate the lugged wheel interactions with soft soil is used here.

The lugged wheel is also modelled with DEM elements wherein, the lugs are represented by overlapping circular DEM elements to better approximate the planar surface. The forces and torque on the wheel include the reaction forces and torques that arise due to contact with the granular media. The external forces on the wheel include the gravitational force and the traction load. The wheel is considered as a rigid body and each of the DEM elements of the wheel move with the same velocity. Reaction forces on the wheel are found as a summation of contact forces on each of the wheel particles determined independently.

The equations of motion of the wheel are as follows:

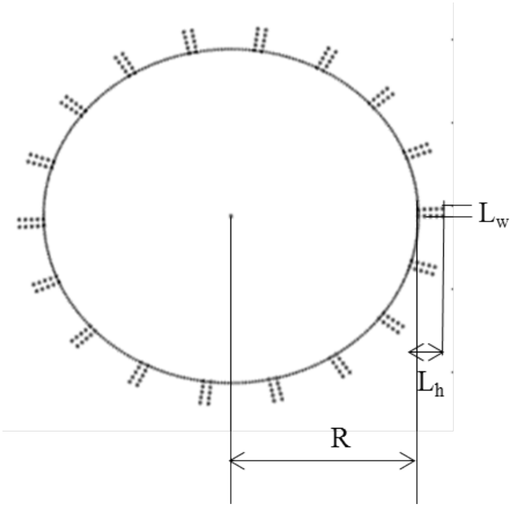

Figure 3.1: Lugged wheel.

$$M_w \frac{d^2 X_w}{dt^2} = \sum_c F_{R,x} - T_c \tag{3.1}$$

$$M_w \frac{d^2 Y_w}{dt^2} = \sum_c F_{R,y} - W \tag{3.2}$$

$$I_w \frac{d\omega}{dt} = \sum_c \tau_R + \tau_{input} \tag{3.3}$$

Here X_w and Y_w are, respectively, the X and Y coordinates of the center of the wheel; ω is the angular speed of wheel; $F_{R,x}$ and $F_{R,y}$ are respectively, the reaction forces from particles of the soil in X direction and Y direction; τ_{input} is the driving torque; T_c is the traction control on the wheel including the traction load T_l which is due to the payload carried by the robot; and W is the fractional load on the wheel due to the weight of the robot.

For the DEM simulations with the lugged wheel, a test bed consisting of

Table 3.2: DEM Parameters

r(m)	0.002
$K_n(N/m)$	10000
$K_t(N/m)$	500
$C_n(Ns/m)$	8.97
$C_t(Ns/m)$	2.01
μ_p	0.75
μ_b, μ_w	0.5
$Timestep$	10^{-4}

Table 3.3: Wheel Parameters

R(m)	0.1
$L_h(mm)$	$varied(10forwheel^{1})$
$L_w(mm)$	$varied(5forwheel^{1})$
L_n	18
$W(N)$	19.6
$M_w(kg)$	0.5

homogeneous particles surrounded by rigid walls is considered. The boundary walls are treated as a collection of circular particles and the interaction between granular media particles and the wall particles is modelled with DEM. In Table 2, the author has listed the DEM parameters of the soil, wheel, and walls. Stiffness, damping, and radius values are kept the same for wall particles, wheel particles, and the granular media particles. As discussed before, the parameters of DEM used for simulating lugged wheel locomotion are similar to the one employed by Nakashima et al. [2007]. The wheel parameters are listed in Table 3. In the simulations, the wheel is first allowed to sink and settle in the granular media, and later, the initial conditions are applied. The initial conditions include the angular speed or the slip ratio based on the type of wheel control mode selected. The wheel gains traction and moves on the granular media.

3.2 Wheel performance metrics

The locomotion performance of the wheel on the soil is assessed in terms of slip, sinkage, gross traction Tr_g , driving torque τ_{input} required by the wheel, power consumption, and traction efficiency η. The relationship between the wheel performance and the wheel parameters as well as the dynamic changes in the performance as the wheel travels on the terrain is explored hereafter. It is to be noted that in the plots for gross traction and slip shown in the following sections, the time series data have been filtered to remove noise while preserving important patterns but not necessarily the scale at all time steps. However, the filter parameters are kept constant for processing the data generated for all wheel configurations and control modes to provide an accurate comparative analysis. The performance metrics used in this study are defined by using equations (3.4)-(3.8).

$$s = \begin{cases} (1 - \frac{V_x}{R\omega}) \quad \text{for} \quad V_x < R\omega; \\ (\frac{R\omega - V_x}{V_x}) \quad \text{for} \quad V_x > R\omega \end{cases} \tag{3.4}$$

$$Tr_g = \sum_c F^+_{R,x} \tag{3.5}$$

$$Db = \sum_c F_{R,x} \tag{3.6}$$

$$Power = \sum_t \tau_R \omega \tag{3.7}$$

$$\eta = \frac{|\sum_t F_{R,x} V_x|}{|\sum_t \tau_R \omega|} \tag{3.8}$$

3.3 Angular velocity-based control

The input τ_{input} for the system is controlled according to the type of wheel control mode selected. For angular velocity-based control, the angular velocity of the wheel is specified and maintained constant throughout the simulation. To achieve a desired angular velocity, the driving torque τ_{input} is provided proportional to the difference in desired angular velocity and actual angular velocity. As discussed above, based on the dynamics of the wheel, the traction gained by the wheel is calculated from the reaction forces generated due to interaction with the granular media. For this control mode, the horizontal travel velocity of the wheel changes as the wheel travels and so does the slip ratio. Results for some representative initial conditions are presented later in this paper. It can be established that the same qualitative behavior holds for other initial conditions.

3.3.1 Force distribution in the granular media

In the granular media, the forces and stresses generated in the particles due to interaction with the wheel are transmitted between the particles through inter-particle contacts, see Peters et al. [2005], Zhang et al. [2017], and Sun et al. [2010]. Complex interactions between the particles of the granular media under the compression load and traction of the wheel results in formation of force chains and force networks. In Figure 3.2, the force distribution in the granular media during the wheel locomotion is shown. Figure 3.2 is a representative figure, which the author has used to show the entire test bed and the mechanism of visualization of the force chains used for all the subsequent figures showing force distributions. Particles with the same color experience approximately the same magnitudes of total forces. The forces are normalized with respect to a maximum force in the granular media in each frame to better visualize the force networks. As discussed before, the wheel is allowed to sink under gravity initially and then rotated at a constant angular velocity. The force distribution in the granular media during the initial phase of sinking is shown in Figure 3.2. In Figure 3.3, the author shows the force distribution in the granular media at different time steps as the wheel travels on the granular media.

In each of the frames of Figure 3.3, it is observed that the forces chains emerge from the particles interacting with the lugs and extend along the directions parallel to the respective lugs. As the lugs rotate along with the wheel, the contacts are formed between the lugs and the new particles. So, it appears as if the force chains are rotating along with the lug. Furthermore, it can be seen from Figures 3.2 and 3.3 that the strong networks of forces are found right below the wheel. Specifically, a concentration of high magnitude forces are found in particles located between the lugs that are inside the granular media. Among the particles that show stronger forces, some particles become part of the force chains. This can be observed in Figures 3.4 and 3.5, wherein the directions of total forces and contact forces acting on the particles are shown respectively. The author plotted directions of the resultant contact forces and total forces in the particles at different time steps as the wheel travels on the granular media. Directions associated with force values that are greater than 0.0003N have been plotted. It is observed that the concentrations of forces are larger in the frames showing contact forces compared to the ones showing total forces. This is because the contact forces are balanced by gravitational forces for some of the particles. Network transmission of forces within the granular media can be observed through contact forces in the particles. The total force gives an insight into the path of transmission of kinetic energy within the granular media.

The wheel performance metrics such as sinkage, traction, and slip are dependant on the force transmission between the soil particles and the wheel. Through these studies, the author brings to attention to how the author bring to attention how the corresponding reaction forces are generated on the particles due to interaction with the wheel travel and dissipate/disperse within the granular media. The number of force chains generated, dispersion, and length of the the force chains depend on the magnitude of the reaction forces generated and dissipation in the particles. In a closely packed medium such as the one used for the current simulations, the force chains generated at the lugs travel inside the granular media and towards the boundary walls in some instances. An example of such behavior can be found in the previous studies, wherein the impact force from the spherical projectile transmit inside the granular media all the way to the boundary walls and reflect therefrom [Zhang et al., 2017, Stoffel, 1998]. It can also be seen that during projectile–medium interactions, a cone volume is developed within the impacted medium in relation to the load diffusion properties. In these previous studies, the granular media is subjected to a singular impact whereas, with the locomotion of

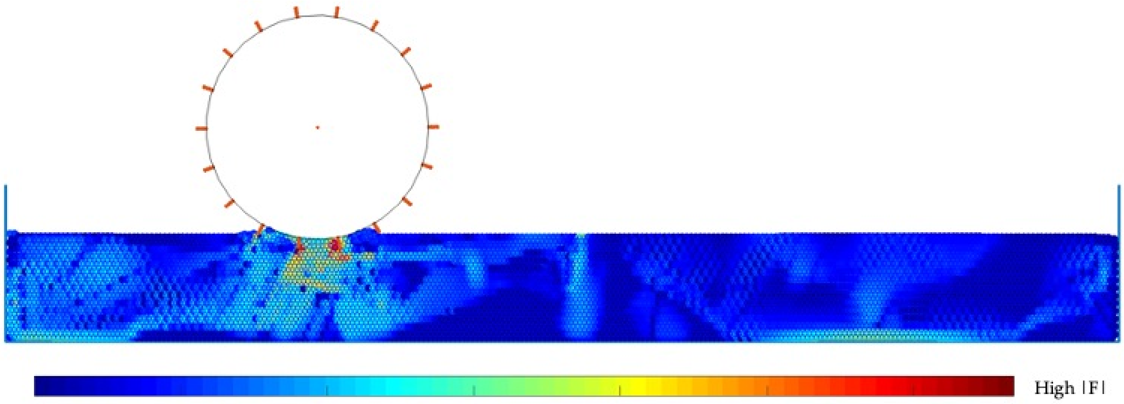

Figure 3.2: Force distribution inside the granular media captured during initial phase of sinking for a wheel with $L_h = 10$mm, $L_w = 5$mm, $\omega = 0.15$ rad/s, and angular velocity-based control.

lugged wheel, the granular media is subjected to a constant static load due to the weight of the wheel as well as the dynamic forcing due to locomotion of the wheel. As a result, the force chains observed show effects of dynamic forcing from wheel locomotion in addition to the cone volume with an approximate angle of 45 degrees that travels along with the wheel.

Due to the small test bed size, one can see reflections of forces from each of the walls surrounding the granular media. Although, the force distribution at the boundary correspond to those with smaller force magnitudes in comparison to the ones directly under the wheel, the results prompt further studies on the effects of boundaries on wheel performance.

3.3.2 Lug length

By using angular velocity-based control, DEM simulations were performed for a range of lug lengths with a fixed lug width of 8.5 mm and constant angular velocity of 2 rad/s. Plots for wheel performance parameters for different lug lengths

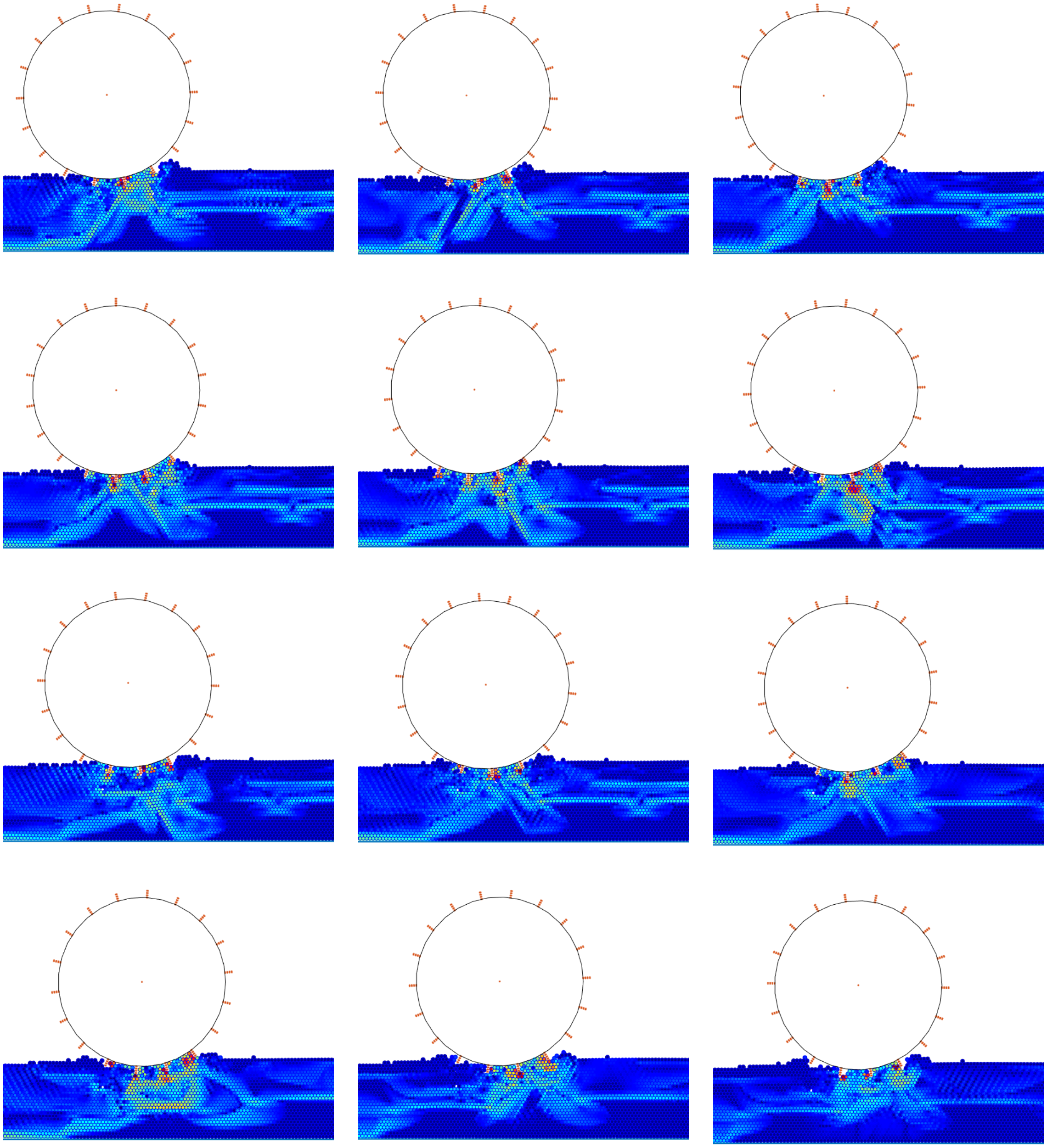

Figure 3.3: In each frame, force chains inside the granular media are shown. These frames are captured at regular intervals of 0.5 seconds, starting from left to right in each row, for a wheel with $L_h = 10\text{mm}$, $L_w = 5\text{mm}$, $\omega = 0.15$ rad/s, and angular velocity-based control.

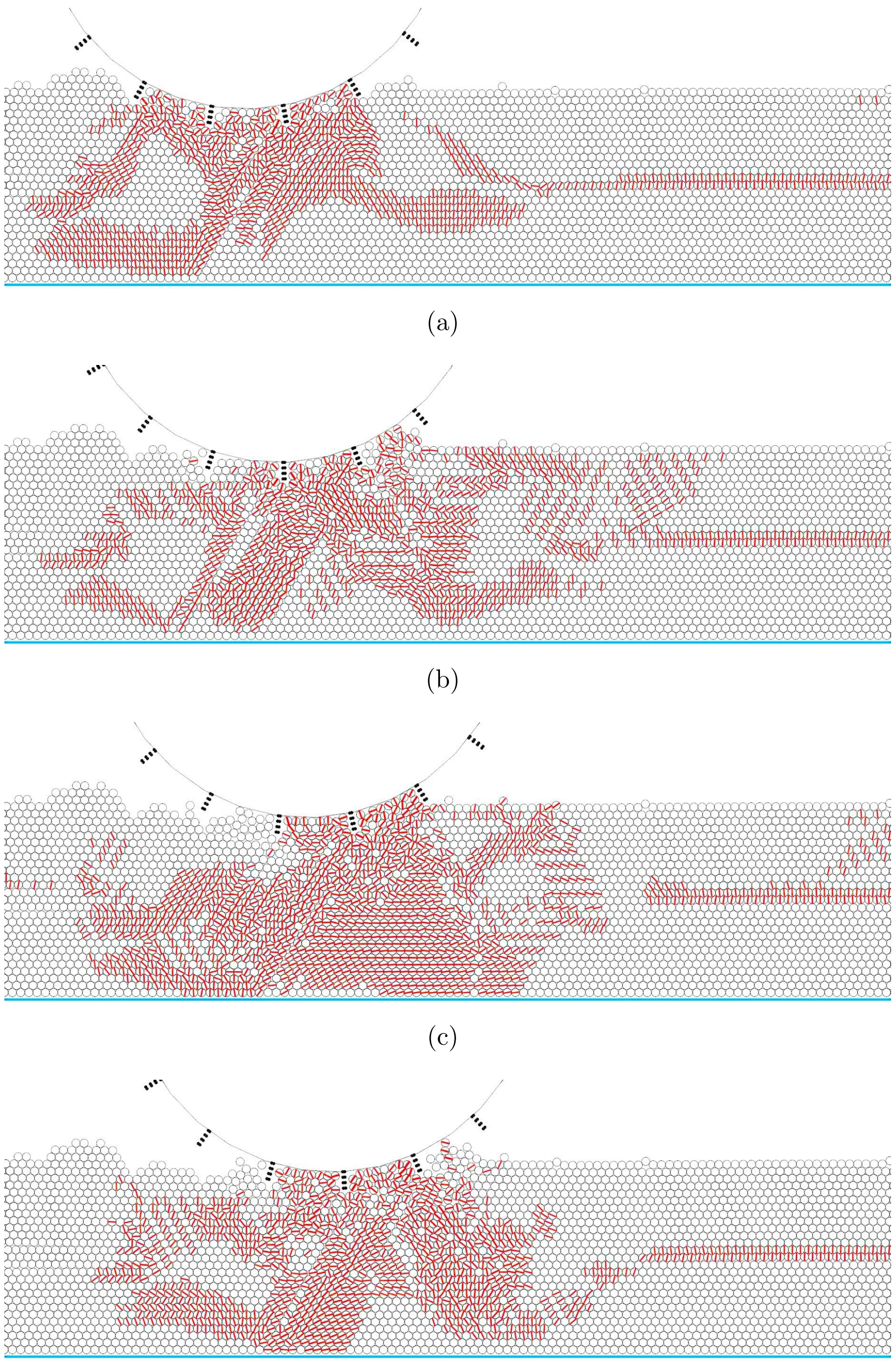

(a)

(b)

(c)

(d)

Figure 3.4: A representation of the directions of total forces inside the granular media are shown. These frames are captured at regular intervals of 0.008 seconds, for a wheel with $L_h = 10\text{mm}$, $L_w = 5\text{mm}$, and $\omega = 2$ rad/s.

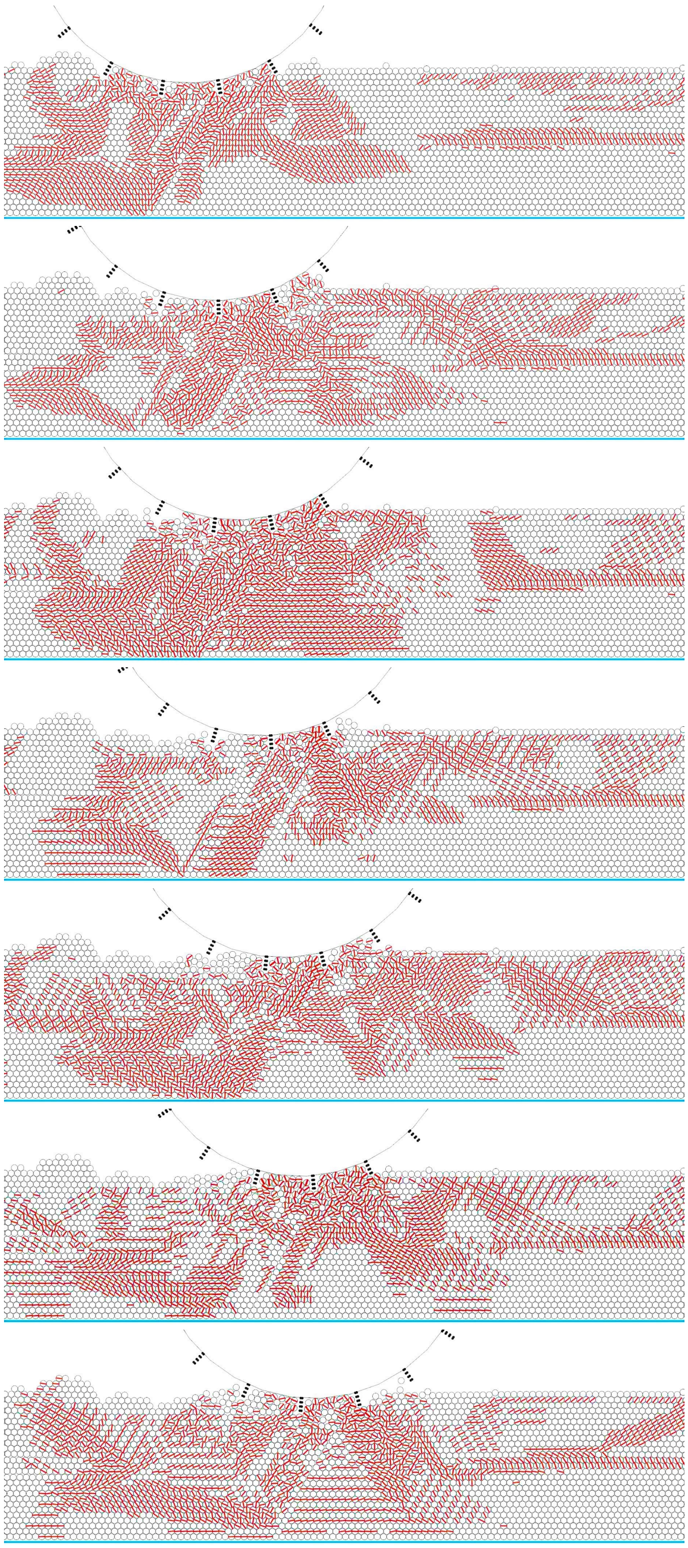

Figure 3.5: A representation of the directions of contact forces inside the granular media are shown. These frames are captured at regular intervals of 0.008 seconds, for a wheel with $L_h = 10$mm, $L_w = 5$mm, and $\omega = 2$ rad/s.

are shown in Figure 3.6. The results indicate that the average sinkage, gross traction, and traction efficiency increase monotonically with an increase in lug length for the angular velocity-based control of the wheel. However, no monotonic behavior can be observed from this data for the power consumption of the wheel with respect to the lug length. Furthermore, a linear relationship can be established between the performance metrics and the lug length.

A visualization of the force distributions generated within the granular media during interaction with the lugged wheel is presented. Wheel performance parameters and particle distributions and maximum forces in the soil over time are shown for two different lug lengths of 8.5 mm and 17 mm in Figure 3.7 and for different lug lengths of 5 mm and 13 mm in Figure 3.8. The results indicate that the granular media has a higher magnitude of forces as well as higher force concentrations due to interactions with lugs of larger lengths. Theoretically, if the stress/force concentrations inside the soil are higher the soil starts to flow causing the wheel to sink further. The DEM results also support this behavior, which can be observed from sinkage and particle distribution plots for the different lug lengths shown in Figure 3.7 and Figure 3.8. For the wheel with larger lug length, the number of particles with higher force are consistently larger compared to the wheel with smaller lug length and so is the sinkage. In Figures 3.9 and 3.10, the force distributions in the granular media are shown at different time steps as the wheel travels on the granular media for two different lug sizes. For the granular media interacting with larger lugs (see Figure 3.9), the force network is relatively denser and contains longer force chains, while the force network is concentrated mostly in the forward path of the

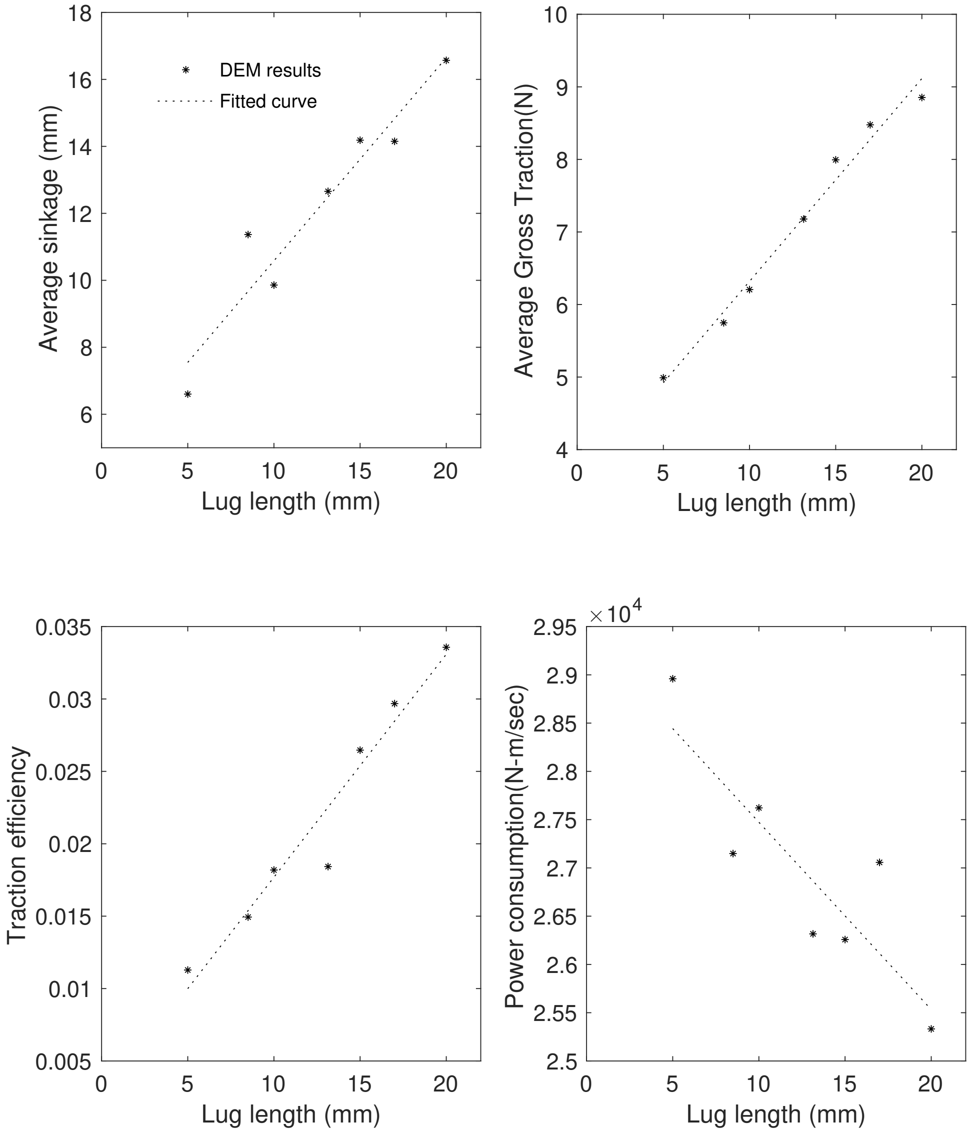

Figure 3.6: Wheel performance for different lug lengths.

wheel for the granular media interacting with smaller lugs (see Figure 3.10).

3.3.3 Lug width

With angular velocity-based control, DEM simulations were carried out for a range of lug widths and fixed angular velocity of 2 rad/s and lug length 10 mm. The average sinkage, average gross traction of the wheel, traction efficiency, and power consumption determined for each of the lug widths are plotted in Figure 3.11. The DEM results indicate that there is no monotonic behavior between the wheel performance and the lug width. The time histories for sinkage, gross traction, force distribution of particles, and maximum forces in the granular media for two different lug widths are presented in Figures 3.12 and 3.13 and compared. It can be observed that for a fixed lug length of 10 mm, the sinkage is higher for the smaller lug width of 5 mm when compared to the lug width of 10 mm. However, for a fixed lug length of 15 mm, the sinkage is less for the smaller lug width of 8.5 mm when compared to the lug width of 13.2 mm. The soil performance can be discerned from the evolution of particle distributions and maximum forces in the soil over time for the different lug widths shown in Figures 3.12 and 3.13. Wheels with a larger width generate higher forces as well as larger force concentrations in the soil.

3.3.4 Traction Load

DEM simulations were carried out for a range of traction loads T_l on the *wheel*[1] under angular velocity-based control. For these simulations, the angular speed was

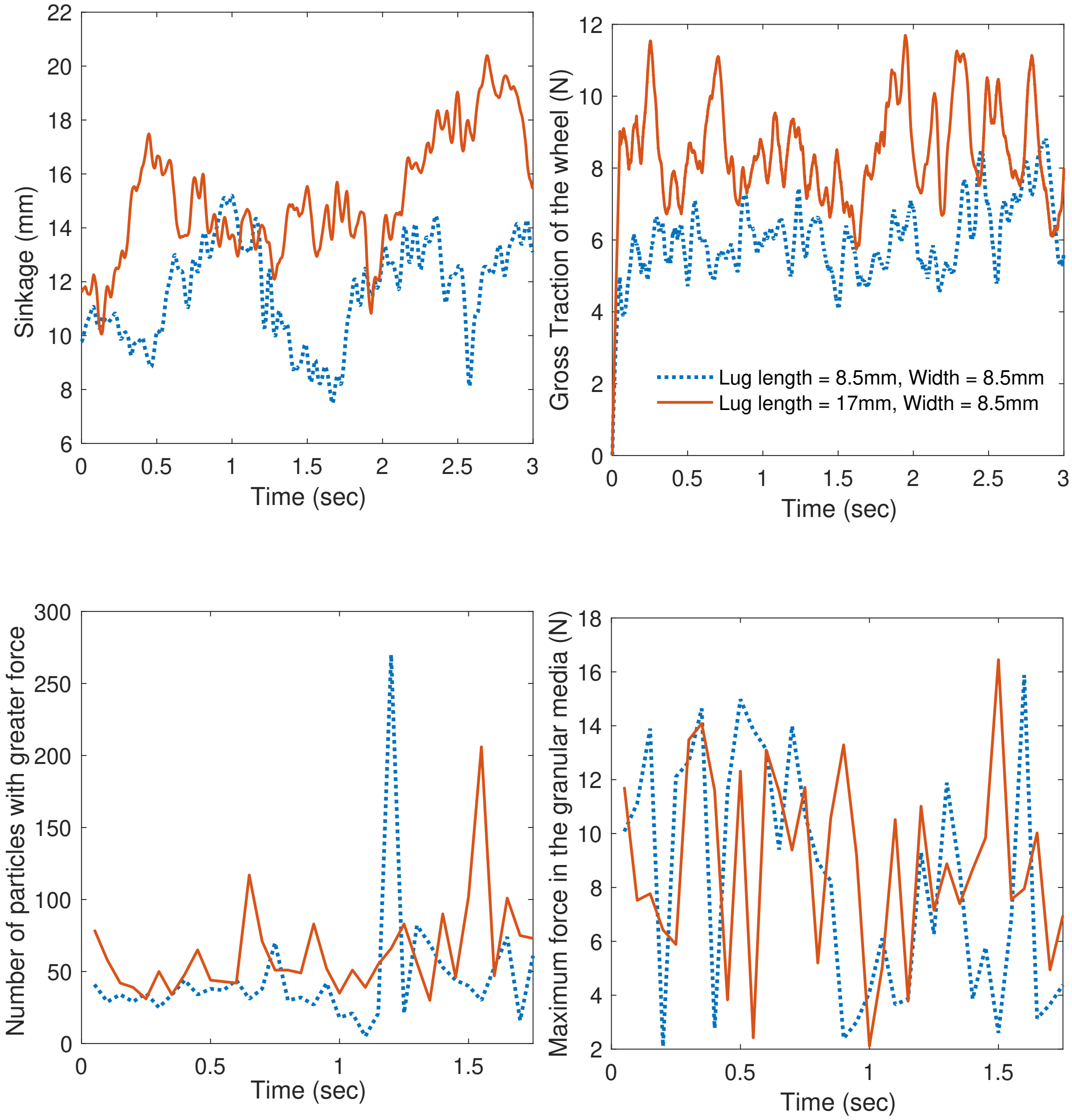

Figure 3.7: Time histories for sinkage, gross traction, force distribution of particles, and maximum forces in the granular media are compared for the two different lug lengths of 8.5 mm and 17 mm.

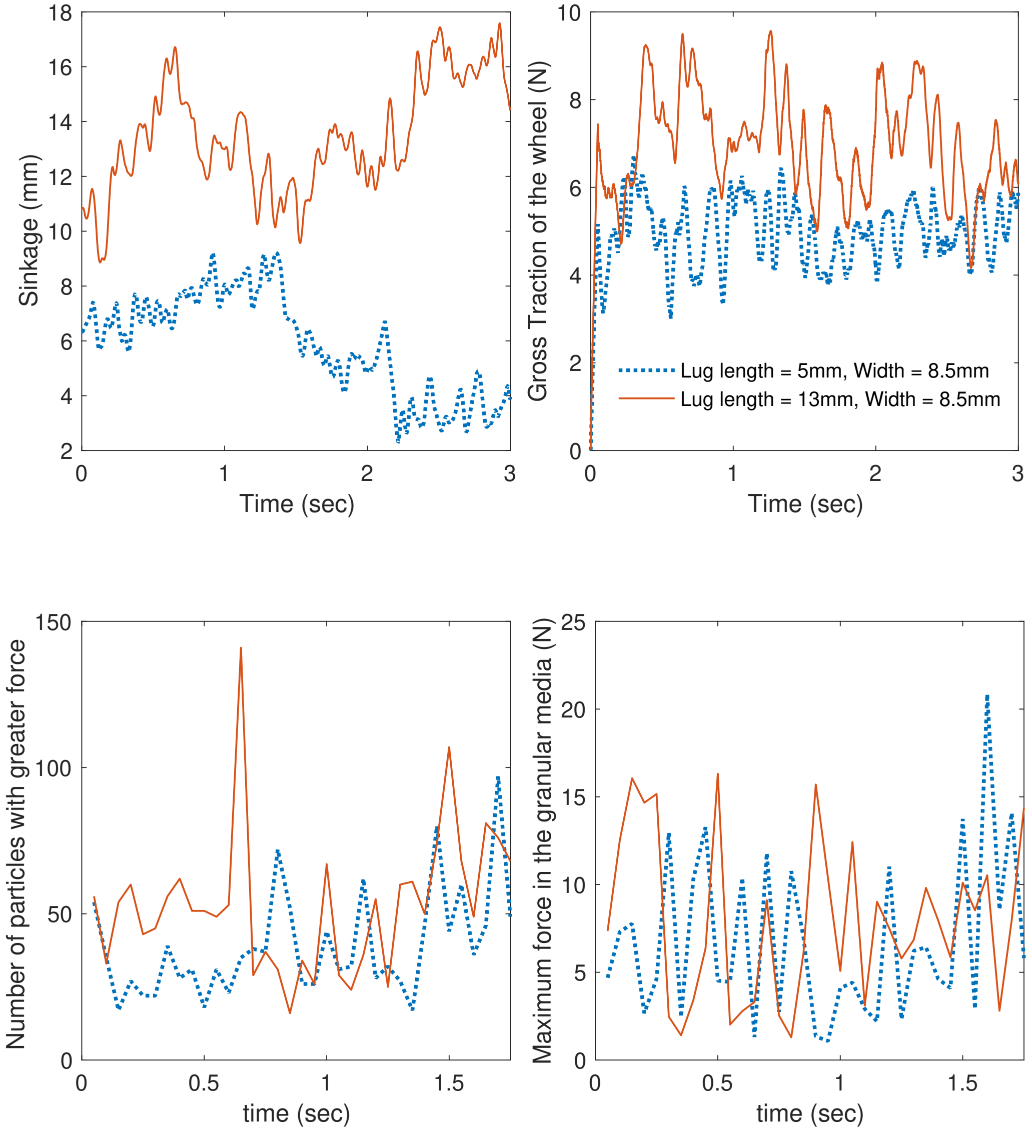

Figure 3.8: Time histories for sinkage, gross traction, force distribution of particles, and maximum forces in the granular media are compared for the two different lug lengths of 5 mm and 13 mm.

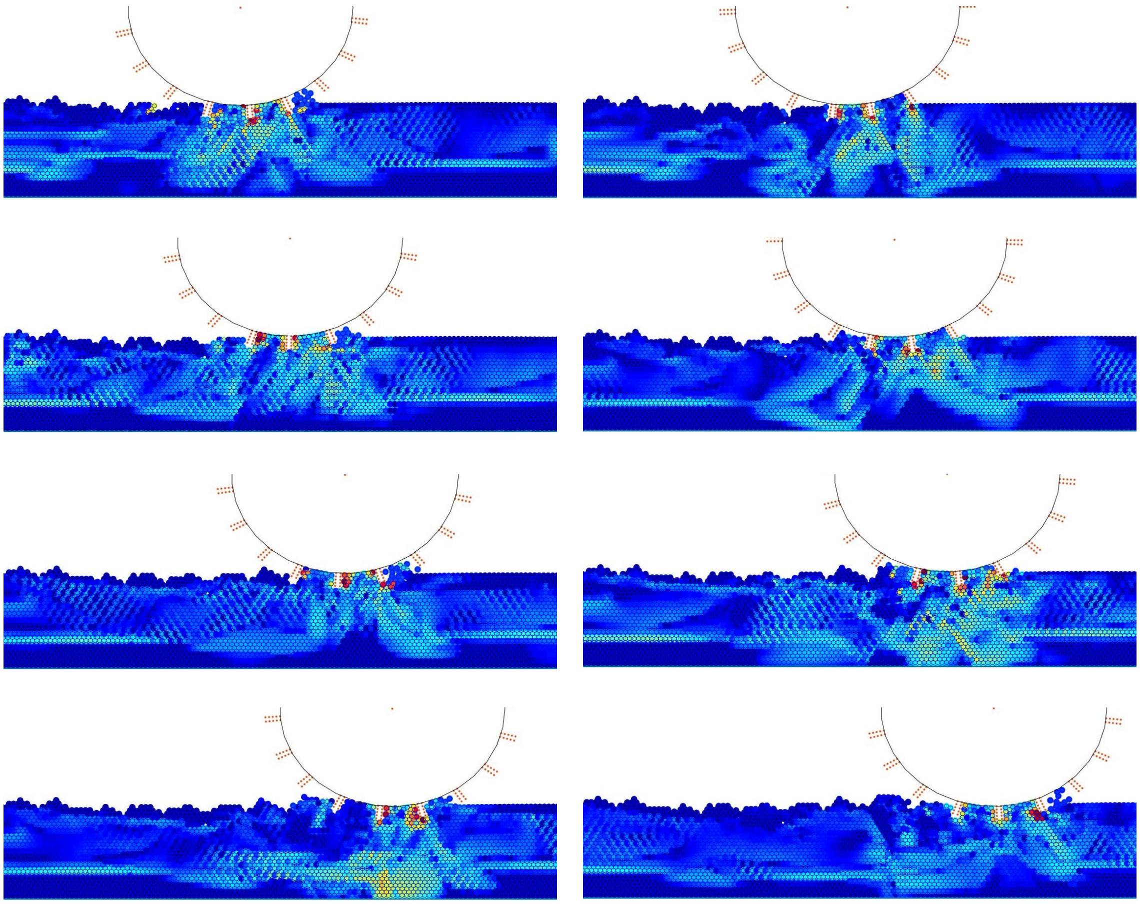

Figure 3.9: In each frame, force chains inside the granular media are shown. These frames are captured at regular intervals of 0.1 seconds, starting from left to right in each row, for a wheel with lug length = 15 mm, width = 8.5 mm, rotation speed = 2.00 rad/s, and angular velocity-based control.

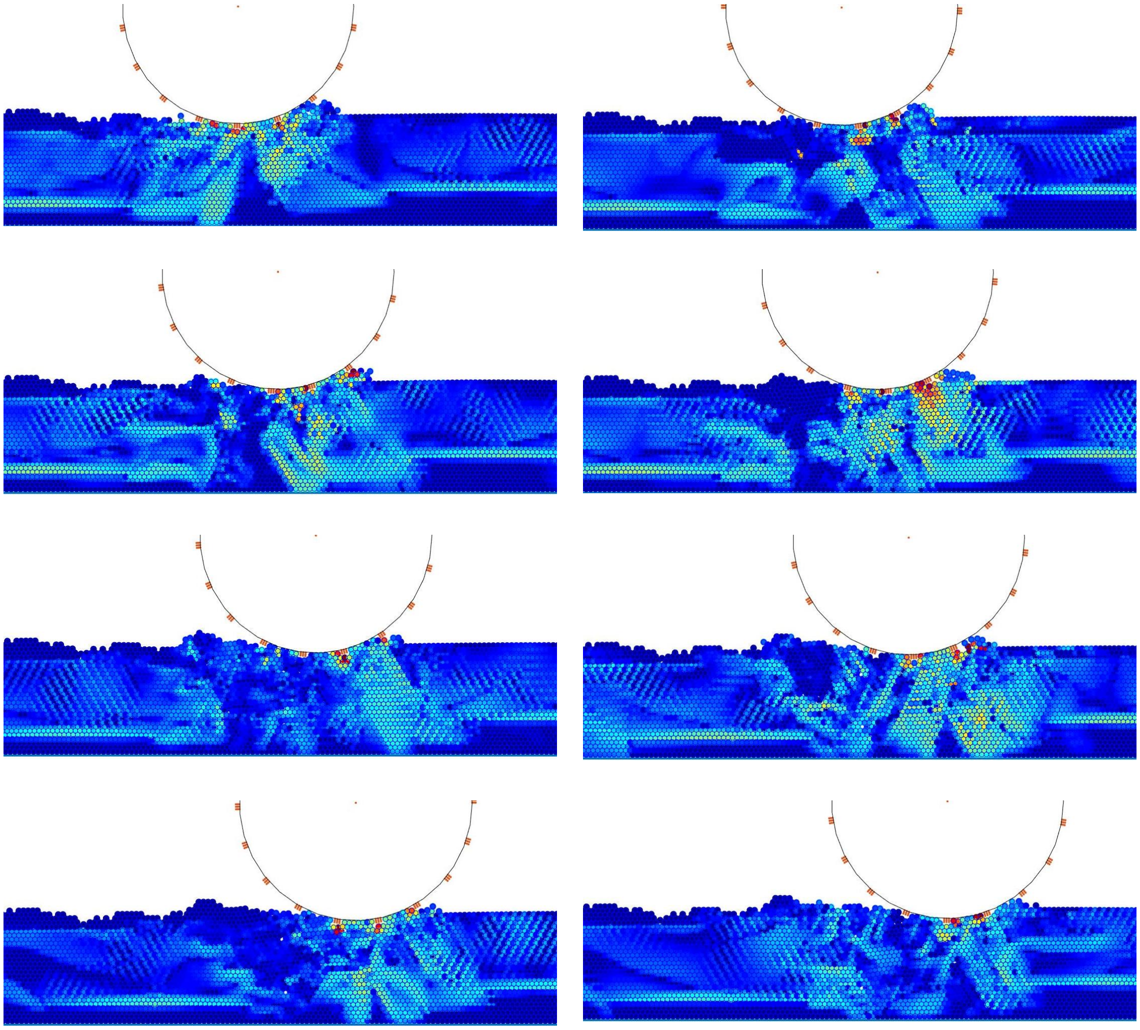

Figure 3.10: In each frame, force chains inside the granular media are shown. These frames are captured at regular intervals of 0.1 seconds, starting from left to right in each row, for a wheel with lug length = 5 mm, width = 8.5 mm, rotation speed = 2.00 rad/s, and angular velocity-based control.

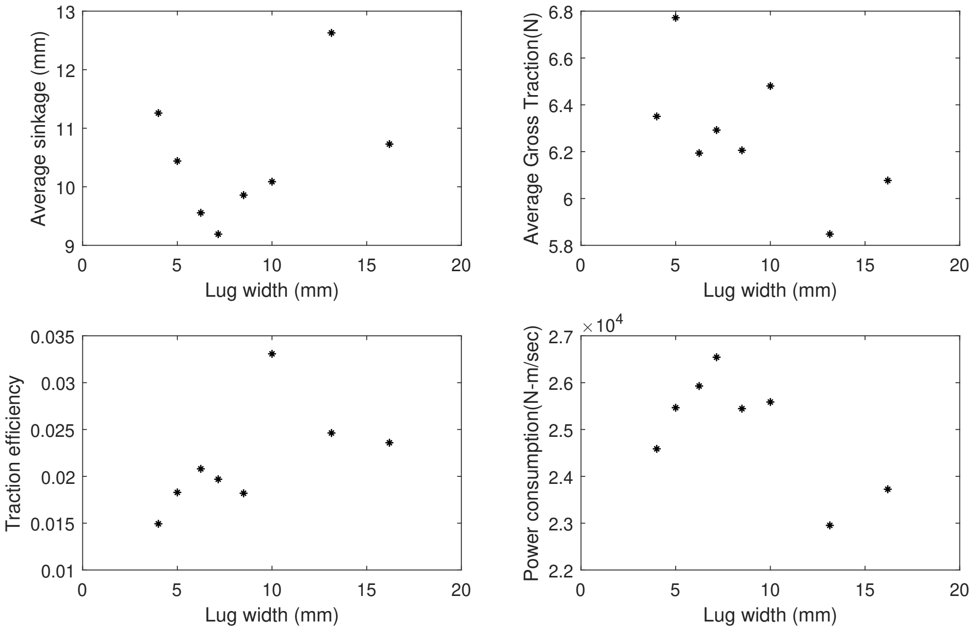

Figure 3.11: Wheel performance for different lug widths.

fixed at 2 rad/s. The average sinkage and average gross traction of the wheel are plotted in Figure 3.14. The results indicate that the gross traction increases with the traction load on the wheel whereas the sinkage decreases with the traction load, as can be seen from Figure 3.14. Furthermore, a linear relationship can be established between the traction load and the gross traction for the angular velocity-based wheel control. In Figure 3.14 c), the time series plots for the sinkage of the wheel are shown for traction loads of 2.5 N, 4.9 N, 9.8 N, and 12.25 N. In Figure 3.15, the time series plots for wheel slip and gross-traction are shown for traction loads of 2.5 N, 4.9 N, 9.8 N, and 12.25 N. The sinkage for the wheels for the different traction loads all have the same initial value and the difference in the sinkage from one case to another increases over time.

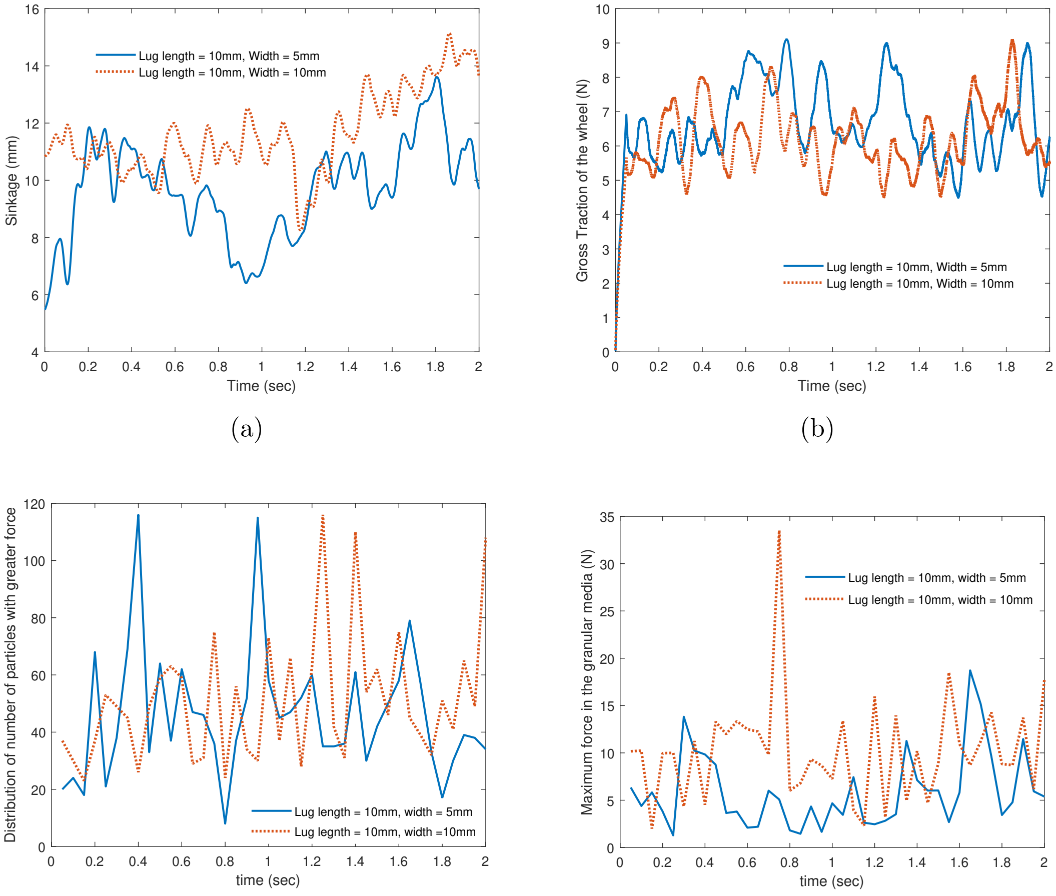

(a) (b)

(c) (d)

Figure 3.12: Time series plots: a) sinkage b) gross traction c) force distribution of particles and d) maximum forces in the granular media are compared for two different lug widths of 5 mm and 10 mm.

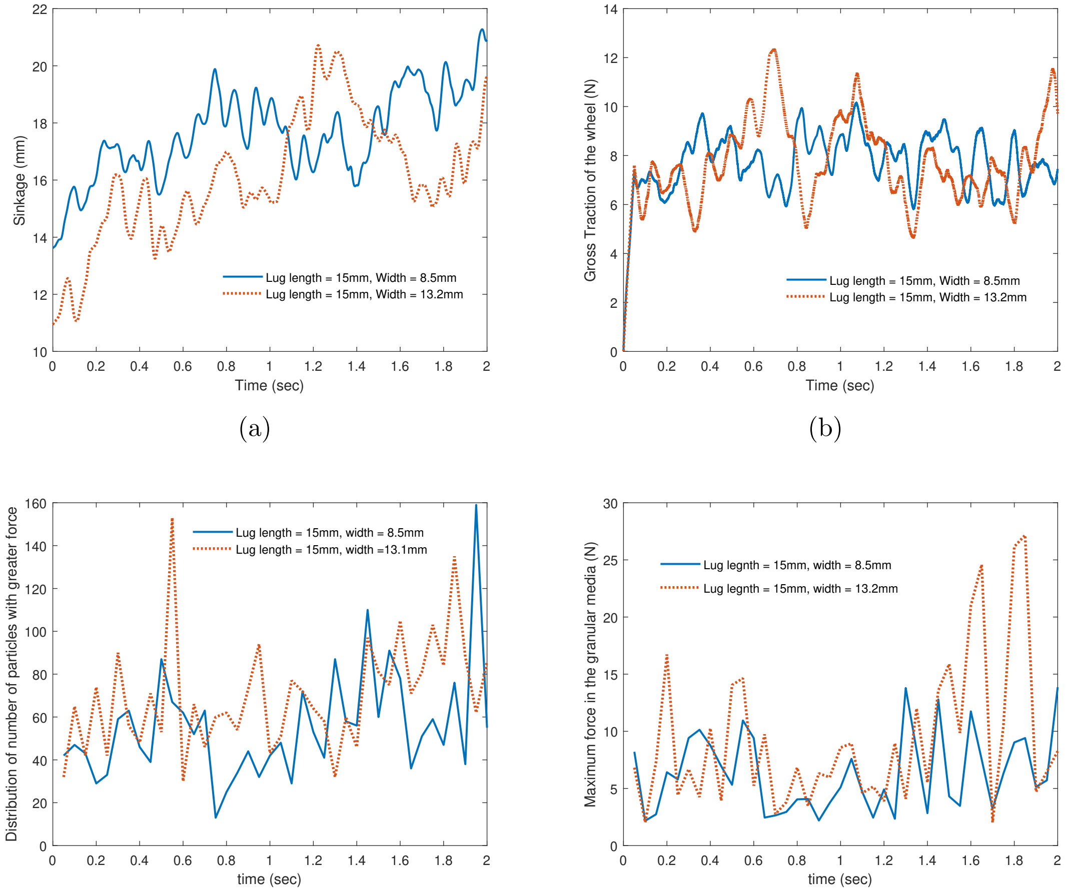

(a)

(b)

(c)

(d)

Figure 3.13: Time series plots: a) sinkage b) gross traction c) force distribution of particles d) and maximum forces in the granular media are compared for two different lug widths of 8.5 mm and 13.2 mm.

3.4 Effect of Control Mode

For DEM simulations with slip-based control mode, the wheel operates at a desired slip ratio, which is maintained constant by controlling the wheel angular speed ω and the wheel longitudinal speed V_x. The reaction forces on the wheel due to interaction with the granular media vary with time. As discussed before, with angular velocity based control, a constant traction load is input to the wheel, as such, the slip ratio changes with time. With slip based control, the horizontal load on the wheel is varied to achieve a constant slip ratio. To make a comparison between the results obtained with the two control modes, simulations are carried out with same values of initial angular speed and wheel parameters. For slip control, the results are evaluated for low-slip ratios ranging between 0.1 and 0.4. For the same values of initial angular speed, the performance parameters obtained from simulations are compared for the two different control modes.

In this section, DEM results with slip-based control and angular velocity-based control are presented for different lug sizes. With slip-based control, the DEM simulations were carried out for a range of slip ratios T_l for $wheel^1$. In Figure 3.16, travelling characteristics of the wheel are plotted for two different slip ratios of 0.15 and 0.3. The results indicate that the wheel has higher gross traction and net traction when operated at a higher slip ratio. In Figure 3.17, a comparison is provided between the wheel performance obtained for the lug lengths 10 mm and 15 mm at different slip ratios. The DEM results indicate that there is a large difference between performance for lower slip ratios and the values converge as the slip ratio increases.

3.5 Concluding remarks

The locomotion performance of a lugged wheel is largely dependent on the dynamic interactions of the lug with the soil and how the soil flows under the wheel. Here, the wheel performance has been evaluated for two different wheel control modes, namely, angular velocity-based control and slip-based control. It is found that by increasing the wheel lug length, one can improve the wheel performance under angular velocity-based control, whereas non-monotonic behavior is observed for wheel performance with respect to the lug width. With an increase in the traction of load on the wheel, there is a decrease in the sinkage and an increase in the gross traction of the wheel. For small slip ratios, it is found that the wheel performance is about the same with both the angular velocity-based control and slip-based control. The effect of control mode, traction loads and lug sizes on the wheel performance have also been examined. The results of these studies are expected to provide an insight into the complex interactions of granular media with the wheel and so are significant to the design and control of robots moving on deformable surfaces.

In these studies, the author also shows a visualization of the forces generated on the particles due to interaction with the wheel. Soil performance has been evaluated in terms of force networks and force distribution in the soil and compared for different wheel configurations. The force networks originated inside the soil due to interaction with the wheel consist of both longitudinal and transverse force chains.

These force chains rotate along with the lug and travel to the boundaries. The relationship between the force distribution in the soil and the wheel performance has been investigated for different wheel parameters. It is observed that the wheel sinkage increases with an increase in the force concentrations inside the granular media soil. Further analysis is necessary to quantify this relationship. While it may be difficult to establish the absolute behavior of the soil with the results shown, the author's focus is on comparing and relating the force distributions in the soil to wheel performance for different wheel configurations and a selected granular media setting. It is expected that the studies presented here could provide insights into the wheel performance, force transmission between the wheel and soil and how this transmission varies for different wheel configurations and control modes.

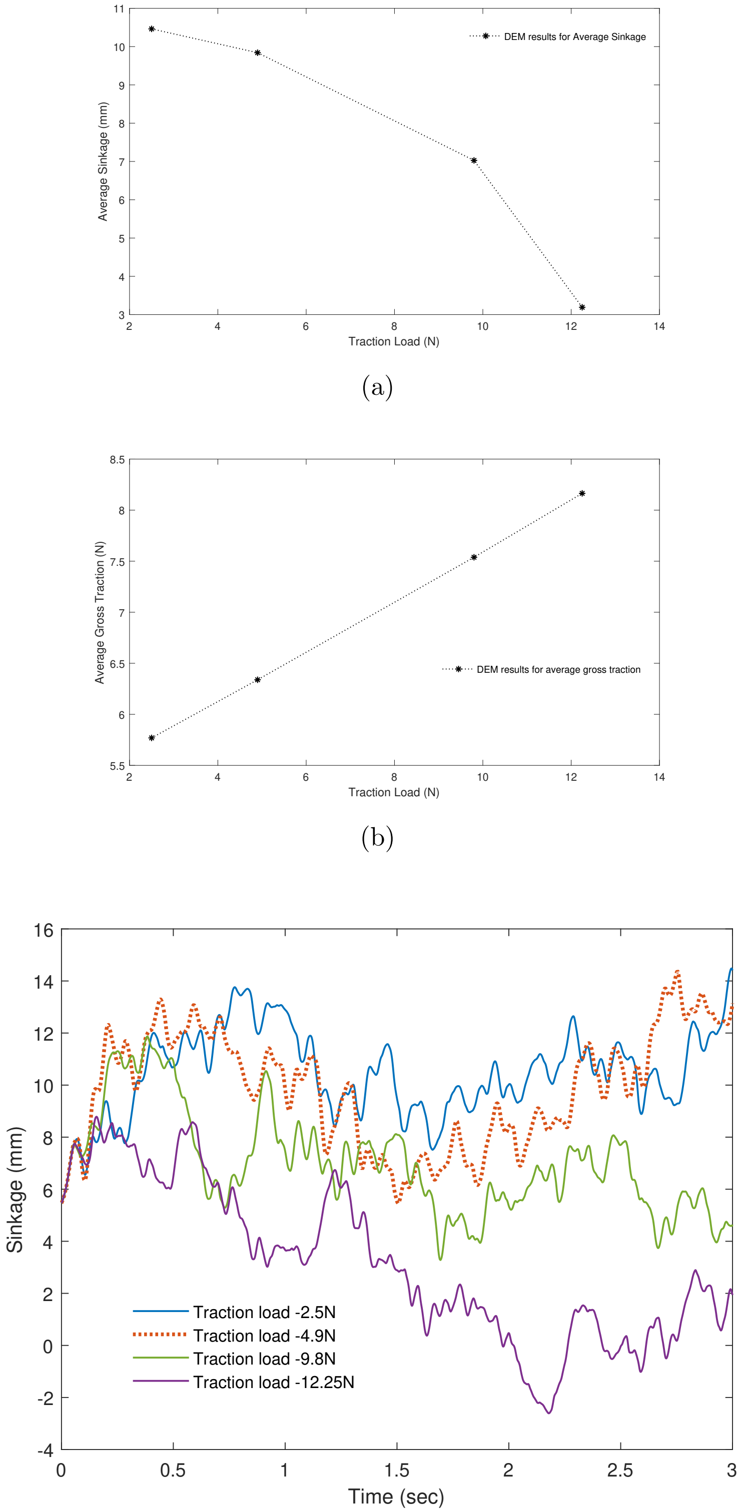

(a)

(b)

(c)

Figure 3.14: a) Average sinkage, b) average gross traction, and c) Time series plots for sinkage of the wheel for angular speed of 2 rad/s and different traction loads 2.5 N, 4.9 N, 9.8 N, and 12.25 N.

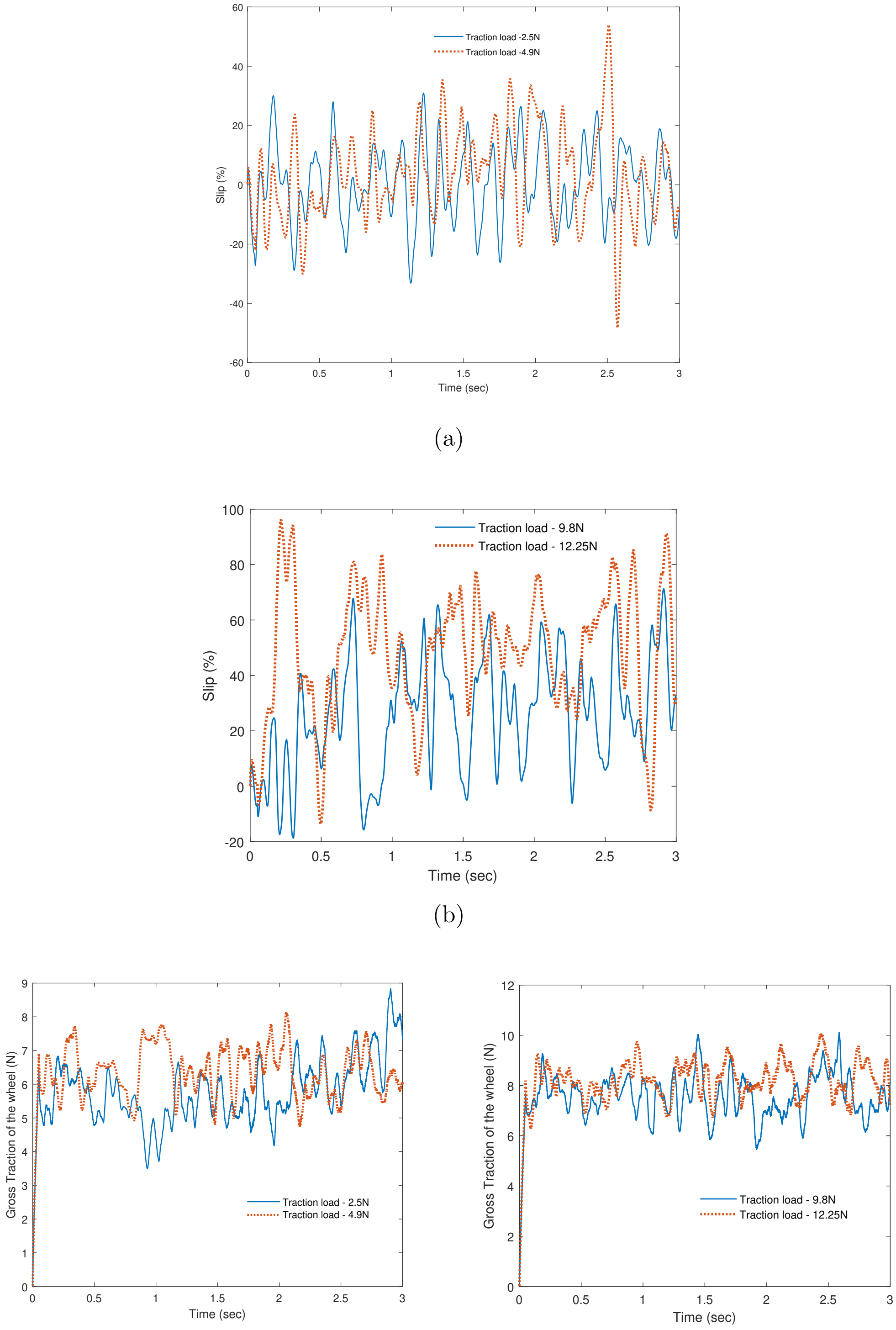

(a)

(b)

(c)

(d)

Figure 3.15: Slip and gross traction time histories shown for different traction Loads 2.5 N, 4.9 N, 9.8 N, and 12.25 N.

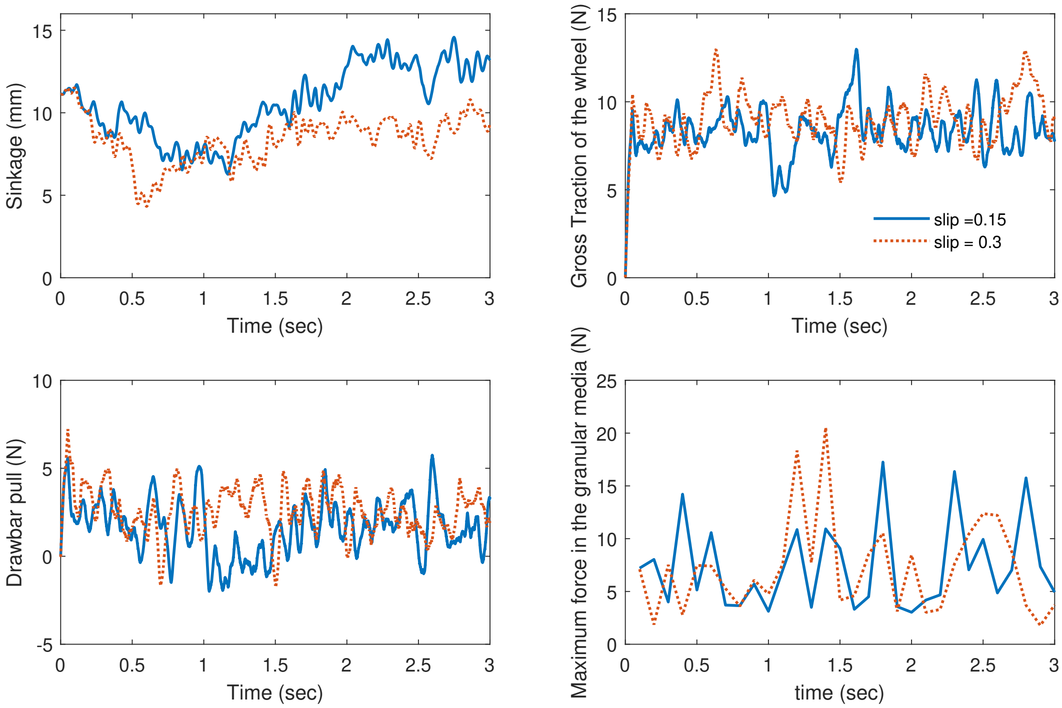

Figure 3.16: Time series plots for sinkage, gross traction, drawbar pull, and maximum forces in the granular media are compared for two different slip ratios 0.15 and 0.3 with slip-based control.

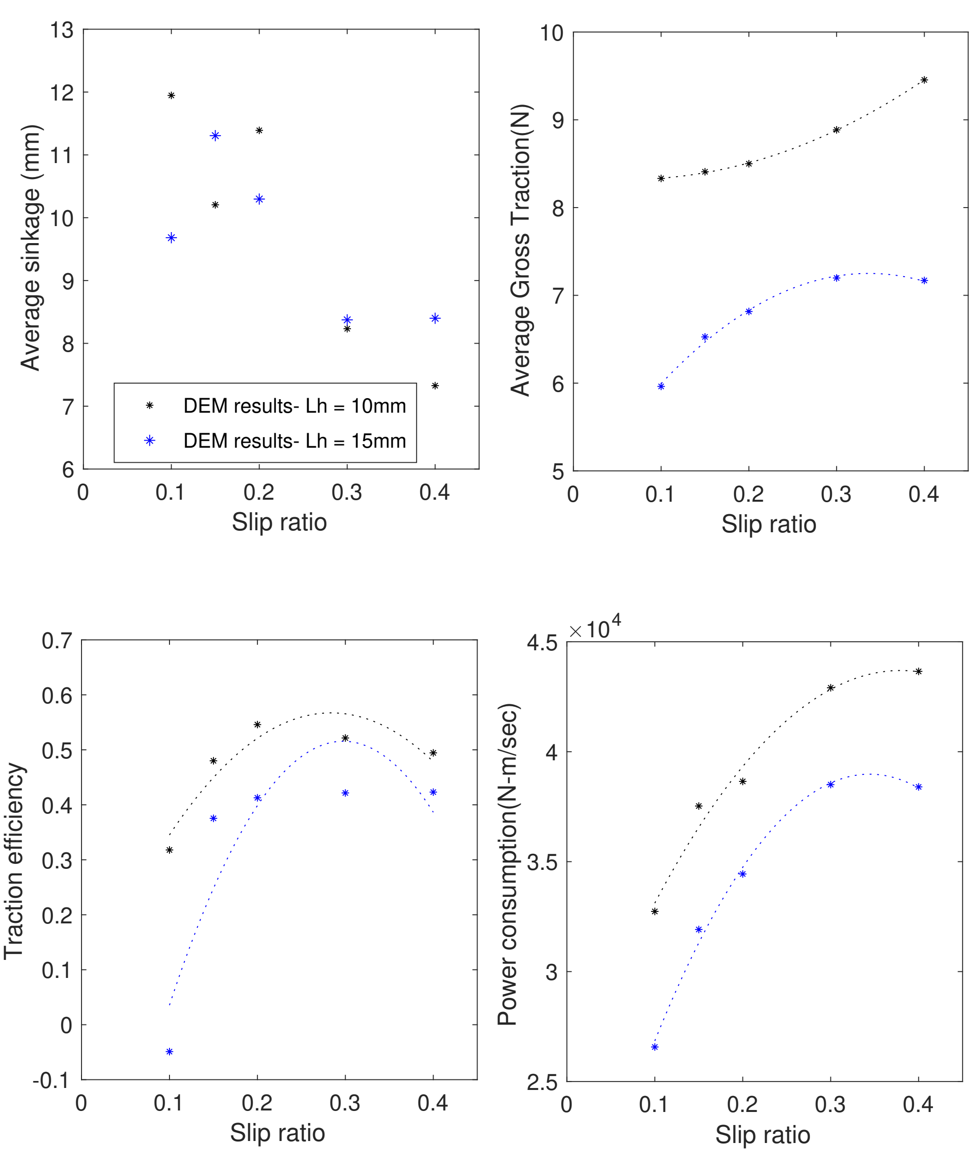

Figure 3.17: Wheel performance versus slip ratio for different lug lengths of the wheel with slip-based control.

Chapter 4: Experiments with photoelastic media

The behavior of granular media can be represented across three length scales; that is, micro-scale, meso-scale, and macro-scale. Sun et al. [2009] proposed a multi-scale methodology for granular media and revealed a number of correlations between the different scales. At the micro-scale, inter-particle forces between the particles are of interest, whereas, at the meso-scale, force chains are determined by the particle properties such as friction, and at the macro-scale, bulk behavior of granular media is of interest. A correlation between the three length scales can be observed, for example, evolution of force chains arising from the particle-scale interactions may contribute to the non-local behavior that is observed across the macro-scale. Furthermore, the transitions between different states of the granular media observed at the macro-scale is influenced by the particle properties. Correlations between different scales and an improved understanding of the granular behavior at these individual length scales are crucial to develop comprehensive models for granular media. In this dissertation work, the author's focus is on investigating the micro-scale and the meso-scale behavior of the granular media under dynamic loading conditions.

As mentioned in the previous chapters, the author has used DEM that is known to accurately represent the complex behavior of granular media at micro-scale to conduct studies on locomotion of robot appendages on granular media. Further, the author has reported on the inter-particle forces, force chains arising due to the inter-particle contacts, and the influence of the force transmission of granular media on the locomotion performance of robot appendages. To further investigate the force chains and evolution of force chain networks, the author has conducted experiments using photo-elastic particles as reported in the work of Acar et al. [2021] and Ravula and Balachandran [2021]. Specifically, the author has conducted experiments with two different designs of robot appendages, namely, a lugged wheel and a single actuator pendulum. Upon interaction with the robot appendages or any other solid intruder, the energy within the granular media propagates through a chain/network of contacts between particles, and eventually dissipates. Of particular interest is how the force networks evolve under dynamic loading, what are the regions of high stress concentrations and the parameters influencing the force distribution within the granular media. The experimental studies can be used to make quantitative advances in understanding granular media interactions.

The rest of the chapter is organized as follows. In Section 4.1, the author describes the design and setup of the lab-scale experimental arrangement. Subsequently, in Section 4.2, experimental arrangement for investigating lugged wheel motion on photo-elastic granular media is described. Further, the experimental results on qualitative and quantitative measures that describe the interaction between the lugged wheel and granular media are presented. Conclusions on lugged wheel motion are drawn together and presented. In Section 4.3, experimental studies on force networks and particle motion during interaction with a single-actuated pendulum are presented followed by a comparison between the experimental and numerical results. Finally, conclusions are drawn together and presented.

4.1 Experimental Setup and Procedure

As discussed before, the author's focus for the experimental studies is on evolution of force chains/networks inside the granular media under dynamics loading. In order to visualize the force chains, photoelastic particles are utilized for the experiments. Photoelasticity describes change in optical properties due to mechanical deformation, for example, the work of Hearn [1997], and is widely used in experiments to quantify internal stress distribution in solid objects. Photoelastic materials show fringe patterns when deformed (see Figure 4.1), which is directly related to the stresses and strains. Under polarized light, the fringe patterns in the photoelastic materials can be observed. In the literature, photoelasticity is used in experiments on crack propagation and mechanical failure, for example, the work of Dally [1979], since this helps obtain a clear indication of high-stress locations, and low-stress regions inside the material.

Dielectric media such as, polyurethane rubber and glass are photoelastic in nature and can be used as an idealized substitute for granular media. To produce the particles, 4.76 mm-thick polyurethane rubber sheets are used. The material has a 60A hardness and 20.7 MPa tensile strength. The particles are punched out from the sheet material using a pair of 14-mm diameter dies. For a collection

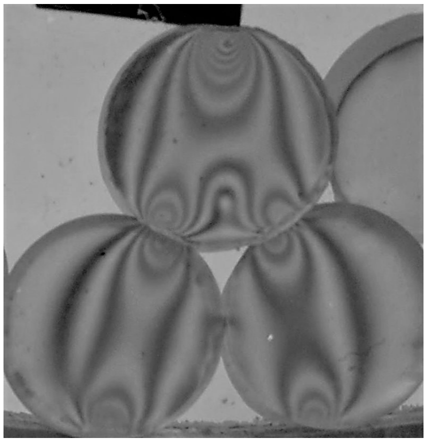

Figure 4.1: A set of photoelastic particles under forcing. The force distribution inside the particles is determined by the fringe pattern and the number of alternating bright and dark fringes.

of circular particles as shown in Figure 4.1, one can see the stress concentration around the contact points, and deduce the force networks through the distribution of interference patterns. The number of fringes increases monotonically with the applied force, and the forces inside the particles can be deduced from the number and pattern of fringes [Zadeh et al., 2019].

High-speed imaging that allows recording images/videos of fast phenomena, is employed to capture the evolution of force networks in photoelastic particles. As shown in the schematic of the experimental setup illustrated in Figure 4.2, the experimental arrangement includes a test bed for holding the photoelastic particles. The test bed consists of two (2 ft × 4 ft) clear acrylic panels, where the gap between the two panels is adjustable from 5mm to 250mm, depending on the thickness and the configuration of the particles. The test bed is filled with photoelastic rubber particles of thickness 5mm are used to study the granular interactions. Accordingly, the gap between the acrylic panels is adjusted to 5 mm in order to ensure that the photoelastic particles are placed in a single plane, which allows one to visualize force networks in 2D.

Two circular polarizer sheets are attached the test bed, one on each of the exposed side of the acrylic panels. After passing through the first polarizer sheet, the light becomes polarized. As the photoelastic particles used here are birefringent, the refractive index depends on the polarization and propagation direction of light. Further, for stressed particles, the birefringence depends on the local stress state. So, next, as the light polarized from the first sheet passes through the photoelastic media that is sandwiched between the acrylic sheets, the birefringence of the media causes the light to rotate its polarization. The intensity of light after passing through the second polarizer varies based on the local stress in the photoelastic media which can be observed as bright and dark fringes.

Capturing videos using High-speed camera at a higher frames per second(fps) requires a flicker-free illumination and at times an additional lighting source. Here, a Phantom MIRO M-310 high-speed camera that has a maximum fps of 10000 fps is used to record the granular surface and the robot appendage. To illuminate the particles, a pair of NILA Zaila lights are used with 20° diffusing lenses. The light sources are placed above the test bed, to illuminate the particles indirectly, which creates a more even lighting. At maximum illumination (8610 lux at 1m), the light source is flicker-free, which makes it suitable for high-speed recording.

With this experimental setup, different types of robot appendages can be attached to the test bed and allowed to interact with the photoelastic granular media inside the test bed. Different robot locomotion modes include walking, jumping,

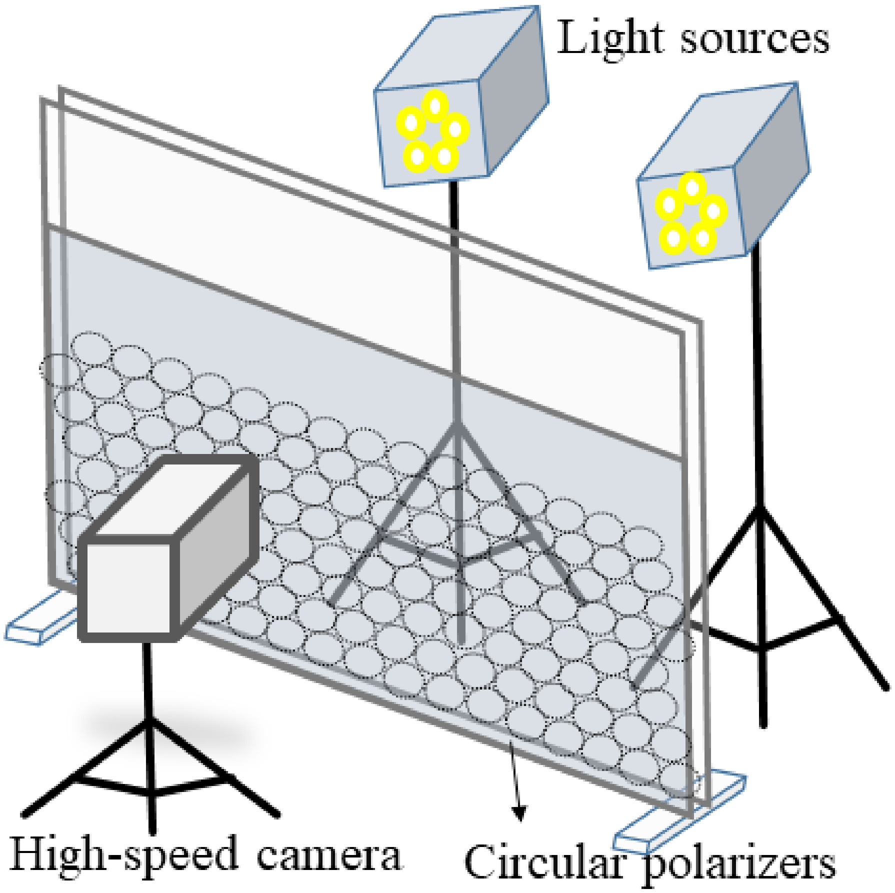

Figure 4.2: A sketch of the photoelastic granular media test bed: Circular polarizers are used to obtain a clear fringe pattern from the particles under loading. The light sources placed above the test bed illuminates the particles and a high-speed camera is employed to capture the particle motion and force-chains inside the granular media.

hopping, crawling and so on. In this experimental work, a lugged wheel and a single actuator pendulum are used for generating different gaits for robots. For example, the pendulum is used for generating a section of the gaits which is representative of swinging motion of robot legs. Similarly, lugged wheels are one of the commonly used appendages for autonomous robots for traveling on granular surfaces. Although locomotion of earthworms in photoelastic gelatin spheres has been studied by Mirbagheri et al. [2015], in order to understand the slithering motion in granular materials, legged locomotion on photoelastic materials has not been considered before. In the following sections, experimental studies and comparison with DEM studies for lugged wheel locomotion and pendulum motion on granular media are presented.

4.2 Lugged wheel locomotion on photo-elastic granular media

The experimental arrangement of the test bed and the lugged wheel is shown in Figure 4.3. The lugged wheel used in the experiments is made out of aluminum and has an inner diameter of 228mm. The wheel has 18 lugs and each of the lugs has a length of 25 mm. To rotate the wheel, a 100-Watt Maxon EC22 (386675) motor with hall sensors is used. The motor is equipped with a gear head with 128:1 reduction. The wheel is continuously driven by the motor at a constant angular speed. As the wheel rotates, it also gains translational velocity due to interaction with the granular particles. So, the wheel is allowed to freely move along the horizontal direction, but it is restricted from moving in vertical direction apart from the initial static sinkage. To facilitate this longitudinal motion, a rail mechanism including a cart and a pair of rails is designed and the wheel is attached to a cart that can move freely on top of the test bed. The arrangement of the cart and the wheel can be seen in the top perspective images of the arrangement shown in Figure 4.4. The rails are attached to the acrylic panels of the test bed and the cart is attached to the rails such that it can freely move along the rails. The wheel is positioned inside the rectangular opening that is parallel to the opening between the acrylic panels. The motor that

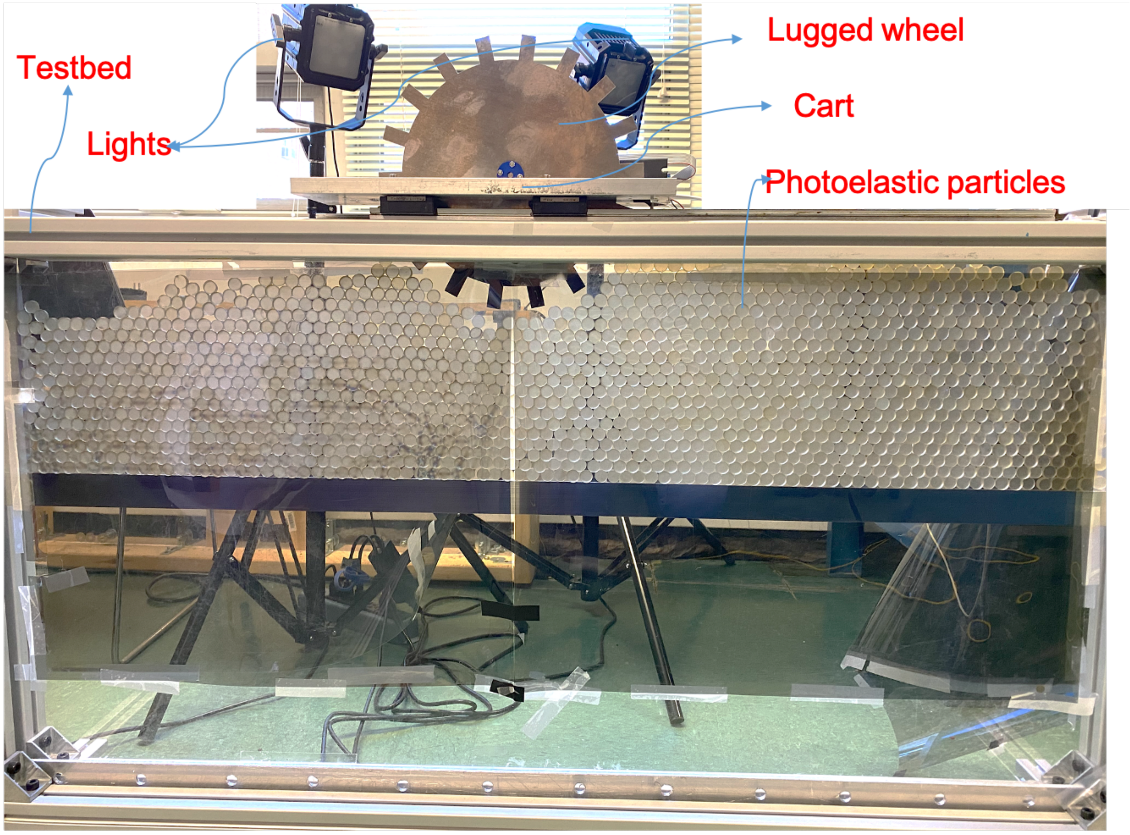

Figure 4.3: The experimental arrangement for the lugged wheel consists of a cart attached to the test bed.

is attached to the center of the wheel is fixed to the cart on one side and the cart carrying the wheel moves along the rails as the wheel gains translational velocity.

A part of the test bed is filled with the photoelastic rubber particles initially in a hexagonal packing. To mimic static sinkage of the wheel in real-world scenarios, the wheel is allowed to sink to a certain depth. The depth of sinking and the configuration of particles surrounding the wheel may have an influence on the evolution of force chains and the wheel motion. As such, multiple sets of experiments are carried out and an average behavior is gathered and presented here. In Figure 4.5, the author shows a snapshot of the configuration of the granular media and the wheel after sinking. It can be seen that the force chains are concentrated in the

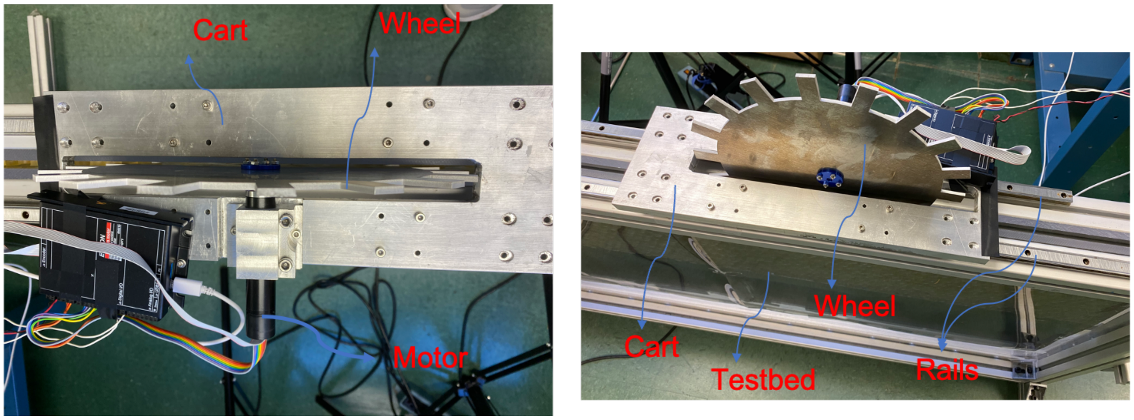

(a) (b)

Figure 4.4: Images a) and b) of the experimental arrangement with the lugged wheel taken from two different perspectives. The motor is attached to the cart on one side. The cart is attached to the two parallel rails that are fixed to the acrylic panels.

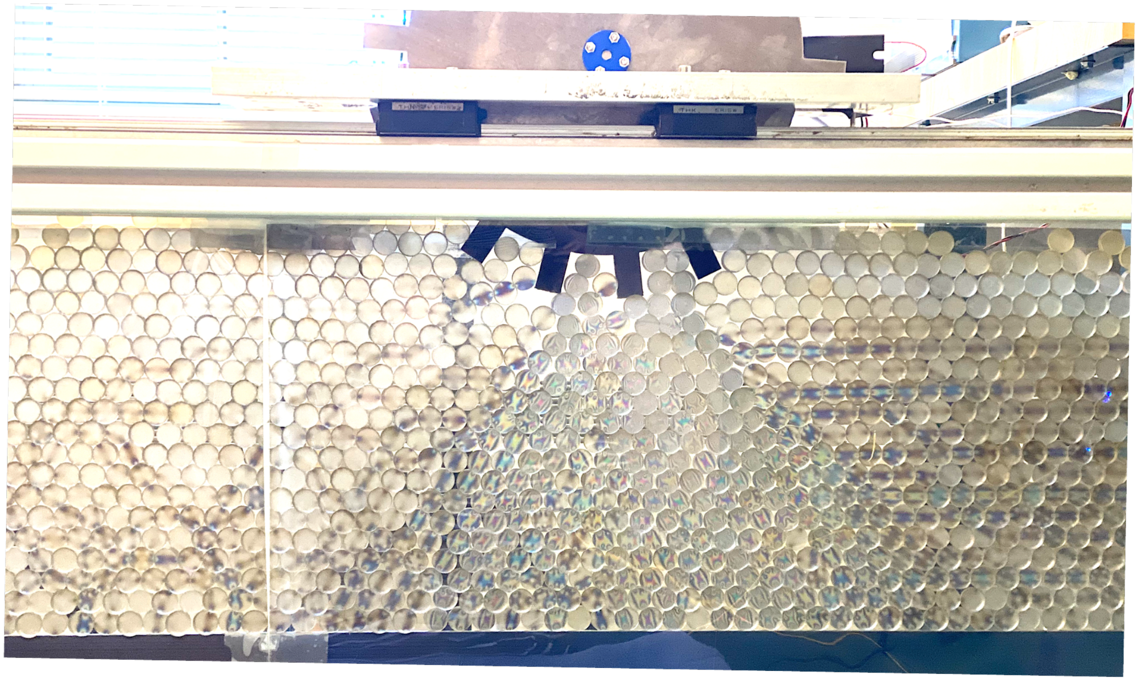

Figure 4.5: Zoom-in snapshot from the experiment with lugged wheel. Force chains generated in the granular media due to interaction with the wheel are concentrated in the portion of granular media that is directly under the wheel.

portion of granular media that is directly under the wheel. Additionally, there are also force chains that are travelling in horizontal direction towards the side walls of the wheel.

4.2.1 Results: Force chains in granular media during wheel locomotion

For a number of motor speeds ranging between 500 - 2000 rpm (0.409 - 2.454 rad/s, after the reduction), interactions between the wheel and the granular surface are recorded by using the camera setup. For each of the wheel speeds, the experiments are repeated multiple times. For a wheel speed of 500rpm, snapshots of force chains captured inside the granular media at time steps, 0s, 1s, 2s, 3s, 4s are shown in Figure 4.6. The experiment with the same angular velocity of 0.409 rad/s is repeated and the zoom-in snapshots from the experiment are shown in Figure 4.7. For a wheel speed of 1000rpm, snapshots of force chains captured inside the granular media are shown in Figures 4.8 and 4.9.

From Figures 4.6, 4.7, 4.8 and 4.9, it can be observed that the force networks are concentrated in the portion of media directly under the wheel. The force chains reach all the way to the bottom wall and reflect therefrom. This behavior of force chains is observed in the repetitions of the experiment. Also, a cone like region with an approximate angle of 45 degrees is formed with the force networks. In addition to the force chains under the wheel, horizontal force chains emerge from the boundaries of the cone. As the wheel travels on the granular media, the cone formed from the force chains also travels in the forward direction as shown in Figure 4.10. This behavior qualitatively agrees with the numerical findings on force distribution in granular media, investigated using DEM.

The wheel is driven at $\omega = 0.409$ rad/s and the actual speed of the motor is recorded during the experiments in order to make sure that the constant speed assumption is valid. As shown in Figure 4.11, the motor speed is approximately equal to the target value with an average variation of 1.2%. The reaction forces on the wheel due to contact with the particles of the granular media varies as the wheel travels. So, to counter these reaction forces from the particles and maintain a constant angular speed for the wheel, a variable torque is applied on the wheel. The motor current values that are indicative of the torque applied on the wheel are recorded in addition to the motor speed values. In Figure 4.12, motor current recorded for experiments with an angular speed of 0.409 rad/s is shown.

Based on the wheel angular speed and the configuration of the particles, the amount of traction and horizontal speed gained by the wheel may vary. For the wheel rotating with 0.409 rad/s and the initial configuration of particles as shown in Figure 4.6, the position of wheel is tracked to determine the velocity. In Figure 4.13, the author shows the horizontal velocity of the wheel. For a different wheel angular speed of 0.818 rad/s, the experiments are repeated and the relevant values are recorded. In figure 4.14, time series plots for the motor current values recorded for two runs and the averaged values is shown.

4.2.2 Conclusions

In these studies, dynamic interactions between a lugged wheel and photoelastic granular media have been experimentally investigated. Experiments involved high-speed video imaging of translucent photoelastic particles under polarized light for visualizing evolution of force chains through fringe patterns. The force chains are generated in the granular media due to both static load from the weight of the wheel and dynamic interactions as the wheel travels along the granular surface. The force chains generated inside the granular media form a cone and the cone travels along with the wheel. Moreover, the torque required to rotate the wheel at a constant angular speed varies non-linearly with time and no dominant frequency is observed. Similar behavior is also observed for the horizontal velocity gained by the wheel.

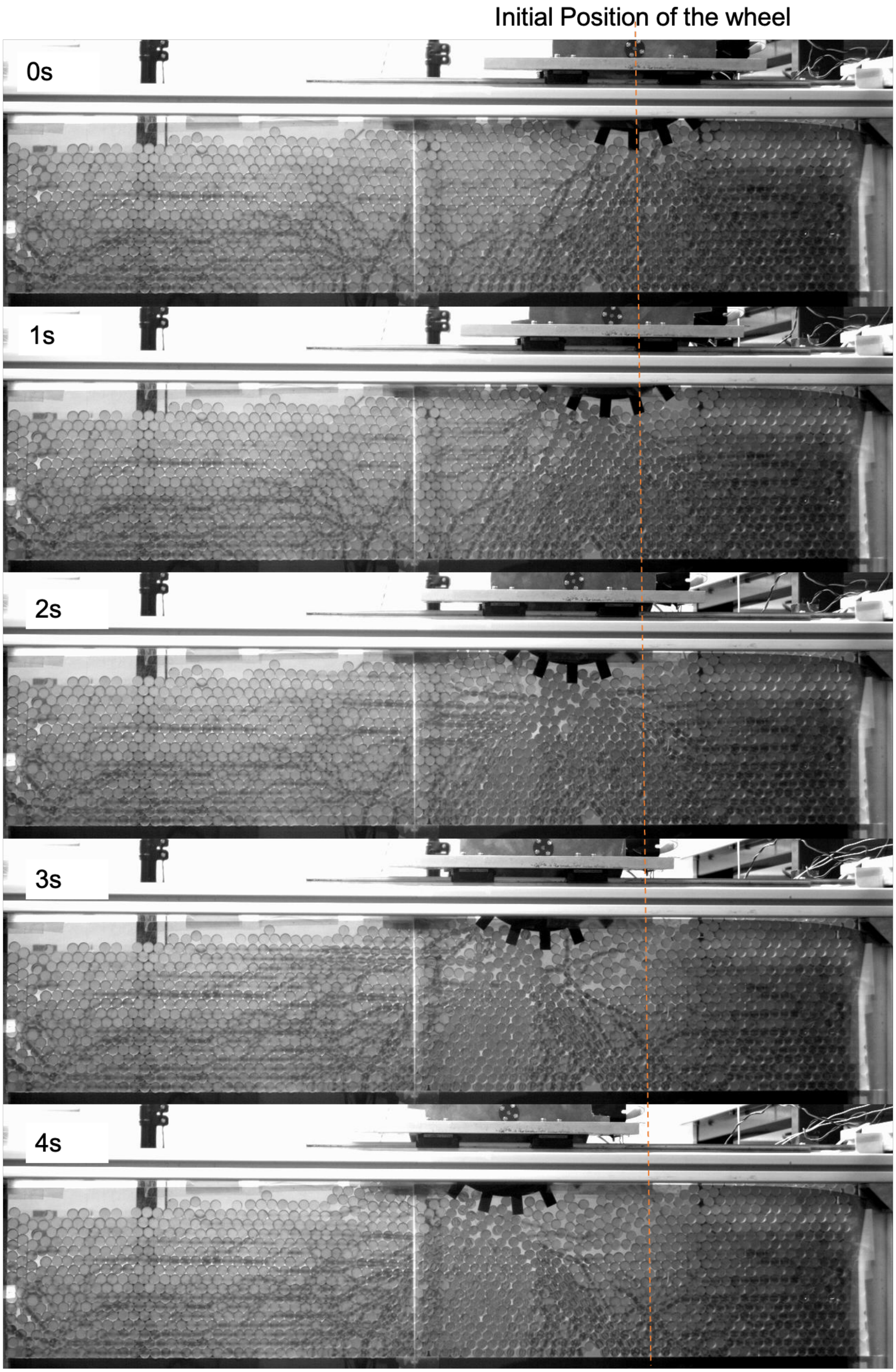

Figure 4.6: Snapshots from the experiment with lugged wheel rotating at $\omega = 0.409$ rad/s, captured at regular intervals of 1 sec.

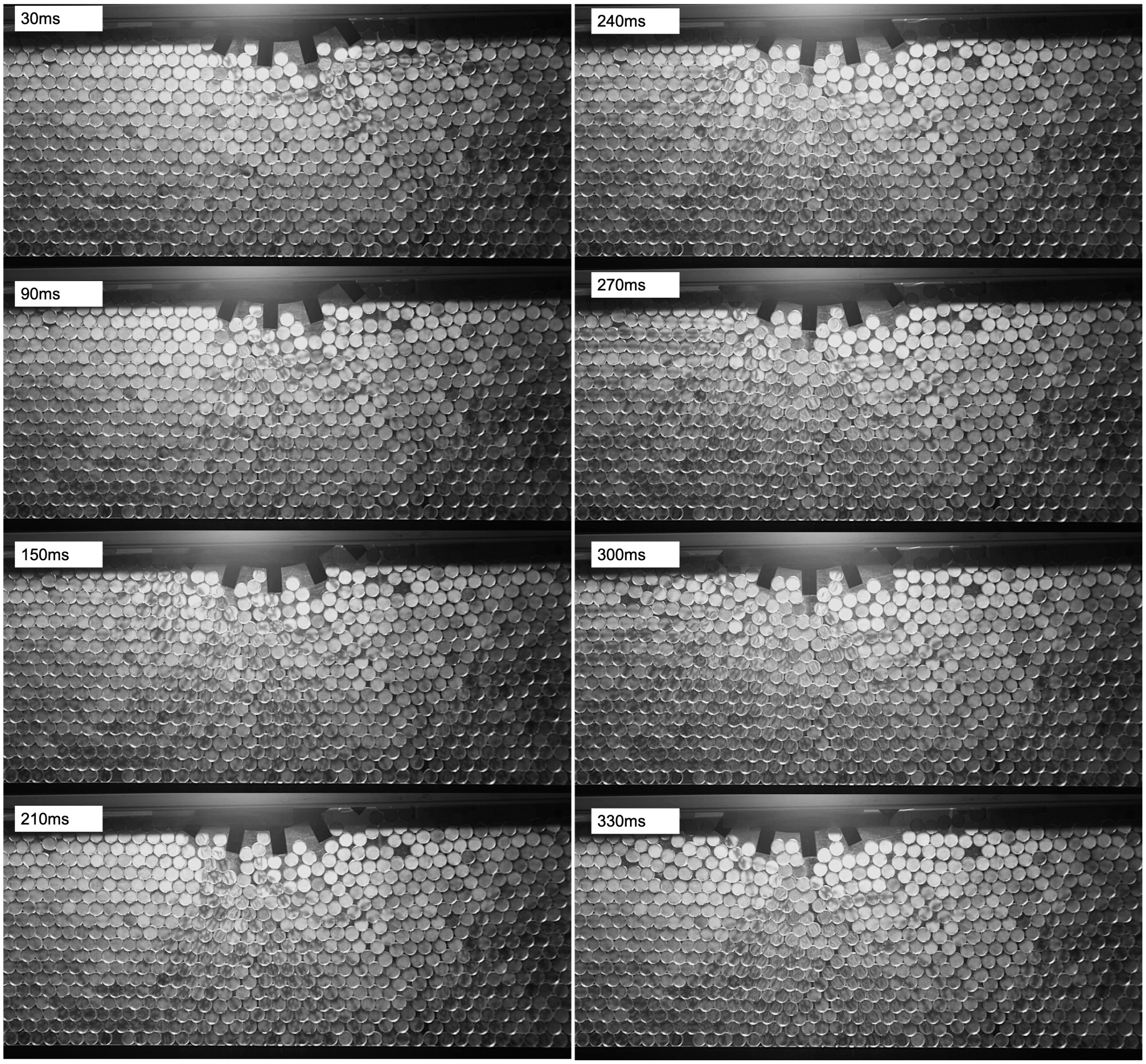

Figure 4.7: Zoom-in snapshots from the experiment with lugged wheel rotating at $\omega = 0.409$ rad/s, captured at regular intervals of 30 ms.

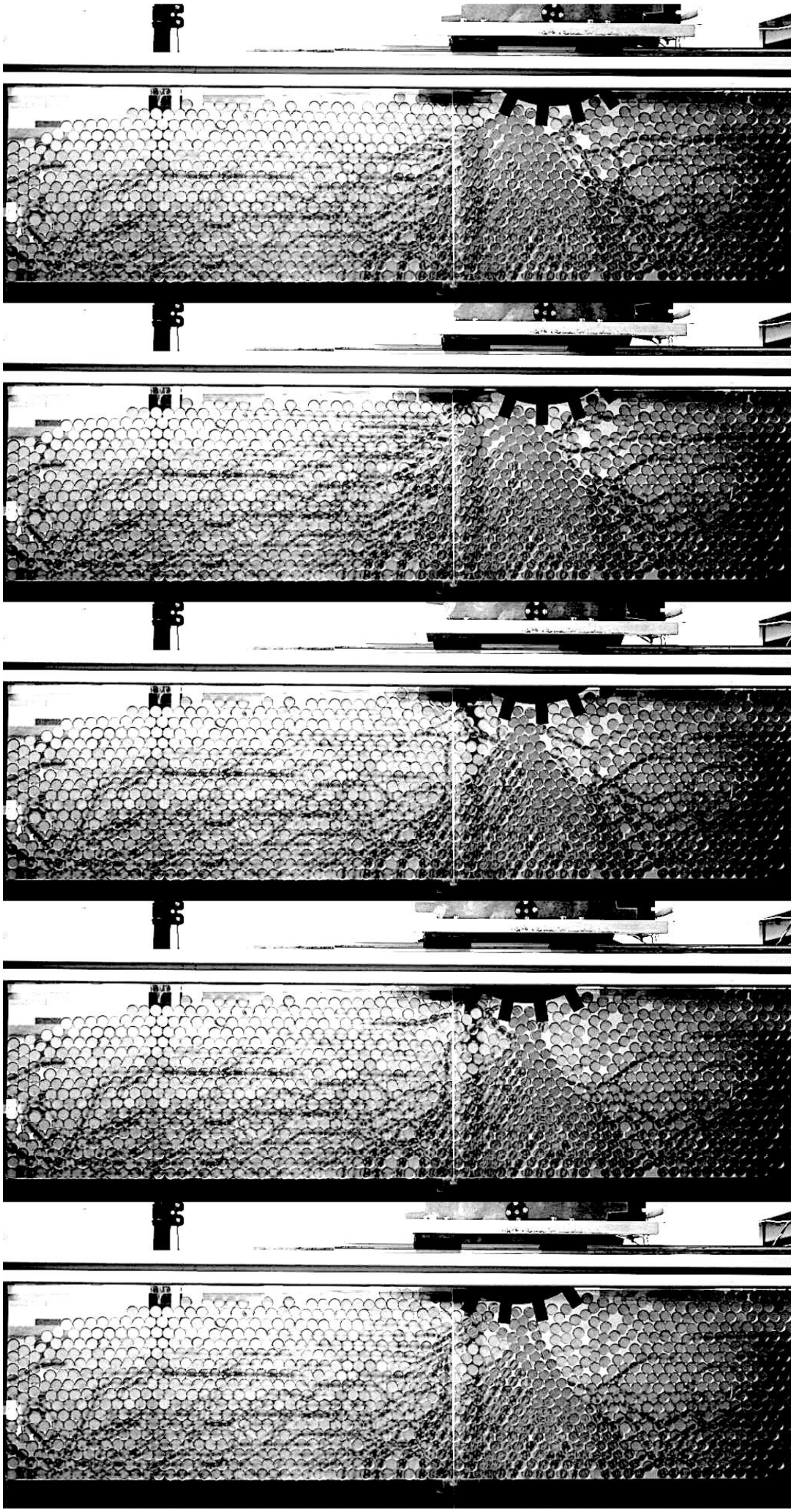

Figure 4.8: Snapshots from the experiment with lugged wheel rotating at $\omega = 0.818$ rad/s, captured at t = 1.1 sec, 1.2 sec, 1.3 sec, 1.4 sec, and 1.5 sec.

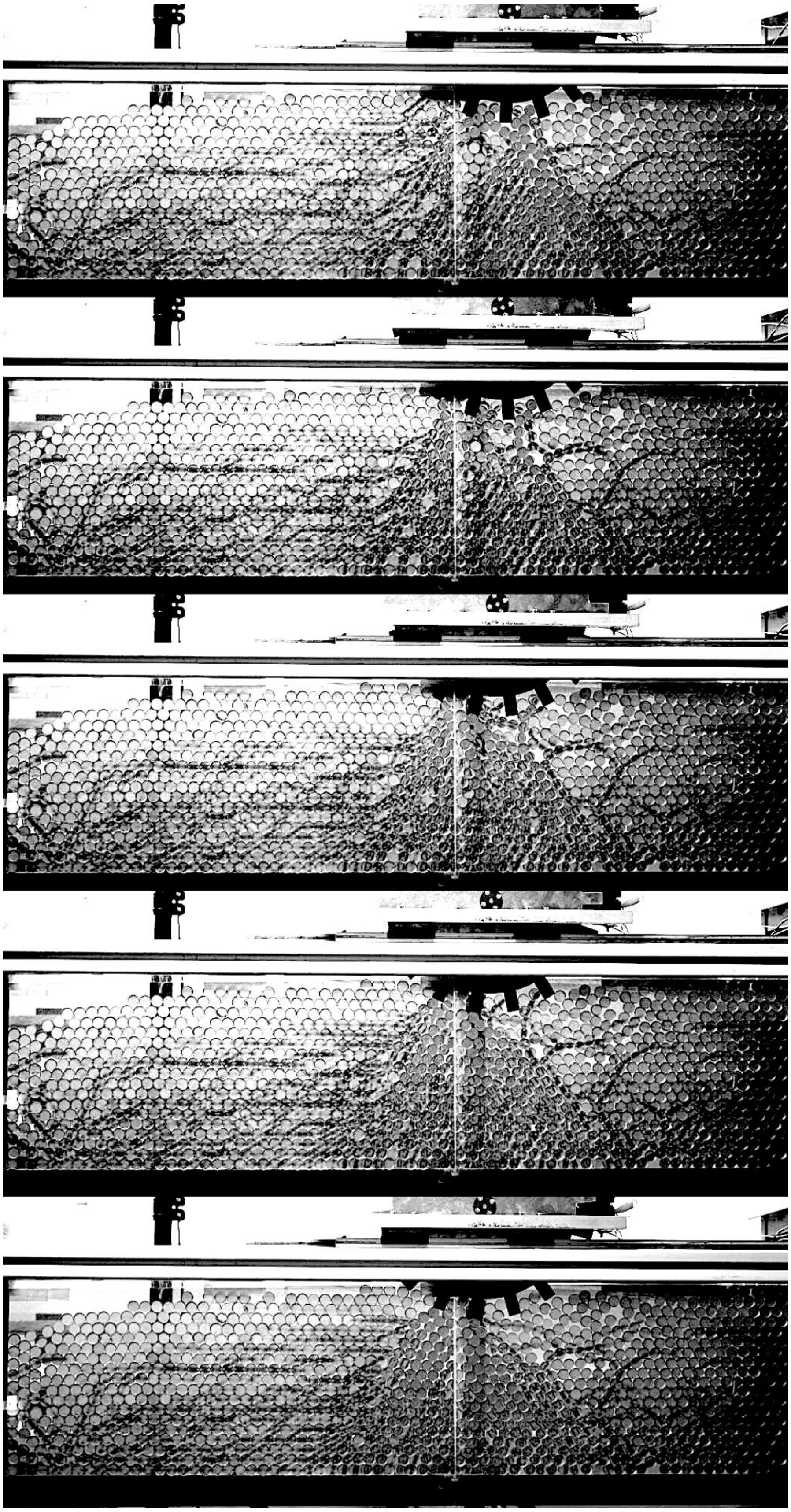

Figure 4.9: Snapshots from the experiment with lugged wheel rotating at $\omega = 0.818$ rad/s, captured at t = 1.6 sec, 1.7 sec, 1.8 sec, 1.9 sec, and 2 sec.

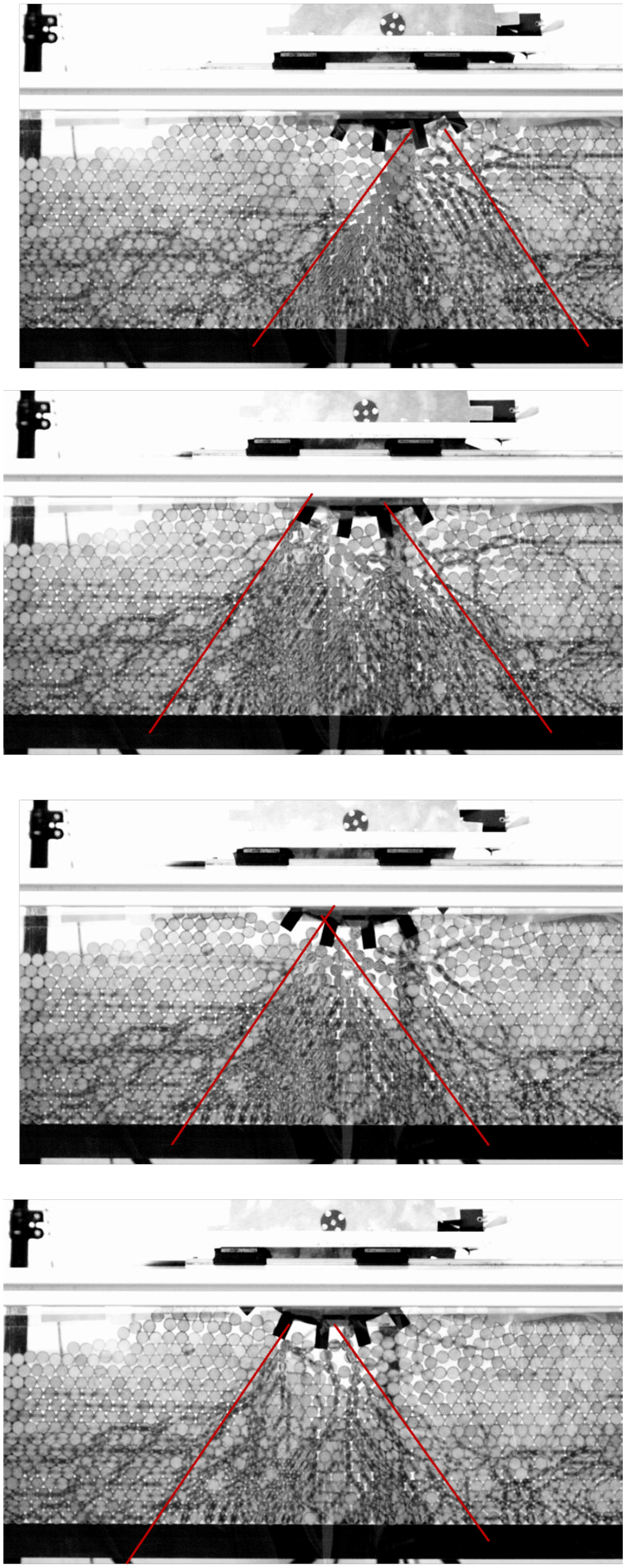

Figure 4.10: Snapshots from the experiment with lugged wheel rotating at $\omega = 0.818$ rad/s, captured at regular intervals of 0.1 sec.

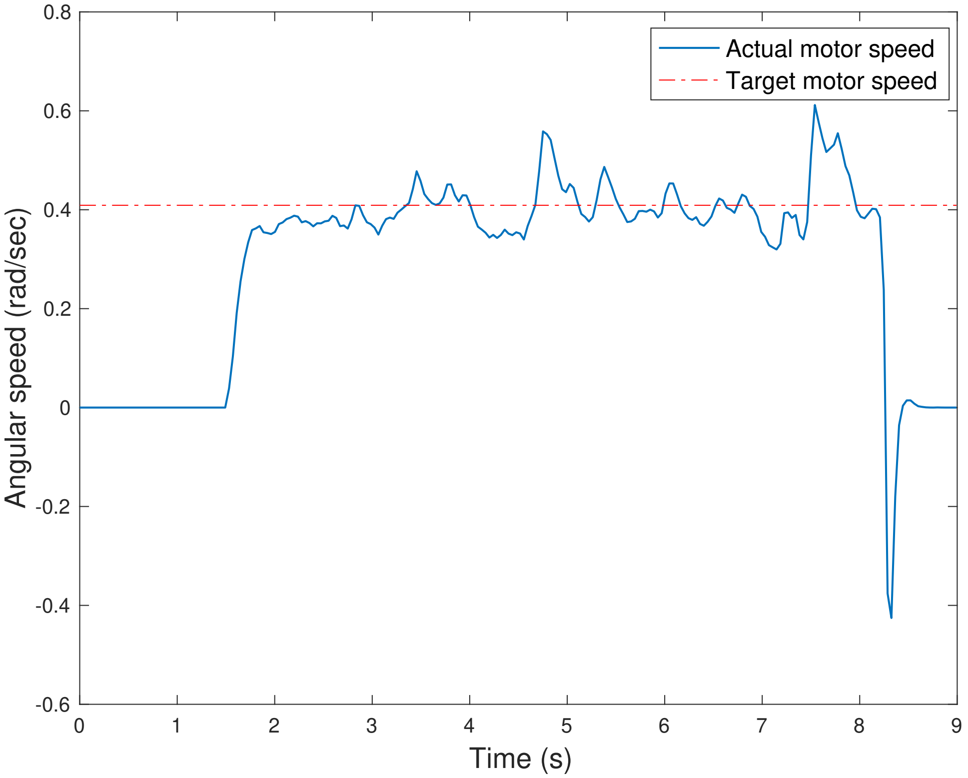

Figure 4.11: Angular speed of the motor recorded during experiments with lugged wheel. After the wheel starts rotating, the measured angular speed of the motor is close to the target value of 0.409 rad/s shown as dashed line with an averaged variation of 1.2%.

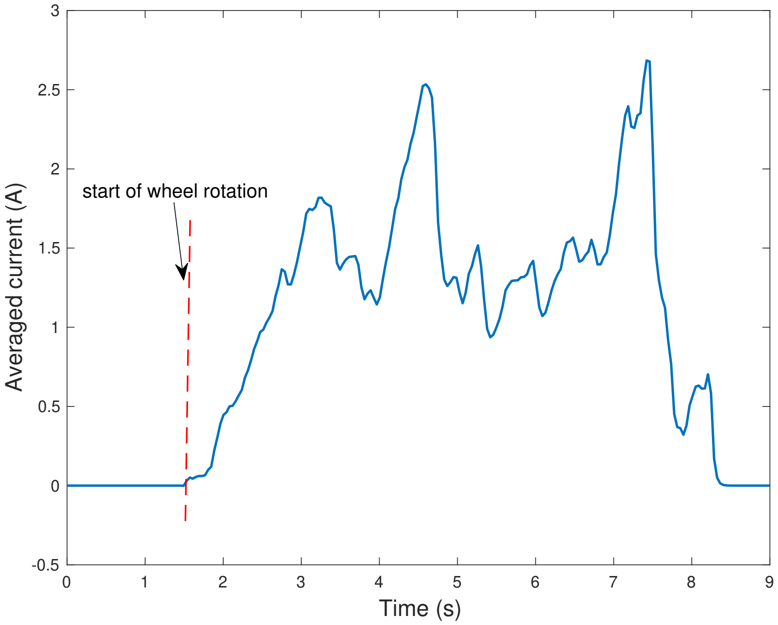

Figure 4.12: Motor current values recorded during experiments with lugged wheel rotating at an angular speed of 0.409 rad/s. The current values are a measure of the torque applied on the wheel to rotate at a constant angular speed.

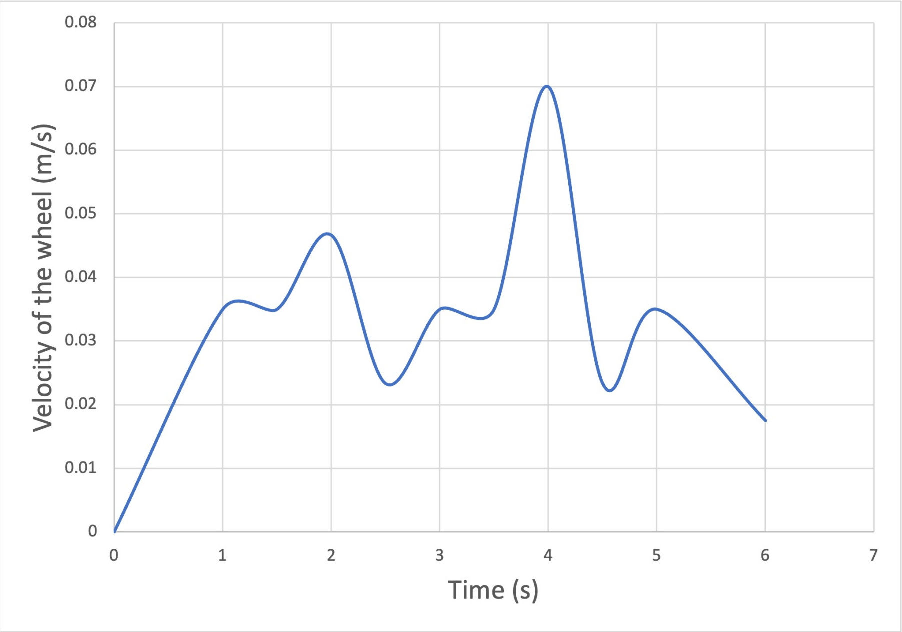

Figure 4.13: Horizontal velocity determined for the wheel when rotated at an angular speed of 0.409 rad/s. Position of the wheel is tracked in time from the recorded video data to determine the velocity.

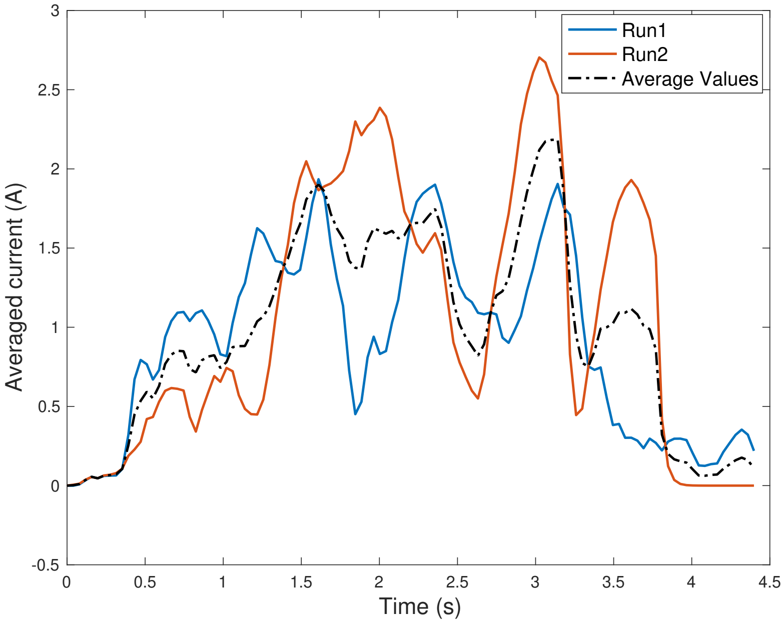

Figure 4.14: Motor current values recorded during experiments with lugged wheel rotating at an angular speed of 0.818 rad/s. The current values are recorded for multiple runs and interpolated to determine the average values shown as the dashed line.

4.3 Pendulum interactions with Granular Media

In this section, experimental investigations using a single actuator pendulum are presented. The pendulum configuration is essentially similar to a single actuator robot leg that is used in the literature for locomotion on granular surfaces, see Li et al. [2013] and Saranli et al. [2001]. Particle displacements as well as force chains in 2D are investigated during interactions with the rotating pendulum. The pendulum is made out of aluminum and has the dimensions 160 mm × 15 mm × 3 mm and is driven by a 100-Watt Maxon EC22 (386675) motor. Here, the pendulum only has rotational motion unlike the wheel that has both translational and rotational motions. Accordingly, the motor that is attached to the pendulum is directly attached to the test bed instead of the cart. A part of the test bed is filled with 520 (40×13) particles with photoelastic particles in a hexagonal packing, as shown in Figure 4.15. The vertical distance between the motor shaft and the granular surface is 132 mm. Therefore the maximum depth the pendulum can reach (i.e. when the pendulum is vertical) is 28 mm (i.e., two-particles deep).

For a number of motor speeds between 500 - 3000 rpm (0.409 - 2.454 rad/s, after the reduction), interactions between the pendulum and the granular surface are recorded with a pair of Phantom MIRO M-310 high-speed cameras. At full resolution (1280 × 800), the videos are recorded at 1000 fps. The pendulum is driven at $\omega = 0.409$, 0.818, 1.636, and 2.454 rad/s. The actual speed of the motor is recorded and the encoder position is tracked during the experiments in order to detect the moment of impact. In Figure 4.16, the angular speed and encoder

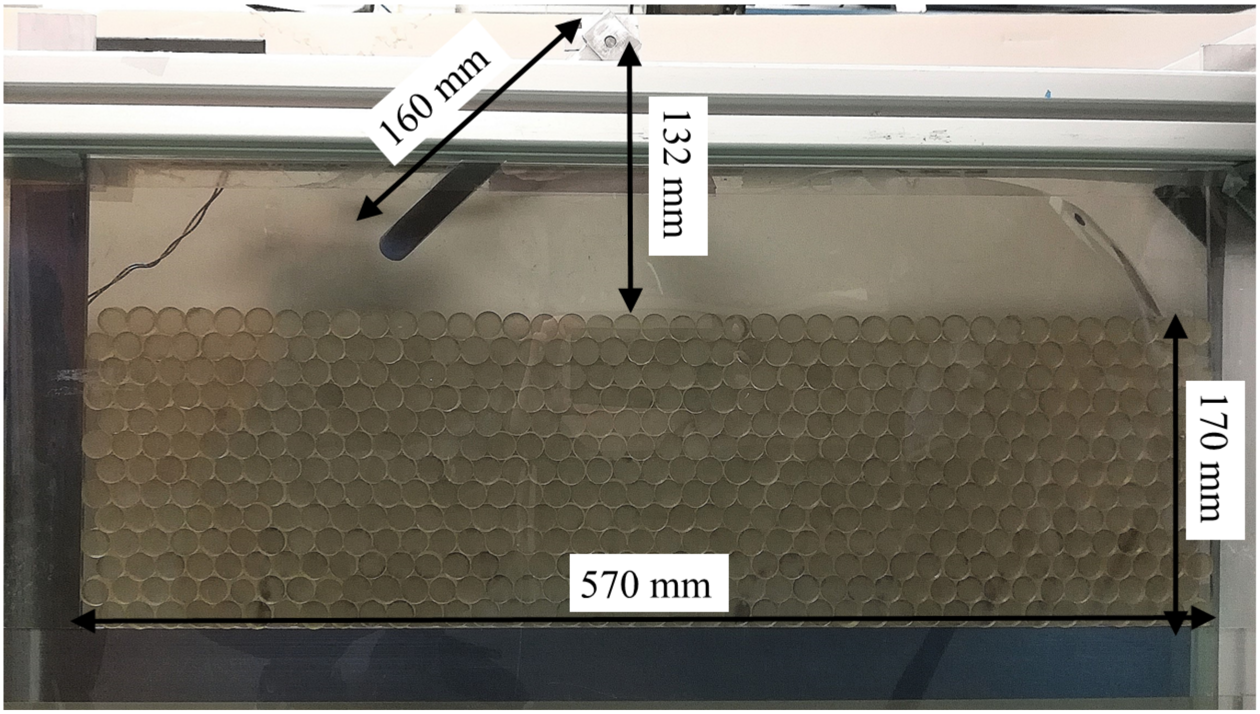

Figure 4.15: Dimensions for experimental arrangement.

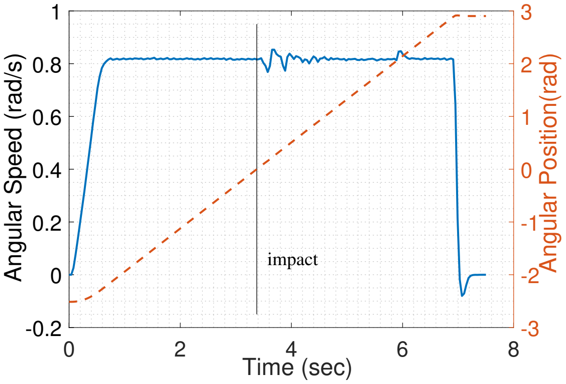

Figure 4.16: Angular speed and position data of the motor during pendulum impact experiment at $\omega = 0.818$ rad/s. The angular position is measured from the impact point.

position data recorded for $\omega = 0.818$ rad/s are shown. For larger motor speeds, the speed does not change more than 6 % whereas for the lowest angular speed tested (0.409 rad/s), the variation is around 14%.

4.3.1 Results: Force chains in granular media during pendulum locomotion

Force chain propagation data in the frames are extracted from the high-speed videos. To analyze the granular motion and force chains, PEGS tool, which was developed by Daniels et al. [2017], is adapted in this study. PEGS is a tool to find the particle locations, their contact points and force chains in the granular media, through the MATLAB's image processing tool.

In order to visualize how the force chains evolve, a snapshot of the pendulum-granular surface interactions are taken at every 100 ms starting at t = 50 ms after the pendulum impact at $\omega = 0.818$ rad/s, as shown in Figures 4.17 and 4.18. At t = 50 ms, the force network starts from the particle that is in immediate contact with the pendulum, and it branches into two diagonal directions. Then, after 100ms, the particles in the top row get compressed due to horizontal pressure applied by the pendulum, and start moving upwards as shown in t=250ms. Then, as the pendulum keeps moving, it impacts on the granules again. It presses on top rows in the horizontal direction (see t=450ms), and creates large stresses, forcing the granules to flow upwards, and gain speed in the vertical direction (see t=550ms and t=650ms). The horizontal force chains become more prominent as the pendulum gets deeper inside the media, and the line of contact becomes more vertical. Through the complete rotation of pendulum inside the granular media, the same pattern of horizontal pressure due to pendulum impact leading to vertical motion of the top rows is seen four times. The trend is similar for other studied pendulum speeds (ω

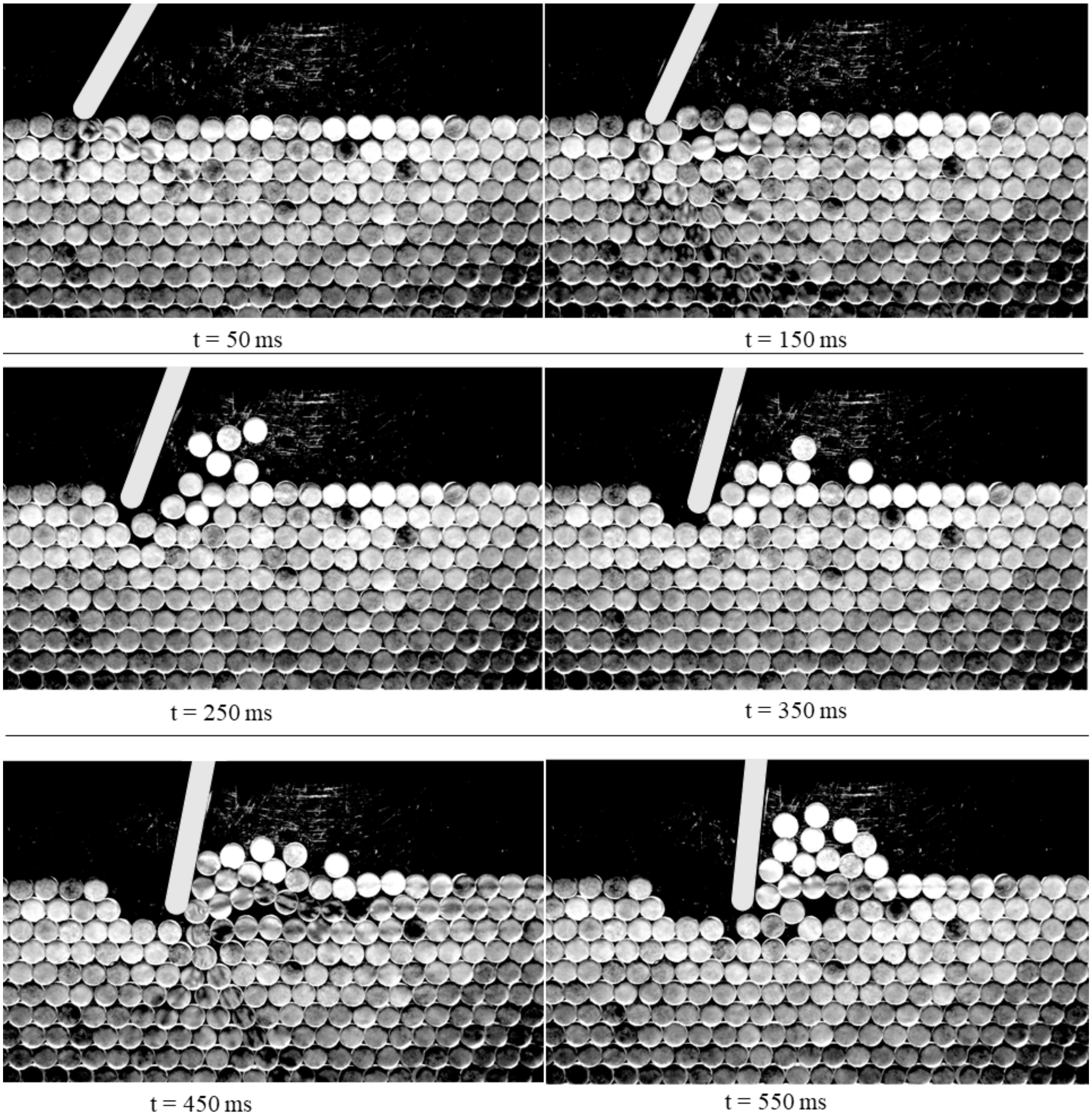
t = 50 ms

t = 150 ms

t = 250 ms

t = 350 ms

t = 450 ms

t = 550 ms

Figure 4.17: Zoom-in snapshots from the experiment with $\omega = 0.818$ rad/s, showing the force chain evolution inside the photoelastic granular media.

$= 0.409$, 1.636, and 2.454rad/s).

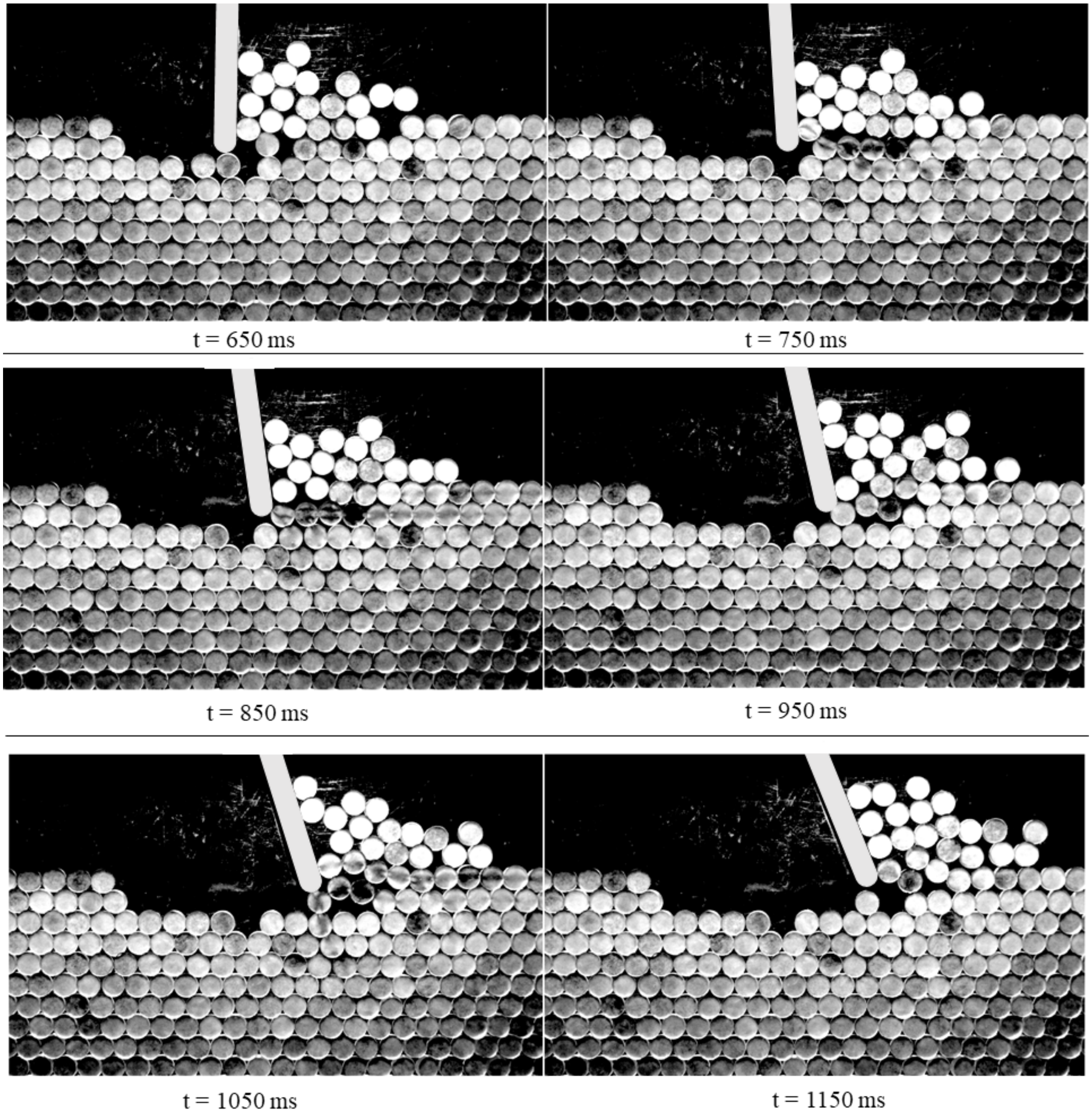

t = 650 ms

t = 750 ms

t = 850 ms

t = 950 ms

t = 1050 ms

t = 1150 ms

Figure 4.18: Zoom-in snapshots from the experiment with $\omega = 0.818$ rad/s, showing the force chain evolution inside the photoelastic granular media.

From the evolution of force chains, one can see how the locations of high stresses develop, and the pendulum motion induces the media's transition from solid phase to the fluid phase. From the high force chains, one can see the weak points of the granular media, where the internal stresses exceed the shear strength, and the material cannot support the weight and the dynamic forces of the robot leg (pendulum) anymore.

In Figure 4.19, a comparison of the motor torque for wheel angular speeds of 0.818 rad/s, 1.636 rad/s, and 2.454 rad/s is shown. It can be seen that for each of the angular speeds, the pendulum has a maximum torque at the moment of impact and it decays as the pendulum rotates inside the granular media. Further, with increase in angular speed, the number of peaks in motor torques also decreases and a smooth decay can be observed. For angular speed of 0.818 rad/s, the average torque applied before the impact is τ_0=0.85 mNm, which is a measure of the torque spent to rotate the pendulum at a constant speed (to overcome the damping effects). During the first impact, the maxi-mum torque applied by the motor is τ_{max}=7.18 mNm, and the variation from the nominal torque applied before the impact is 6.33 mNm. Transmitting this torque through the gearbox, which has a reduction ratio r_{gear}=1/128, and the maximum efficiency (η) 59 %, the effective torque applied on the pendulum is given by

$$\tau_p = \eta(\tau_{max} - \tau_0)/r_{gear} = 0.48Nm. \tag{4.1}$$

The force applied on the particles in the perpendicular direction can be es-

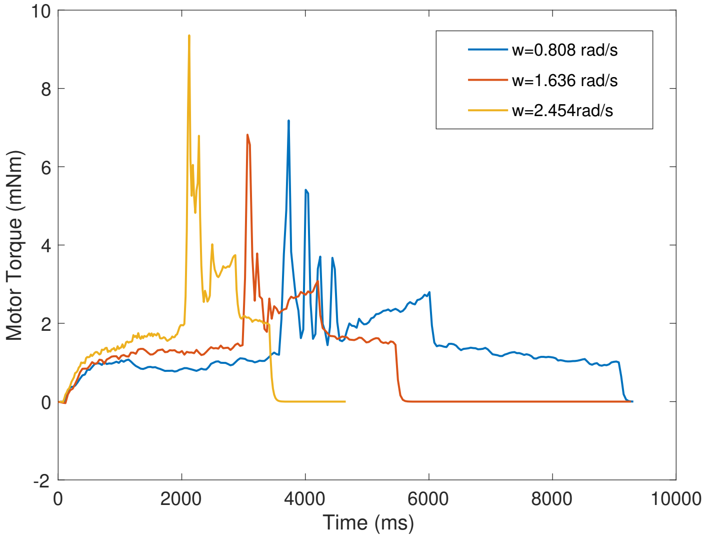

Figure 4.19: Torque data of the motor during interactions with the granular surface for different angular speeds of $\omega = 0.818$ rad/s, 1.636 rad/s, and 2.454 rad/s.

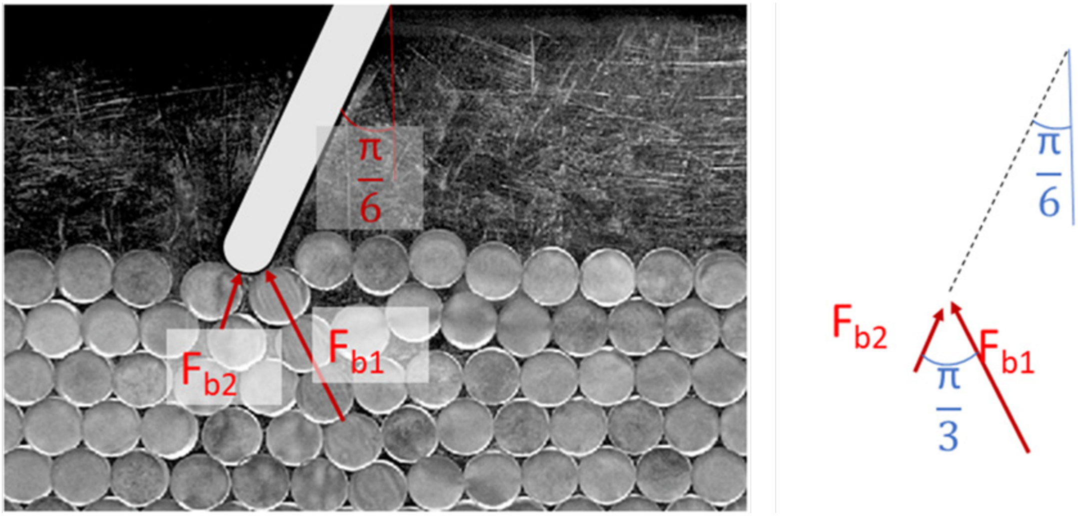

Figure 4.20: Reaction forces on the pendulum after impact with the granular media.

timated as $F_p = 3$N based on the length of the pendulum (L_p =0.16m) and the effective torque applied on the pendulum. The torque applied by the pendulum peaks around 150 ms after the impact. In Figure 4.17, one can see that only two particles are in immediate contact with the pendulum at t=150ms, where F_{b2} is

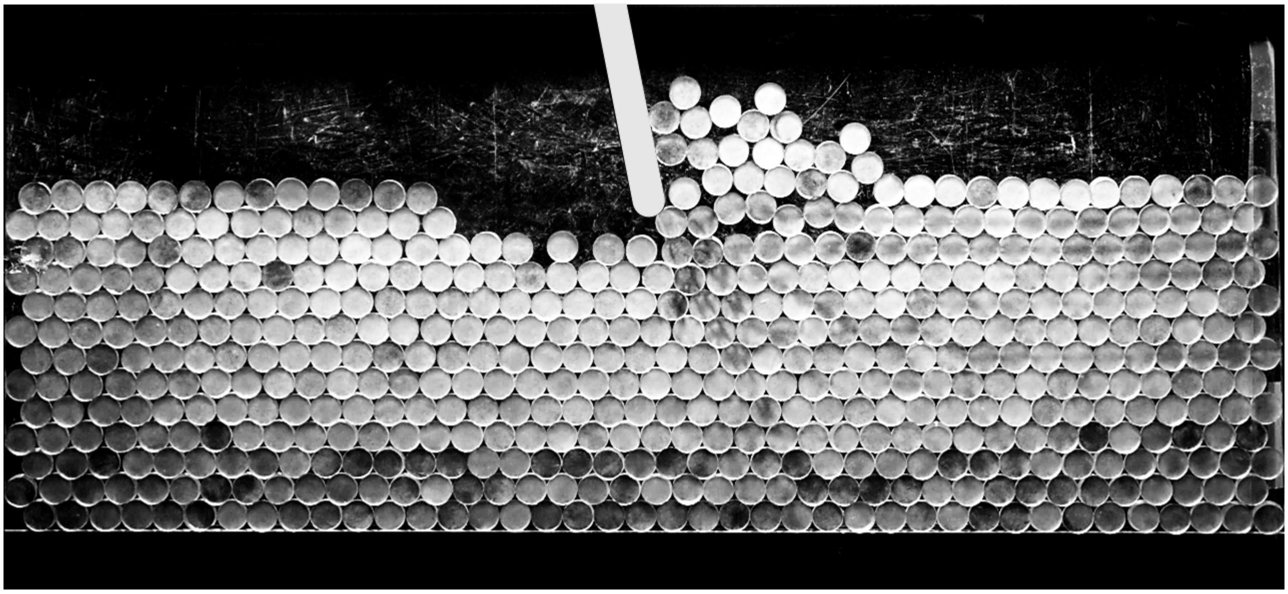

Figure 4.21: A snapshot at t=810s from the experiment for ω =0.818rad/s, showing the force chains extending up to the boundaries.

almost co-linear with the pendulum. Therefore the only reaction force that has a perpendicular component is F_{b1}. From Figure 4.17, one can see that 150 ms after the impact, the angle between the pendulum and the vertical is around $\pi/6$, as shown in Figure 4.20. Since the particles are in hexagonal packing, and the particle bearing the force F_{b1} is under diametric loading, the force chain along F_{b1} direction makes a $\pi/3$ angle with the pendulum. Therefore, assuming that the speed of the pendulum is constant, the perpendicular component of F_{b1} is $||F_p|| = ||F_{b1}||sin(\pi/3) = 3N$, which implies that at the instant the highest torque is applied by the pendulum, the highest force bearing particle is under $||F_{b1}|| = 3.46N$ compression.

The packing type affects both the magnitude and direction of the forces traveling inside the granular media. Since the force chains inside the photoelastic media are compression forces that are primarily aligned with the contact points between the particles, directions of the force chains depend on the angle between the lines connecting the particle contact points. In a hexagonal arrangement, the angle between the lines connecting the contact points is 60°, the angle between forces is also predominantly 60°, although there are some irregularities. For other types of packing, the force directions would be different (e.g., 90° for square packing).

The force chains are found to move horizontally all the way to the right wall on top two rows as shown Figure 4.21, and the diagonal force chains move all the way to the bottom wall when the pendulum is in contact with the particles, as can be seen in frames t=150ms and t=450ms in Figure 4.18. This suggests that the force chain pattern inside the media is affected by the reflections from the walls. In a larger container, the forces would travel through longer chains, and the amount of energy dissipated due to damping and friction would be larger. This would affect the velocities of the particles and the reaction forces applied on the pendulum. Experiments with a larger portion of the test bed (i.e., larger number of particles) need to be conducted to overcome the wall effects. These studies are left for a future work.

As the pendulum applies a horizontal force on the top rows, the chain of particles deforms under compression, and at a critical point it goes through what can be considered as “buckling”. Similar to the classic column buckling, the particle chain is found to undergo plastic deformation in the lateral direction due to the compression, which results in a few particles getting released from the row and gaining speed in the vertical direction. Therefore, the potential energy stored in the deformed particles right before buckling transforms into the kinetic energy of particles that pop out of the particle chain. Since the force leading to “buckling” of the particle chain is the same for all pendulum speeds, the energy transferred to particle motion, hence, the vertical particle speed, are also independent of the pendulum speed.

4.3.2 DEM studies on pendulum interaction with granular media

Numerical studies on pendulum motion on granular media are conducted by using DEM model described previously in Chapter 2. For the DEM simulations, dimensions of test bed and pendulum that are same as the one used in experiments are used. However, the granular media with a different resolution is considered for DEM simulations, specifically the particles are considered to have half the radius of the particles used for experiments. Accordingly, the properties of DEM elements are calculated based on the material properties of the photo-elastic rubber particles. While material characterization to determine mechanical and DEM properties of the particles after machining is outside the scope of this dissertation, it could be a potential avenue for future work.

DEM simulations were carried out for a range of angular speeds and fixed size and configuration of the pendulum and granular media. In Figure 4.22, the time series plots for the driving torque of the pendulum are shown for angular speeds of $\omega = 8$ rad/s, 10 rad/s, and 15 rad/s. The torque on the pendulum is highest at the moment of impact of the pendulum with granular media for each of the angular speeds. Further, This behavior of torque is consistent with that of

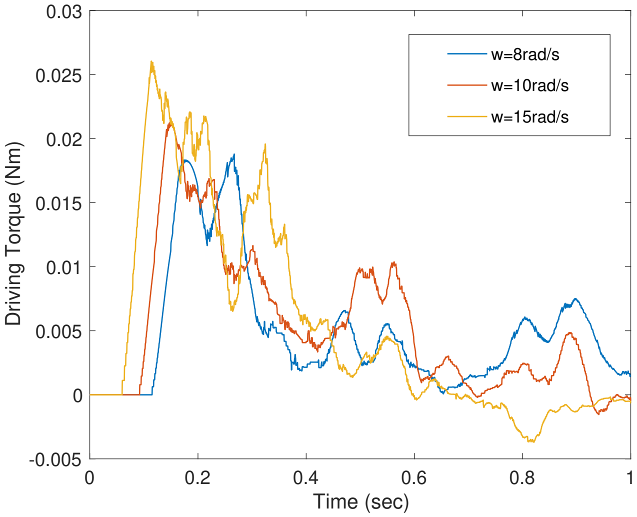

Figure 4.22: Time series plots for driving torque of pendulum at different angular speeds $\omega = 8$ rad/s, 10 rad/s, and 15 rad/s.

the torque determined from current data from experiments. In Figure 4.23, the time series plots for the number of particles with higher forces and the maximum forces in the granular media are shown for different angular speeds $\omega = 20$ rad/s, 25 rad/s, 30 rad/s, 35 rad/s, and 40 rad/s. Number of particles with higher forces is a measure of the force distribution in the granular media and it can be seen that the number is highest at the moment of impact and then decays exponentially as the pendulum further rotates. Further, the pendulum performance determined in terms of average reaction force, driving torque, and power consumption determined for different angular speeds of the pendulum are plotted in Figure 4.24.

Force distribution inside the granular media as the pendulum impacts the granular media is shown in Figure 4.25. Particles with the same color experience approximately the same magnitudes of forces. The force distribution inside the granular media can be visualized based on the colorbar shown. It can be observed

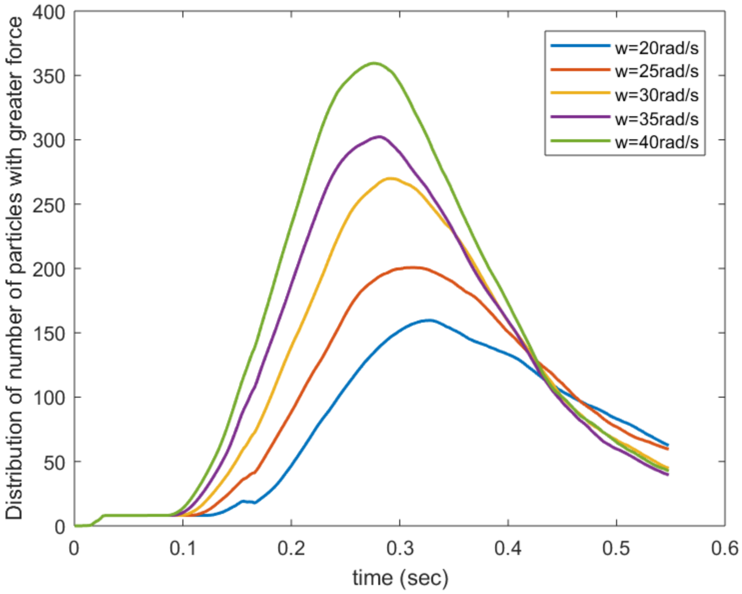

(a)

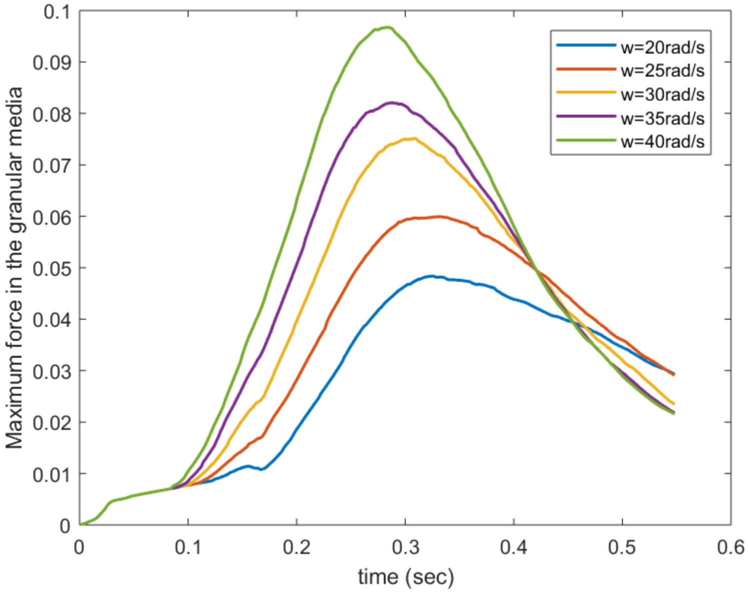

(b)

Figure 4.23: Time series plots: a) force distribution of particles and b) maximum forces in the granular media are compared for different angular speeds $\omega = 20$ rad/s, 25 rad/s, 30 rad/s, 35 rad/s, and 40 rad/s.

that, the the force chains originated at the impact point of pendulum travels deeper into the granular media in a direction that is parallel to the pendulum. While some

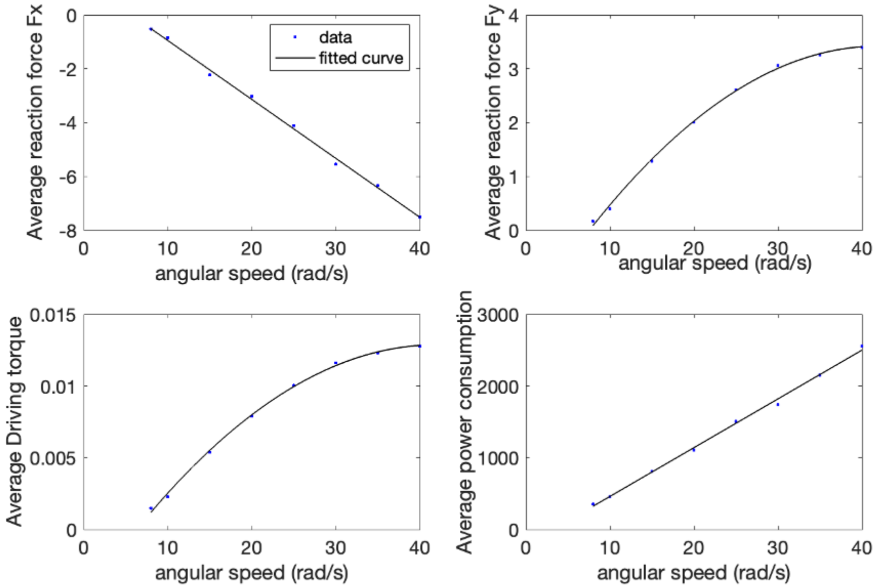

Figure 4.24: Pendulum performance for different angular speeds.

of the forces are dissipated, the rest are transmitted to the particles in contact. As the pendulum rotates further, new contacts are made and so the area of higher force concentration increases.

4.3.3 Conclusions

Dynamic interactions between a speed-driven pendulum and photoelastic granular media have been studied to explore granular media behavior during robot locomotion. For a selected rotor speed, snapshots of force chains have been presented. During penetration through the granular surface, the horizontal force chains have been observed due to speed-driven pendulum striking the granules multiple times, and causing high stresses in the top rows of particles. The maximum force acting on the particles was calculated through the motor-torque data. Furthermore, DEM simulations are conducted for pendulum interactions with granular media and

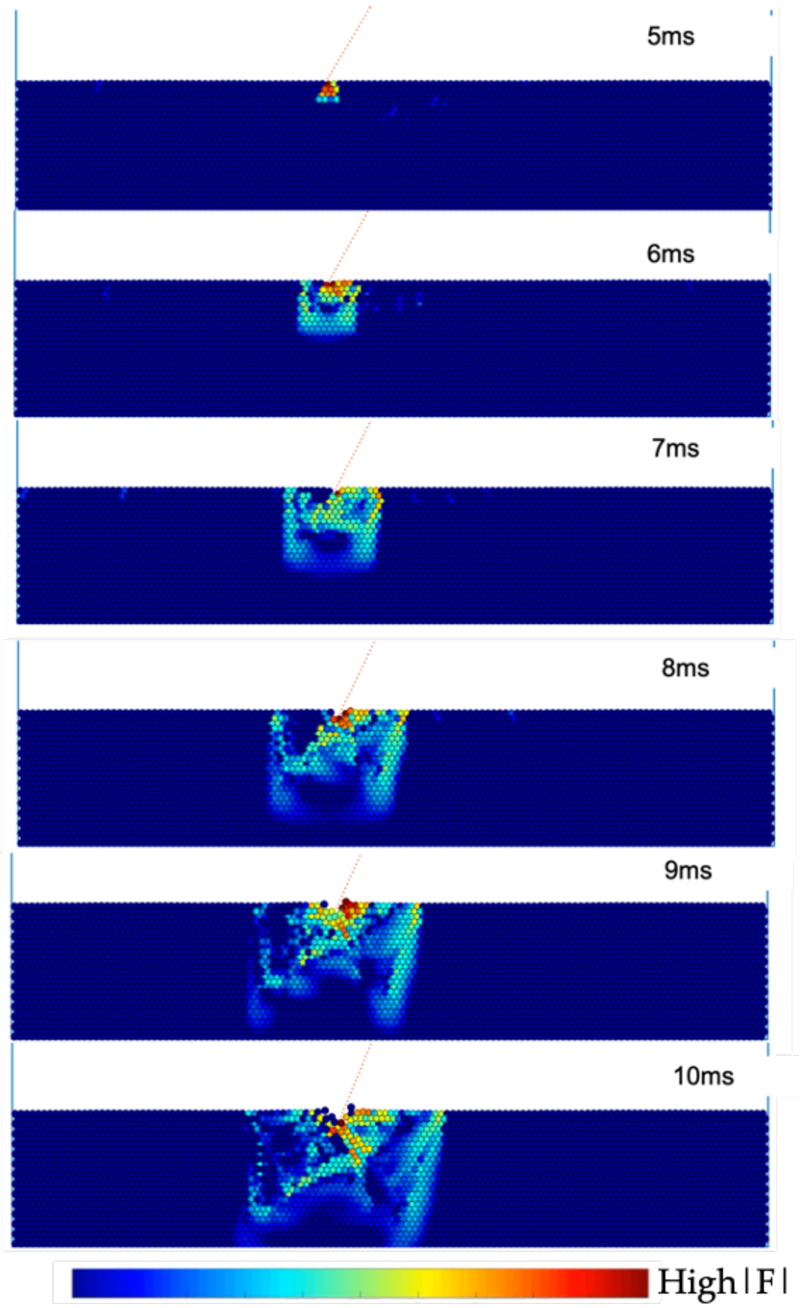

Figure 4.25: Snapshots from DEM simulations with pendulum rotating at $\omega = 30$ rad/s. These frames are captured at regular intervals of 1ms.

qualitative comparisons of torque, force distributions inside the granular media are presented.

4.4 Comparison between granular media interactions with the lugged wheel and the pendulum

For both lugged wheel and pendulum, during initial phases of interaction with granular media, force chains form a cone shape and travel angularly towards the bottom wall as shown in Figure 4.26. Further, the forces disperse/dissipate as the pendulum moves and the force network becomes sparse compared to that of the wheel. In addition to the cone, one of the significant observations that can be made from the studies is the horizontal force chains that are generated during locomotion of both the wheel and the pendulum. In Figure 4.27, the author shows the snapshots of the force chains inside the granular media captured during initial phase and after a certain time. As the wheel travels on the granular media, it can be seen that the horizontal force chains are generated in the forward path of the wheel. Similar behavior is also observed from DEM simulations as shown previously in Figures 3.3 and 3.4 in Chapter 3. The results indicate that the granular media that is away from the wheel is also affected during locomotion of the wheel.

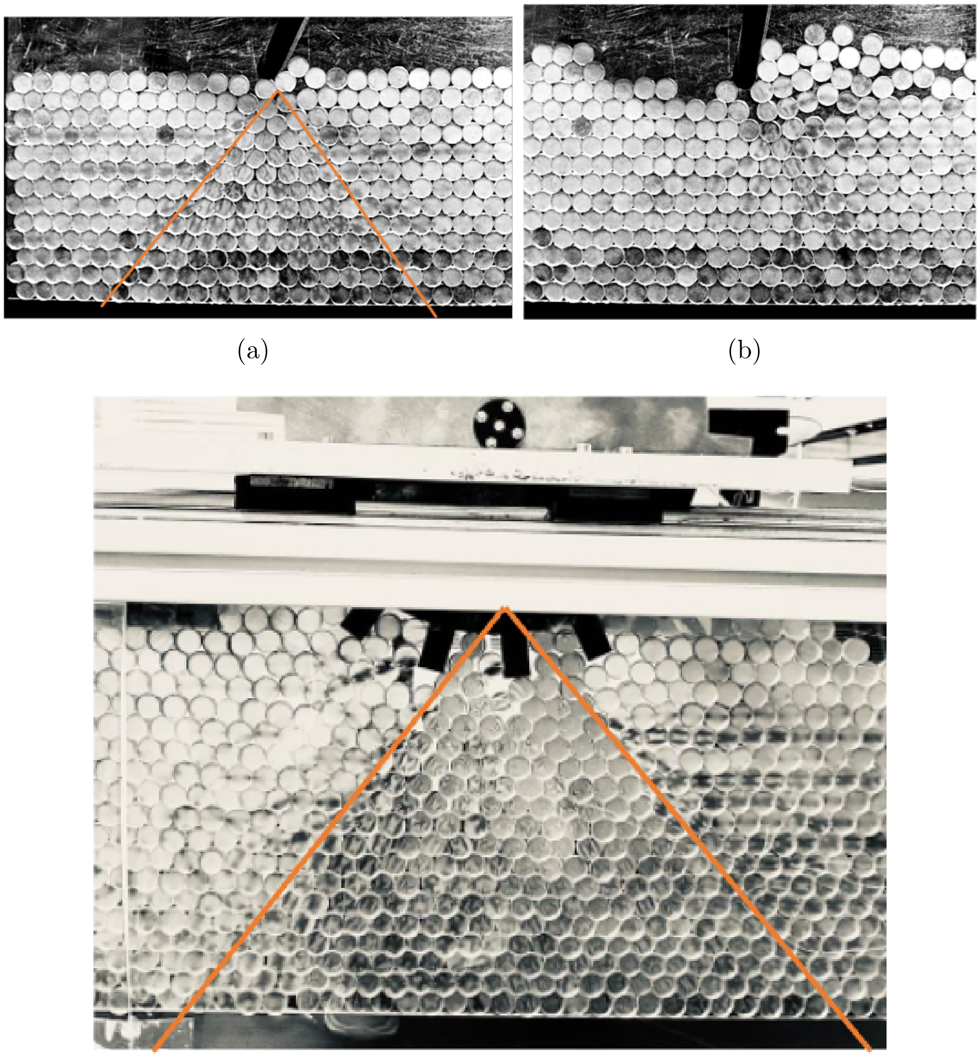

(a) (b)

(c)

Figure 4.26: Comparison between force chains in granular media during interaction with wheel and pendulum: a) Initial phase of interaction with pendulum, b) after time t = 0.65s, and c) force chains during interaction with lugged wheel

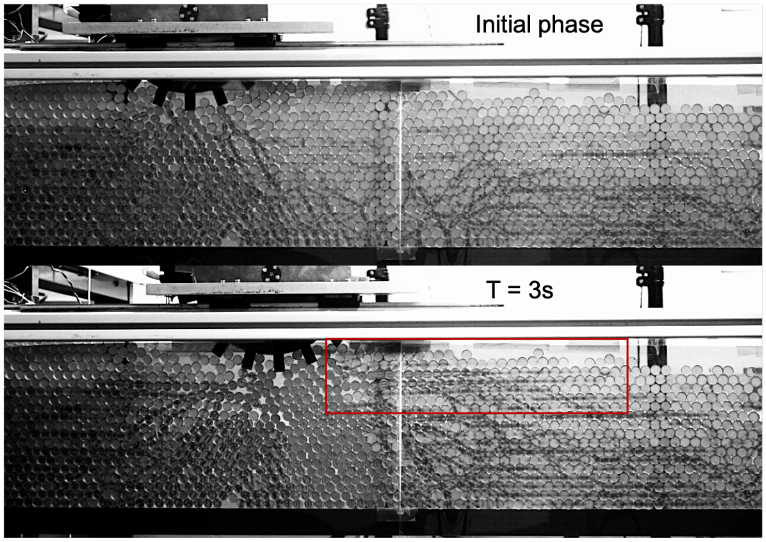

Figure 4.27: Snapshot of force chains generated in initial sinking phase and snapshot of horizontal force chains generated in granular media during locomotion of wheel shown in red rectangular box.

Chapter 5: Summary of Contributions and Recommendations for Future Work

5.1 Summary of Contributions

In this section, the different research findings reported in Chapters 2 through 4 are collected and discussed. A combination of experimental and numerical studies have been undertaken to investigate the principles and physics of interaction between granular media and robot appendages. For two different designs of robot appendages, a lugged wheel and a pendulum, the complex interactions of the granular media and force chain evolution are examined through experimental and numerical tools. The key findings are as follows:

1. Studies on dynamic interactions between lugged wheel and granular media revealed the parameters influencing the locomotion performance of the lugged wheel. Specifically, traction performance of the wheel increases with lug length and traction load, and a non-monotonic behavior is observed for wheel performance with respect to lug width. Further, as slip increases, the performance of the wheel converges for both angular velocity-based control and slip-based control [Ravula et al., 2021].

2. Force chain visualization in granular media during locomotion of lugged wheel presented in this work is demonstrative a quasi-static and dynamic behavior of the granular media. Wheel interaction generated longitudinal and transverse force chains in the soil. The force networks in the soil are concentrated in the portion of granular media that is directly under the wheel, and in the forward path of the wheel which provides a qualitative agreement between the experimental results and numerical studies conducted by using DEM [Ravula et al., 2021, Ravula and Balachandran, 2021].

3. During locomotion of a single actuator pendulum on granular media, force networks are generated in diagonal and horizontal directions. The pendulum impact on the granular surface created force chains along its wake and the momentum transferred to the media can cause buckling of the top granular surface. Driving torque required to rotate the pendulum with a constant angular speed is highest at the moment of impact and decays gradually as the pendulum moves through the media [Acar et al., 2021, Ravula and Balachandran, 2021].

DEM, a computational technique that is based on particle-scale interactions is used to simulate the locomotion of a lugged wheel on granular media and different parameters influencing the performance, as presented in Chapter 3 [Ravula et al., 2021]. DEM can be used to capture behavior of granular media at particle level (micro-scale) and force chains at meso-scale are influenced by the properties of the granular media. Moreover, at macro-scale, the bulk behavior of granular media is influenced by the properties observed at both the length scales, for example, the force chains evolution can influence the granular flow and transitions between solid-like and liquid-like behavior. So, in order to develop a way to bridge the micro-scale and meso-scale properties of granular media, generation and evolution of force chain networks are extensively studied by using the numerical and experimental methods.

In Chapter 3, a visualization of force distribution is presented and the quantitative parameters related to the soil performance such as, the number of particles with higher forces and maximum force in the media are used to compare the soil performance and the wheel performance. In Chapter 4, an experimental arrangement designed to study behavior of granular media during interaction with different designs of robot appendages, a lugged wheel and a pendulum is presented. Under static loading with the wheel, force networks are concentrated in a cone volume developed within the impacted medium. The evolution behavior of these force chains varies for interactions with different appendages. With the locomotion of lugged wheel, the granular media is subjected to a constant static load due to the weight of the wheel as well as the dynamic forcing due to rotation and translation of the wheel. As a result, the force chains observed show effects of dynamic forcing from wheel locomotion in addition to the cone volume with an approximate angle of 45 degrees that travels along with wake. In contrast to the wheel interactions, with the pendulum interactions, the force chains generated are relatively sparse and less dense as the contact area between the pendulum and the granular media is smaller. This work provides a glimpse into the design influences of robot appendages on performance and also aids in developing an understanding into the behavior of granular media at different length scales.

5.2 Recommendations for Future Work

In this section, open problems in legged locomotion on granular media and future recommendations are discussed. In Chapter 3 of this dissertation, the numerical model based on DEM for determining dynamics interactions of soft soil with lugged wheel has been constructed. Many of the granular surfaces existing in nature such as, mud, soil, gravel are partially or completely saturated with moisture. Further, thermal effects cannot be ignored for densely packed substrates and in certain active materials. To expand beyond the focus from dry granular media, it remains to be explored in what ways DEM can be used to realistically simulate legged locomotion on different types of granular media, such as, media with thermal effects, moisture, long range forces, and so on. So, as an extension of the work presented in Chapter 3 and Chapter 4, studies of the effects of granular media properties (e.g., particle size distribution (PSD), particle shape, and cohesion) on the legged locomotion and soil performance could be one potential avenue for future research. Through this dissertation work, two dimensional DEM model employing linear contact between particles has been proven to be effective in simulating the interactions between robot appendages and soft soil. Computational cost, scalability, and model interpretation, specifically for force chains are some of the advantages of using a two-dimensional model. As an extension, studies could also be conducted with other types of real-world granular substrates by taking advantage of the features of three dimensional

DEM modeling and/or assuming Hertzian contact between particles. While both numerical simulations and lab-scale experiments are constrained by the size of the test bed, moving wall boundary conditions for the side walls could be explored instead of the fixed boundary conditions for simulations to gain an insight into the dissipating and dispersing properties of force chains.

In Chapter 4, the author presented qualitative comparisons between DEM and experimental studies for interactions between robot appendages and granular media. Specifically, evolution of force chains along with torque required to drive the appendage has been investigated. The studies and techniques presented do provide a solid foundation for future studies in the area of force network evolution in granular media under dynamic loading/locomotion of robot appendages. In addition to these qualitative investigations, non-dimensional parameters could be determined from numerical and experimental results to make other generalized inferences and quantitative comparisons. Various other designs and gaits of robots/robot appendages could be examined through experimental studies.

Appendix A: Granular Column Collapse

Granular column collapse has been extensively studied by the researchers using both experimental and numerical methods. The flowing behaviour of dense granular media is important in understanding various natural phenomena such as landslides, avalanches, and others. In this dissertation work, the author employed 2D DEM model to carry out simulations for granular column collapse analogous to the experimental investigated carried out by Lube et al. [2005]. Studies show that the morphology of the granular column depends on the initial aspect ratio.

Here, the author conducted studies on tall granular columns with an aspect ratio of 6. To start with, the particles of radius ranging between 3.2 and 4.8 mm are generated inside the boundary walls and the particle assembly is allowed to reach an equilibrium under gravity. The right boundary wall confining the particles is then removed and the profile of the particle assembly is tracked through time. In Figure A.1, the author shows the initial and final geometry of the granular column with an initial aspect ratio of 4.2. For an initial aspect of 6, the flow profiles of the granular column captured at different time steps are shown in Figure A.2. Force distribution is shown for the granular column as it collapses. The magnitude of forces are represented as different colors in the color bar shown in A.1. Same color represents approximately same magnitude of forces. The forces are concentrated on the outer part of the assembly as can be seen in Figure A.2. It can be observed that with time, a part of the assembly closer to the left boundary walls remains intact where as the remaining part closer to the boundary wall that is removed collapses and progressively becomes flatter. The evolution of profiles determined by using DEM compares well with the experimental results from the literature.

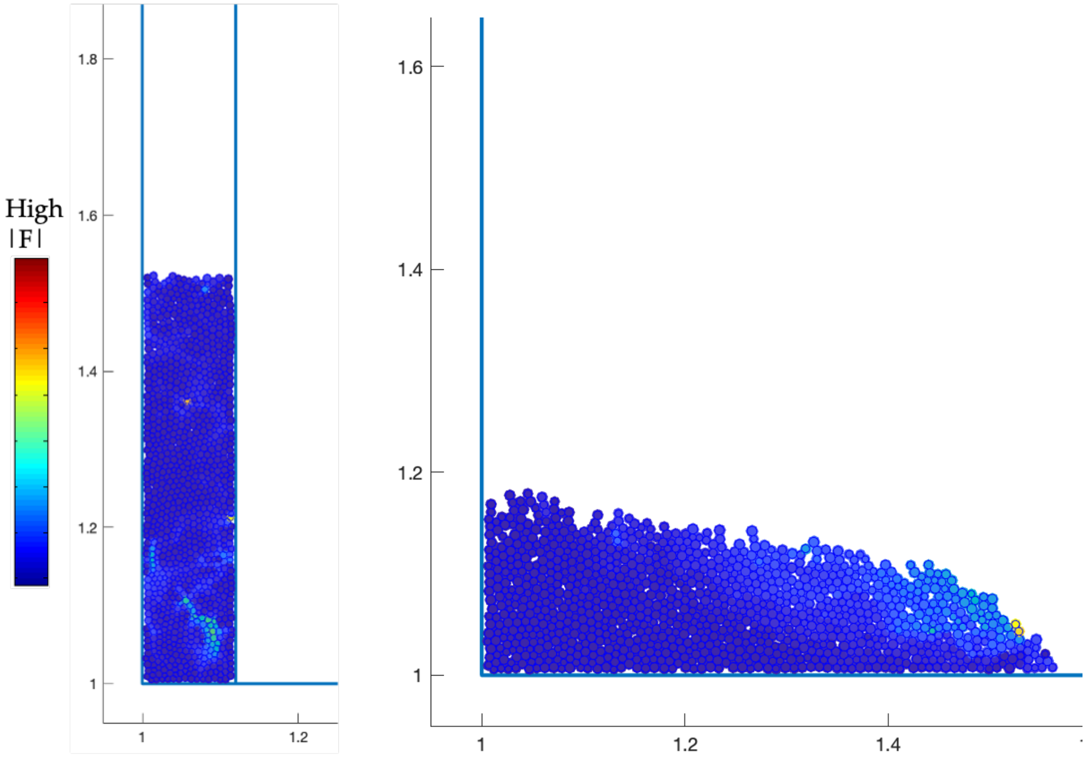

(a) (b)

Figure A.1: a) Initial configuration of granular column and b) after collapse

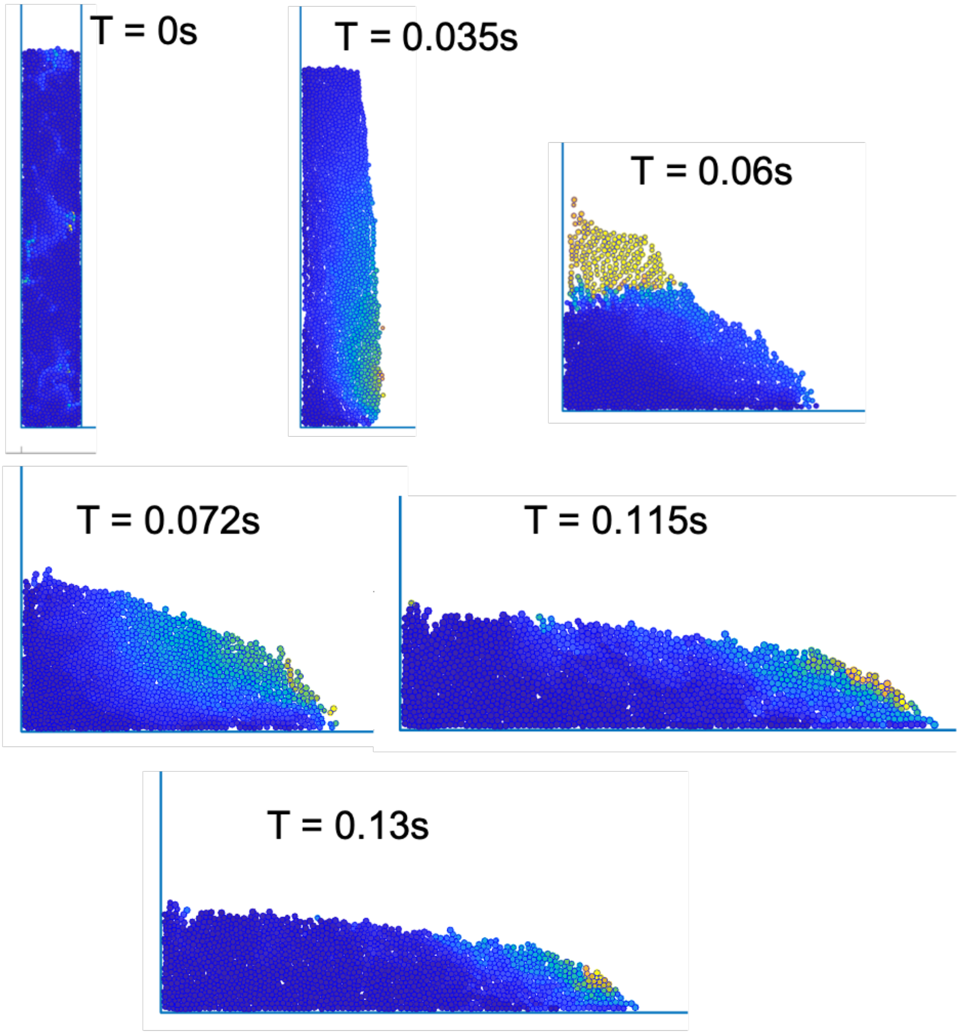

Figure A.2: Evolution of profiles for granular column with an aspect ratio of 0.6, captured at different time steps. In each frame, force distribution in granular column is shown.

Bibliography

G. Acar, P. Ravula, and B. Balachandran. Dynamic interactions of a driven pendulum with photoelastic granular media. *Physics Letters A*, 396:127244, 2021.

H. Bagheri, V. Taduru, S. Panchal, S. White, and H. Marvi. Animal and robotic locomotion on wet granular media. In *Conference on Biomimetic and Biohybrid Systems*, pages 13–24. Springer, 2017.

M. G. Bekker. Mechanics of off-the-road locomotion. *Proceedings of the Institution of Mechanical Engineers: Automobile Division*, 16(1):25–44, 1962.

N. Belheine, J.P. Plassiard, F.V. Donzé, F. Darve, and A. Seridi. Numerical simulation of drained triaxial test using 3d discrete element modeling. *Computational Geotechnic*, 36:320–331, 2009.

G. Besseron, C. Grand, F. B. Amar, F. Plumet, and P. Bidaud. Locomotion modes of an hybrid wheel-legged robot. In *Climbing and Walking Robots*, pages 825–833. Springer, 2005.

S.P.D. Birch, M. Manga, B. Delbridge, and M. Chamberlain. Penetration of spherical projectiles into wet granular media. *Physical Review E*, 90(3):032208, 2014.

T.A. Brzinski III, P. Mayor, and D.J. Durian. Depth-dependent resistance of granular media to vertical penetration. *Physical review letters*, 111(16):168002, 2013.

H. H. Bui, R. Fukgawa, K. Sako, and S. Ohno. Lagrangian mesh-free particle method (sph) for large deformation and post-failure flows of geo-material using elastic-plastic soil constitutive model. *International Journal for Numerical and Analytical Methods in Geomechanics*, 32:1537–1570, 2008.

Oxford Butterworth-Heineman. Numerical modeling of 2-d granular step collapse on erodible and non-erodible surface. *The Finite Element Method: Its Basis and Fundamentals (Sixth ed.)*, 2005.

G.B. Crosta, S. Imposimato, and D. Roddeman. Numerical modeling of 2-d granular step collapse on erodible and nonerodible surface. *Journal of Geophysical Research*, 114:F03020, 2009.

P. A. Cundall and O. D. L. Strack. A discrete numerical model for granular assemblies. *Geotechnique*, 29(1):47–65, 1979.

A. Daerr and S. Douady. Two types of avalanche behaviour in granular media. *Nature*, 399:241–243, 1999.

J.W. Dally. Dynamic photoelastic studies of fracture. *Experimental Mechanics*, 19 (10):349–361, 1979.

K.E. Daniels and N.W. Hayman. Force chains in seismogenic faults visualized with photoelastic granular shear experiments. *Journal of Geophysical Research: Solid Earth*, 113(B11), 2008.

K.E. Daniels, J.E. Kollmer, and J.G. Puckett. Photoelastic force measurements in granular materials. *Review of Scientific Instruments*, 88(5):051808, 2017.

J. V. DeMartini, D.C Richardson, O. S. Barnouin, N.C Schmerr, J.B Plescia, P. Scheirich, and P. Pravec. Using a discrete element method to investigate seismic response and spin change of 99942 apophis during its 2029 tidal encounter with earth. *Icarus*, 328:93–103, 2019.

J. Dijkstra and W. Broere. New method of full-field stress analysis and measurement using photoelasticity. *Geotechnical Testing Journal*, 33(6):469–481, 2010.

L. Ding, H. Gao, Z. Deng, K. Yoshida, and K. Nagatani. Slip ratio for lugged wheel of planetary rover in deformable soil:definition and estimation. *2009 IEEE/RSJ International Conference on Intelligent Robots and Systems*, pages 3343 – 3348, 2009.

L. Ding, H. Gao, Z. Deng, K. Nagatani, and K. Yoshida. Experimental study and analysis on driving wheelsâ€™ performance for planetary exploration rovers moving in deformable soil. *Journal of Terramechanics*, 48(1):27 – 45, 2011.

O. Dorostkar, R.A. Guyer, P.A. Johnson, C. Marone, and J. Carmeliet. Cohesion-induced stabilization in stick-slip dynamics of weakly wet, sheared granular fault gouge. *Journal of Geophysical Research: Solid Earth*, 123(3):2115–2126, 2018.

S. Dunatunga and K. Kamrin. Continuum modelling and simulation of granular flows through their many phases. *Journal of Fluid Mechanics*, 779:483–513, 2015.

H. Fayazfar, M. Salarian, A. Rogalsky, D. Sarker, P. Russo, V. Paserin, and E. Toyserkani. A critical review of powder-based additive manufacturing of ferrous alloys: Process parameters, microstructure and mechanical properties. *Materials & Design*, 144:98–128, 2018.

J.J. Gallagher Jr, M. Friedman, J. Handin, and G.M. Sowers. Experimental studies relating to microfracture in sandstone. *Tectonophysics*, 21(3):203–247, 1974.

J. Geng, G. Reydellet, E. Clément, and R.P. Behringer. Green's function measurements of force transmission in 2D granular materials. *Physica D: Nonlinear Phenomena*, 182(3-4):274–303, 2003.

R. A. Gingold and J.J. Monaghan. Smoothed particle hydrodynamics: Theory and application to non-spherical stars. *Monthly Notices of the Royal Astronomical Society*, 181:375–389, 1977.

B.V. Guerrero, L.A. Pugnaloni, C. Lozano, I. Zuriguel, and A. Garcimartín. Slow relaxation dynamics of clogs in a vibrated granular silo. *Physical Review E*, 97 (4):042904, 2018.

S. Haeri, Y. Wang, O. Ghita, and J. Sun. Discrete element simulation and experimental study of powder spreading process in additive manufacturing. *Powder Technology*, 306:45–54, 2017.

E.J. Hearn. *Mechanics of Materials 2: The mechanics of elastic and plastic deformation of solids and structural materials*. Elsevier, 1997.

M Heverly. *A wheel-on-limb rover for lunar operations*. Pasadena, CA: Jet Propulsion Laboratory, National Aeronautics and Space Administration, 2008.

M. A. Hopkins, J. B. Johnson, and R. Sullivan. Discrete element modeling of a rover wheel in granular material under the influence of earth, mars, and lunar gravity. *Earth & amp; Space 2008*, 323:1–7, 2008.

D. Howell, R.P. Behringer, and C. Veje. Stress fluctuations in a 2D granular couette experiment: a continuous transition. *Physical Review Letters*, 82(26):5241, 1999.

H. Ikari and H. Gotoh. Sph-based simulation of granular collapse on an inclined bed. *Mechanics Research Communications*, 73:12–18, 2016.

K. Iwashita and M. Oda. Rolling resistance at contacts in simulation of shear band development by dem. *Journal of Engineering Mechanics*, 3:285–292, 1998.

X. Jia, C. Caroli, and B. Velicky. Ultrasound propagation in externally stressed granular media. *Physical Review Letters*, 82(9):1863, 1999.

M. Jiang, Y. Dai, L. Cui, and B. Xi. Experimental and dem analyses on wheel-soil interaction. *Journal of Terramechanics*, 76:15 – 28, 2018.

J. B. Johnson, A. V. Kulchitsky, P. Duvoy, K. Iagnemma, C. Senatore, R. E. Arvidson, and J. Moore. Discrete element method simulations of mars exploration rover wheel performance. *Journal of Terramechanics*, 62:31 – 40, 2015.

J. B. Johnson, P. X. Duvoy, A. V. Kulchitsky, C. Creager, and J. Moore. Analysis of mars exploration rover wheel mobility processes and the limitations of classical terramechanics models using discrete element method simulations. *Journal of Terramechanics*, 73:61 – 71, 2017.

P.A. Johnson and X. Jia. Nonlinear dynamics, granular media and dynamic earthquake triggering. *Nature*, 437(7060):871, 2005.

G. Juarez, K. Lu, J. Sznitman, and P.E. Arratia. Motility of small nematodes in wet granular media. *EPL (Europhysics Letters)*, 92(4):44002, 2010.

M.A. Knuth, J.B. Johnson, M.A. Hopkins, R.J. Sullivan, and J.M. Moore. Discrete element modeling of a mars exploration rover wheel in granular material. *Journal of Terramechanics*, 49(1):27 – 36, 2012.

J. P. Latham, A. Munjiza, X. GarcÃa, J. Xiang, and R. Guises. Three-dimensional particle shape acquisition and use of shape library for dem and fem/dem simulation. *Minerals Engineering*, 21:797–805, 2008.

D. Lesniewska and D.M. Wood. Photoelastic and photographic study of a granular material. *Geotechnique*, 61(7):605–611, 2011.

C. Li, P.B. Umbanhowar, H. Komsuoglu, D.E. Koditschek, and D.I. Goldman. Sensitive dependence of the motion of a legged robot on granular media. *Proceedings of the National Academy of Sciences*, 106(9):3029–3034, 2009.

C. Li, T. Zhang, and D.I. Goldman. A terradynamics of legged locomotion on granular media. *Science*, 339(6126):1408–1412, 2013.

R. Li, H. Yang, G. Zheng, and Q.C. Sun. Granular avalanches in slumping regime in a 2D rotating drum. *Powder Technology*, 326:322–326, 2018.

X.K. Li, X.H. Chu, and Y.T. Feng. A discrete particle model and numerical modeling of the failure modes of granular materials. *Engineering Computations*, 22:894–920, 2005.

J. Lim and K. Ravi-Chandar. Dynamic measurement of two dimensional stress components in birefringent materials. *Experimental mechanics*, 49(3):403, 2009.

L. Liu, J. Li, and C. Wan. Nonlinear dynamics of excited plate immersed in granular matter. *Nonlinear Dynamics*, 91(1):147–156, 2018.

W. Losert, L. Bocquet, T.C. Lubensky, and J.P. Gollub. Particle dynamics in sheared granular matter. *Physical review letters*, 85(7):1428, 2000.

G. Lube, H.E. Huppert, R.S. Sparks, and A. Freundt. Collapses of two-dimensional granular columns. *Physical Review Letters E*, 72:1–10, 2005.

L. Lucy. A numerical approach to testing the fission hypothesis. *Astronomical Journal*, 82:1013–1024, 1977.

T.S. Majmudar and R.P. Behringer. Contact force measurements and stress-induced anisotropy in granular materials. *Nature*, 435(7045):1079, 2005.

H. Marvi, C. Gong, N. Gravish, Astley H., Travers M., R.L. Hatton, J.R. Mendelson III, H. Choset, D.L. Hu, and D.I. Goldman. Sidewinding with minimal slip: Snake and robot ascent of sandy slopes. *Science*, 346(6206):224–229, 2014.

P. Mast, C. M.and Arduino, P. Mackenzie-Helnwein, and G. R. Miller. Simulating granular column collapse using the material point method. *Acta Geotechnica*, 10: 101–116, 2014.

S.A. Mirbagheri, E. Ceniceros, M. Jabbarzadeh, Z. McCormick, and H.C. Fu. Sensitively photoelastic biocompatible gelatin spheres for investigation of locomotion in granular media. *Experimental Mechanics*, 55(2):427–438, 2015.

B.R. Mose, D.K. Shin, and J.H. Nam. Development of an experimental system to measure stresses in a bearing using photo-elasticity. *Experimental Mechanics*, 58 (3):437–447, 2018.

H. Nakashima and T.Kobayashi. Effects of gravity on rigid rover wheel sinkage and motion resistance assessed using two-dimensional discrete element method. *Journal of Terramechanics*, 53:37 – 45, 2014.

H. Nakashima, H. Fujii, A. Oida, M. Momozu, Y. Kawase, H. Kanamori, S. Aoki, and T. Yokoyama. Parametric analysis of lugged wheel performance for a lunar microrover by means of dem. *Journal of Terramechanics*, 44(2):153 – 162, 2007.

H. Nakashima, H. Fujii, A. Oida, M. Momozu, H. Kanamori, S. Aoki, T. Yokoyama, H. Shimizu, J. Miyasaka, and K.Ohdoi. Discrete element method analysis of single wheel performance for a small lunar rover on sloped terrain. *Journal of Terramechanics*, 47(5):307 – 321, 2010.

J.G. Osorio, G.J. Stuessy, G.and Kemeny, and F.J. Muzzio. Characterization of pharmaceutical powder blends using in situ near-infrared chemical imaging. *Chemical Engineering Science*, 108:244–257, 2014.

J. Peters, M. Muthuswamy, J. Wibowo, and A. Tordesillas. Characterization of force chains in granular material. *Physical review. E, Statistical, nonlinear, and soft matter physics*, 72:041307, 2005.

F. Qian, T. Zhang, W. Korff, P.B. Umbanhowar, R.J. Full, and D.I. Goldman. Principles of appendage design in robots and animals determining terradynamic performance on flowable ground. *Bioinspiration & biomimetics*, 10(5):056014, 2015.

P. Ravula and B. Balachandran. Force chain propagation in granular media under dynamic loading. *Manuscript in preparation*, 2021.

P. Ravula, G. Acar, and B. Balachandran. Discrete element method-based studies on dynamic interactions of a lugged wheel with granular media. *Journal of Terramechanics*, 94:49–62, 2021.

U. Saranli, M. Buehler, and D.E. Koditschek. RHex: A simple and highly mobile hexapod robot. *The International Journal of Robotics Research*, 20(7):616–631, 2001.

R.B. Shah, M.A. Tawakkul, and M.A. Khan. Comparative evaluation of flow for pharmaceutical powders and granules. *Aaps Pharmscitech*, 9(1):250–258, 2008.

A. Shukla and C. Damania. Experimental investigation of wave velocity and dynamic contact stresses in an assembly of disks. *Experimental mechanics*, 27(3):268–281, 1987.

M.D. Silva and J. Rajchenbach. Stress transmission through a model system of cohesionless elastic grains. *Nature*, 406(6797):708, 2000.

J. Slonaker, D.C. Motley, Q. Zhang, S. Townsend, C. Senatore, K. Iagnemma, and K. Kamrin. General scaling relations for locomotion in granular media. *Physical Review E*, 95(5):052901, 2017.

W. Smith and H. Peng. Modeling of wheel and soil interaction over rough terrain using the discrete element method. *Journal of Terramechanics*, 50(5):277 – 287, 2013.

W. Smith, D. Melanz, C. Senatore, K. Iagnemma, and Huei Peng. Comparison of discrete element method and traditional modeling methods for steady-state wheel-terrain interaction of small vehicles. *Journal of Terramechanics*, 56:61 – 75, 2014.

S.M. Stoffel. Sollicitation dynamique de la couverture des galeries de protection lors de chutes de blocs. *EPFL*, page 208, 1998.

D. Sulsky, Z. Chen, and H. Schreyer. A particle method for hystory-dependent materials. *Computer Methods in Applied Mechanics and Engineering*, 118:179–196, 1994.

Q. Sun, G. Wang, and K. Hu. Some open problems in granular matter mechanics. *Progress in Natural Science*, 19:5, 2009.

Q. Sun, F. Jin, Y. Liu, and G. Zhang. Understanding force chains in dense granular materials. *International Journal of Modern Physics B - IJMPB*, 24:5743–5759, 2010.

M. Sutoh, J. Yusa, T. Ito, K. Nagatani, and K. Yoshida. Traveling performance evaluation of planetary rovers on loose soil. *J. Field Robotics*, 29:648–662, 2012.

M. Tanaka, M. Nishida, T. Kunimochi, and T. Takagi. Discrete element simulation and experiment for dynamic response of two-dimensional granular matter to the impact of a spherical projectile. *Powder Technology*, 124:160–173, 2002.

C. Ulrich, M. Leonardi, and T. Rung. Multi-physics sph simulation of complex marine-engineering hydrodynamic problems. *Ocean Engineering*, 64:109–121, 2013.

P.B. Umbanhowar, F. Melo, and H.L. Swinney. Localized excitations in a vertically vibrated granular layer. *Nature*, 382(6594):793, 1996.

M. Van Hecke. Granular matter: A tale of tails. *Nature*, 435(7045):1041, 2005.

G. Wang, A. Riaz, and B. Balachandran. Smooth particle hydrodynamics studies of wet granular column collapses. *Acta Geotechnica*, pages 1–13, 2019.

D.M. Wendell, K. Luginbuhl, J. Guerrero, and A.E. Hosoi. Experimental investigation of plant root growth through granular substrates. *Experimental Mechanics*, 52(7):945–949, 2012.

Z. Wieckowski and I. Kowalska-Kubsik. A particle-in-cell solution to the silo discharging problem. *International Journal for Numerical Methods in Engineering*, 45:1203–1225, 1999.

J.Y. Wong. Predicting the performances of rigid rover wheels on extraterrestrial surfaces based on test results obtained on earth. *Journal of Terramechanics*, 49 (1):49 – 61, 2012.

D.M. Wood and D. Leśniewska. Stresses in granular materials. *Granular Matter*, 13 (4):395–415, 2011.

S. Yoneyama, S. Arikawa, and Y. Kobayashi. Linear and nonlinear algorithms for stress separation in photoelasticity. *Experimental mechanics*, 52(5):529–538, 2012.

A.A. Zadeh, J. Barés, T.A. Brzinski, K.E. Daniels, J. Dijksman, N. Docquier, H. Everitt, J.E. Kollmer, O. Lantsoght, D. Wang, et al. Enlightening force chains: a review of photoelasticimetry in granular matter. *Granular Matter*, 21, 2019.

L. Zhang, N. G. H. Nguyen, S. Lambert, F. Nicot, F. Prunier, and I. Djeran-Maigre. The role of force chains in granular materials: from statics to dynamics. *European Journal of Environmental and Civil Engineering*, 21(7-8):874–895, 2017.

F. Zhou, R. E. Arvidson, K. Bennett, B. Trease, R. Lindemann, P. Bellutta, K. Iagnemma, and C. Senatore. Simulations of mars rover traverses. *J. Field Robotics*, 31:141–160, 2014.